ALMA MATER STUDIORUM
UNIVERSITÀ DI BOLOGNA

DEPARTMENT OF ELECTRICAL, ELECTRONIC AND INFORMATION ENGINEERING

"GUGLIELMO MARCONI"

SECOND CYCLE DEGREE
IN
BIOMEDICAL ENGINEERING

IN SILICO INVESTIGATION OF THE COMPENSATORY EFFECT OF THE AUTONOMIC NERVOUS SYSTEM IN HAEMODIALYSIS PATIENTS AT TISSUE LEVEL

Supervisor

Prof. Stefano Severi

Co-Supervisors

PD Dr.-Ing. Axel Loewe

M.Sc. Moritz Linder

M.Sc. Eugenio Ricci

Defended by

Michele Terren

Graduation Session 12/03/2026

Academic Year 2024/2025

Statutory declaration

I declare that I have authored this thesis independently, that I have not used other than the declared sources/resources, and that I have explicitly marked all material which has been quoted either literally or by content from the used sources.

Cesena, March 3, 2026

Abstract

The sinoatrial node (SAN) is the primary pacemaker of the heart and is responsible for the rhythmic initiation of each heartbeat through the spontaneous activity of specialised pacemaker cells. Its automaticity arises from a tightly regulated interplay between membrane ionic currents and intracellular calcium cycling, and is highly susceptible to changes in the extracellular milieu. Electrolyte imbalances are common in patients with chronic kidney disease undergoing haemodialysis (HD), a population with a markedly increased incidence of sudden cardiac death (SCD), which is frequently preceded by sinus bradycardia and asystole. Previous single-cell in silico investigations demonstrated that hypocalcaemia slows the beating rate; this effect can be transiently offset by sympathetic stimulation, whereas abrupt withdrawal of sympathetic tone can abolish automaticity.

To determine whether these mechanisms are preserved at the tissue level, we implemented a discrete intercellular coupling framework in openCARP. A calibrated population of models generated from the extended Severi DiFrancesco model was embedded in a two-dimensional patch of SAN tissue. Subsequently, hypocalcaemia and graded autonomic modulation were simulated over a wide range of coupling resistances.

Our results demonstrate that intercellular coupling and cellular heterogeneity prevent sinus arrest at the tissue level, even under severe hypocalcaemia and sympathetic withdrawal. Although sympathetic stimulation reduced the cycle length and increased the proportion of spontaneously depolarising cells, it was not essential to maintain global tissue automaticity, in contrast to single-cell predictions. These findings indicate that tissue-level interactions mitigate the deleterious effects of hypocalcaemia predicted in isolated cells, suggesting that the mechanism underlying HD patients SCD episodes needs to be further investigated by considering the interaction between the SAN and the surrounding atria.

Acknowledgments

I am deeply grateful to Prof. Stefano Severi for arranging the exchange here at the Karlsruhe Institute of Technology that not only allowed me to write my dissertation in a insitute at the forefront of computational cardiology research, but also made me discover a new country, know more people, and make new friends.
My best regards go also to PD-Dr.-Ing. Axel Loewe for hosting me at the Institute of Biomedical Engineering (IBT), and most importantly for having provided guidance and insightful feedback during the development of this thesis.
I am thankful to M.Sc. Eugenio Ricci, who not only inspired and contributed to this thesis with his previous work, but also provided precious help.
A special thank goes to my supervisor at IBT M.Sc. Moritz Linder who laid the foundations for this thesis and helped me in every step of the process, not limiting his contribution to the research aspects, but also making sure that I integrated in the research group.
I would also like to thank everybody at IBT who became a friend along the way and brightened the dark German winter days during which we carried out our work. At the same time I need to thank all my friends at home who stayed closed to me even if I was far.
I will always be grateful to my family, who supported me for all these university years, and especially so during these last months abroad.
Last but surely not least, I thank my girlfriend Matilde for constantly cheering me in the good and in the bad days, for enduring a 20 hours long round trip to visit me and for her daily gestures, which made me feel her love in spite of the distance.

Contents

Abbreviations

V_m	transmembrane voltage . . . . . 8, 13, 25 ff., 32, 35, 38
ACR	albuminuria to creatine ratio 20
AER	albumin excretion ratio 20
ANS	autonomic nervous system . . . 2, 6, 24 f., 35, 41, 43, 47 f., 53, 57
AP	action potential . . . . . 7 ff., 12 f., 16, 25, 27, 38, 43, 52, 54
APA	action potential amplitude 13, 15, 38, 43, 53, 55
APD	action potential duration 13, 15, 35
ATP	adenosine tri-phosphate 8, 15
AV	atrioventricular . . . . . 3 ff.
BR	beating rate . . . . . 1 f., 13, 15, 17, 24, 27, 57
CKD	chronic kidney disease . . . . . 1 f., 20 ff., 24
CL	cycle length . . . . . 13, 16, 27, 35, 38, 43, 45–48, 52 ff., 59
CO	cardiac output 6
CT	crista terminalis 11
CV	conduction velocity . . . . . 16 f., 34, 37, 41, 51
CVD	cardiovascular disease 24
DALY	disability-adjusted life-year . . . . . 21 f.
DD	diastolic depolarization 1, 13–17, 27, 38, 43
EMI	extracellular-membrane-intracellular . . . . . 29 f.
ESRD	end stage renal disease 20, 24
FEM	finite element method . . . . . 2, 25, 31 f., 61, 65 f.
GBD	Global Burden of Disease, Injuries, and Risk Factors Study . . 1, 21
GFR	glomerular filtration rate . . . . . 19 f.
HD	haemodialysis . . . . . 1 f., 23 f., 54, 57, 60
HR	heart rate 6, 17
IAS	interatrial septum 11
ISO	isoprenaline . . . . . 27, 37 f., 47 f., 53, 55, 59
IVC	inferior vena cava 11
KDIGO	Kidney Disease: Improving Global Outcomes 20
KNM	Kirchhoff network model . . . . . 30 f.
KRT	kidney replacement theraphy 22
LAT	local activation time 34
LIDP	long interdialytic period 24

MDP maximum diastolic potential 13, 35, 38
NCX sodium calcium exchanger 15
ODE ordinary differential equation 25, 27
OS overshoot . . . . . 12 f., 35, 38
PD peritoneal dialysis 23
PDE partial differential equation 31, 66
POM population of models . . . . . 35 f., 46, 52, 54, 57, 59
RA right atrium 11, 57
SACP SAN conduction pathway . . . . . 11 f.
SAN sinoatrial node 1 f., 4, 10 ff., 14–17, 20, 24, 27, 35, 37, 42, 51, 54 f., 57–60
SANC SAN cell . . . . . 1 f., 12–16, 25, 27, 38, 52, 54 f.
SCD sudden cardiac death . . . . . 1 f., 24, 57
SDiF Severi DiFrancesco 27, 35, 37, 45, 47, 52, 54, 59
SEP SAN exit pathway 11, 16
SF safety factor 17
SIDP short interdialytic period 24
SKNM simplified Kirchhoff network model25, 31, 33, 35, 37, 41, 51, 57, 59, 61, 66
SMC sequential Monte Carlo . . . . . 35 f.
SR sarcoplasmic reticulum 7, 15, 28
SV stroke volume 6
SVC superior vena cava 11
TOP take off potential . . . . . 13, 38 f.
UI uncertainty interval . . . . . 21 f.

Chapter 1

Introduction

The sinoatrial node (SAN) is the primary natural pacemaker of the heart. It regularly provides excitation to the atria, which then propagates to the rest of the heart, causing contraction.
The spontaneous beating rate (BR) of SAN cells (SANCs) is tightly regulated by a fine-tuned equilibrium between inward and outward transmembrane currents during the diastolic depolarization (DD) phase of the caridac cycle, together with the complex interaction between the *calcium* and *membrane clock*, known as the *coupled clock* mechanism.
The extracellular milieu can deeply affect the electrophysiology of the SAN, and is therefore strongly controlled in mammals [1].

One of the most important functions of the kidneys is the maintenance of the homeostasis of ions in the blood and in the extracellular milieu. Chronic kidney disease (CKD) hinders the ability of the kidneys to keep electrolyte concentrations within the narrow ranges compatible with life, with consequences for several other organ systems, including the heart and the SAN. Globally, in 2017, a systematic analysis from the all-age Global Burden of Disease, Injuries, and Risk Factors Study (GBD) project found 697.5 million cases of all-stage CKD [2].
CKD patients undergoing haemodialysis (HD) experience a high annual mortality rate of 17% [3]. Up to a quarter of these deaths are caused by sudden cardiac death (SCD) [3–5], exposing the HD population to a risk of SCD 14 times higher than in cardiovascular patients with normal kidney function [5].

Most SCD episodes take place at the end of the long interdialytic period [3–5], i.e. the three days interval between the last and the first HD session of consecutive weeks. Furthermore, long-term studies on HD patients with implanted loop recorders, i.e. devices used to continuously measure the electrical activity of the heart, showed that the rhythm at the time of death is sinus bradycardia followed by asystole, whereas in the general population SCD is mostly caused by ventricular tachyarrhythmias such as ventricular fibrillation [3, 4].
Zaho *et al.* found that SCD was preceded by an abrupt reduction of sympathetic tone in CKD rat models, which were also associated with a reduced response of the BR to sympathetic stimulation [6].

In silico studies on SAN single-cell models provided mechanistic insights on SCD in HD patients. Loewe *et al.* investigated the effect of altered electrolyte concentrations on SAN pacemaking, proving that hypocalcaemia lowers the BR of SANCs [1]. This was later confirmed by a case report of an 80-year-old woman who experienced sinus arrest followed by bradycardia, which was caused by severe iatrogenic hypocalcaemia [7].
Linder *et al.* showed that, in computational models of rabbit and human SANCs, the autonomic nervous system (ANS) can compensate for the hypocalcaemia-induced bradycardia maintaining sinus rhythm. At the same time, they found that a sudden withdrawal of the sympathetic tone while under hypocalcaemia resulted in a loss of automaticity within seconds [8].
While various tissue implementations of the SAN have been used to study different aspects of pacing, none included the graded compensatory response of the ANS implemented by Linder *et al.* [9–12]. Hence, the following research question was formulated:

Research question

How does the compensatory response of the autonomic nervous system to hypocalcaemia-induced bradycardia change in tissue-level simulations of the sinoatrial node compared to single-cell simulations?

The next two chapters will introduce the medical and mathematical fundamentals necessary to understand this work. Namely, Chapter 2 will describe the heart anatomy and physiology, with particular focus on the SAN. It will also dive into kidney structure and function, concluding with a section dedicated to the interaction of these organs in CKD. Chapter 3 will introduce the basics of computational cardiology, describing single-cell models, the possible strategies to simulate the heart at the tissue-level, and providing a brief overview of the finite element method (FEM).
Chapter 4 describes the methods used for this work, including the implementation of a discrete intercellular coupling mechanism in openCARP, and how it was used to perform simulations of the SAN under hypocalcaemia and sympathetic stimulation.
The results will be reported in Chapter 5 and discussed in Chapter 6. Lastly the limitations of this work, and the future perspectives are presented in Chapter 7, while Chapter 8 sums up the major findings and compares them to previous publications.
Two appendixes provide additional information regarding the discrete coupling implementation in openCARP (Appendix A) and the preliminary results obtained by including fibroblasts in the tissue (Appendix B).

Chapter 2

Medical Fundamentals

2.1 Heart Anatomy and Physiology

The first medical description of the heart dates back to the ancient "Egyptian medical papyri", which are thought to have been written around 1600 - 1900 BCE [13]. Heart anatomy and physiology have been studied ever since, however, despite millennia of inquiries, a comprehensive understanding of the heart has not been achieved yet.
The anatomy of this organ is closely related to its function, which is to pump blood throughout the body to supply tissues with oxygen and to remove metabolic waste products. This chapter presents the anatomical and physiological fundamentals necessary for understanding the subsequent sections of this manuscript.

2.1.1 Anatomy

The heart has roughly the dimensions of a human fist and weights about 350 g. It is located in the protective thorax, posterior to the sternum and between the lungs, in the so called mediastinum, and is encapsulated by the pericardium (Figure 2.1). It lies obliquely on top of the diaphragm, along the plane connecting the right shoulder to the left nipple, with two thirds of it left of the midline [14].
The atrial and the ventricular septa separate the organ in two functionally and anatomically similar halves: the left heart and the right heart. The left heart collects the oxygenated blood flowing from the lungs and pumps it into the rest of the body. Conversely, the right heart receives the de-oxygenated blood from the body and sends it into the lungs.
Similarly, the atrioventricular (AV) septum divides the top chambers, known as atria, from the bottom chambers, called ventricles. The atria collect the blood which they receive from the veins and push it into the ventricles. Ventricles, on the other hand, pump the blood into the pulmonary arteries and in the aorta. Four valves ensure unidirectional flow between the atria and the ventricles and between the ventricles and the arteries.

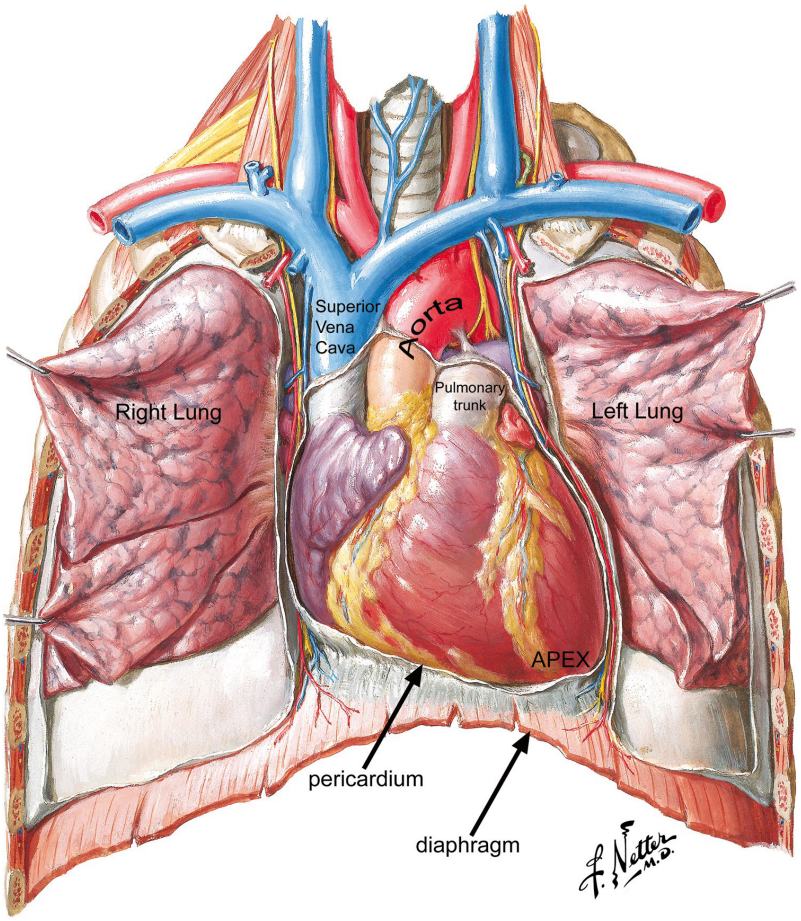

Figure 2.1: Heart location in the protective thorax. It sits obliquely on top of the diaphragm between the lungs, with the apex left of the midline. It is contained by the pericardium. Figure taken from [14].

The heart is a hollow organ, meaning that the atria and the ventricles are composed by a wall that surrounds a blood filled cavity. Figure 2.2 shows a cross section of the wall. It consists mainly of muscle tissue, the myocardium, which is covered on the inside by the endocardium and on the outside by the epicardium. Since the ventricles have to generate more power, the myocardium is thicker in these chambers than in the atria.

2.1.1.1 Conduction System

At rest, the heart pumps 5 l/min of blood into the body contracting 60-70 times per minute. To do so it is crucial that the aforementioned structures, i.e. atria and ventricles, contract in the correct order. However, myocardial cells can contract only upon excitation by the surrounding cells (see Section 2.1.3). The conduction system (see Figure 2.3) ensures the coordination of all the cardiac structures. Excitation is initiated in the SAN (see Section 2.2), where special pacemaker cells periodically depolarise. It then propagates through the atria causing their contraction. The fibrotic tissue of the valves and the AV septum is unexcitable

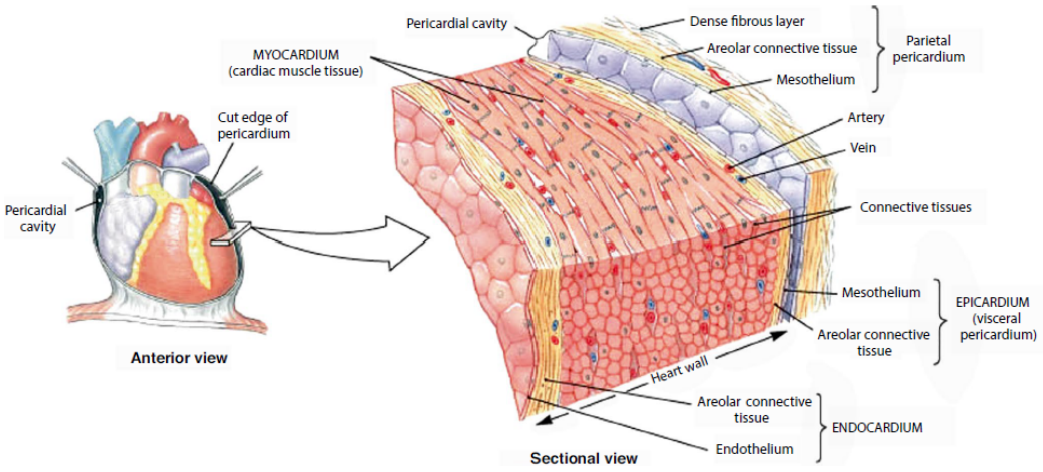

Figure 2.2: Cross section of the heart wall. Three main layers are distinguishable: the endocardium in contact with he blood, the myocardium i.e. the cardiac muscle tissue, and the epicardium. The latter is separated from the parietal pericardium by the pericaricardial cavity. Figure taken from [14].

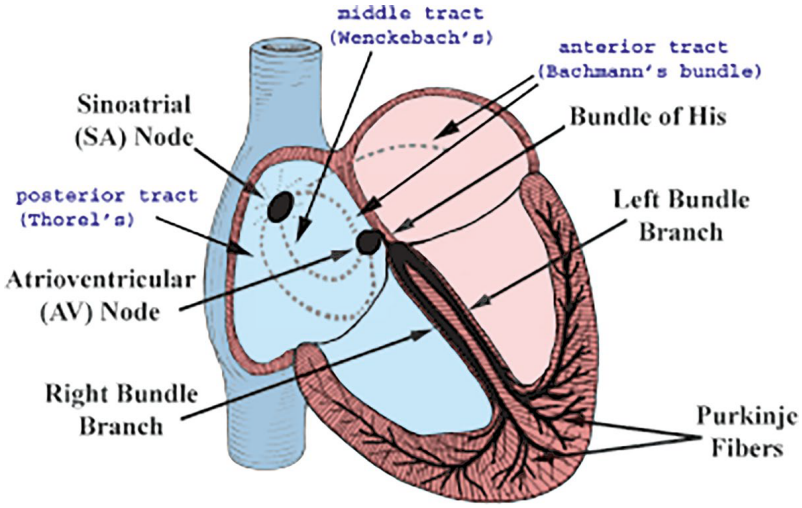

Figure 2.3: Conduction system. The dashed lines connecting the SAN to the AV node and to the left atrium should not be interpreted as macroscopic structures but as preferential pathways of aligned cardiomyocytes. From the AV node the conduction system continues with the Bundle of His, the left and right bundle branches in the septum and the Purkinje fibres. Figure taken from [14].

and prevents the depolarisation wave from reaching the ventricles. Indeed the AV node is the only pathway that electrically connects atria and ventricles. It also introduces a delay between atrial and ventricular contraction, essential for the proper functioning of the heart. From here the excitation signal propagates through the bundle of His, then splits between the right and the left bundle branches and ends in the Purkinje fibres.

2.1.2 Physiology

Under normal physiologic conditions, the human heart functions as two separate pumps working in series; the right heart pumps blood through the pulmonary circulation, and the left heart pumps blood through the systemic circulation. Since the two halves of the heart are in series, they both pump the same amount of blood every minute. This quantity is known as cardiac output (CO) and can be calculated as follows:

$$CO = HR \times SV. \tag{2.1}$$

The CO is determined by two primary variables: the heart rate (HR), which is the number of heartbeats per unit of time (typically expressed in beats per minute), and the stroke volume (SV), which is the volume of blood ejected by the left ventricle during a single contraction. While CO remains relatively constant at rest, it can increase significantly during physical exertion through the modulation of both variables by the ANS. The SV is influenced by three main factors: preload (the degree of stretch of the ventricular cardiomyocytes at the end of diastole), afterload (the resistance the heart must pump against), and contractility (the innate force of the heart muscle).

2.1.3 Electrophysiology

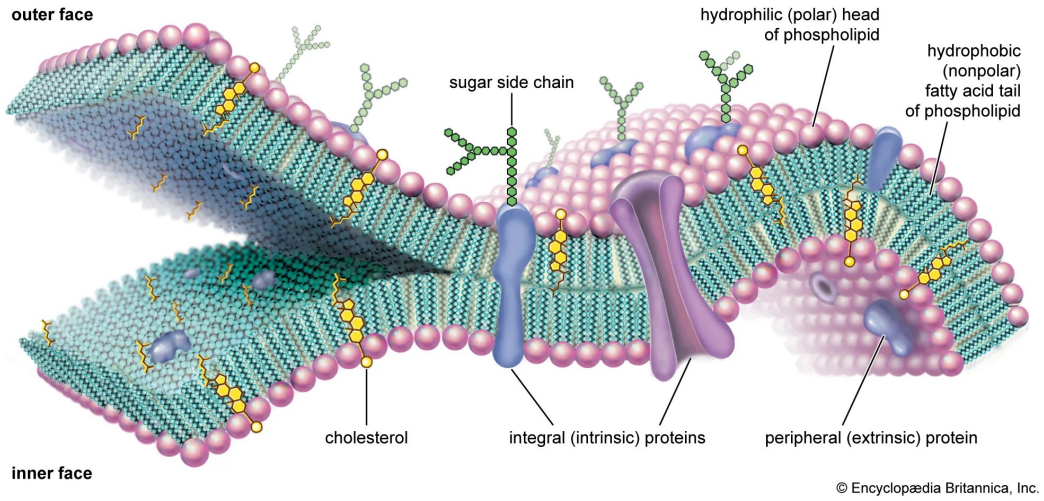

Figure 2.4: Illustration of the cell membrane. The double phospholipidic layer is crossed by channel proteins which allow the passage of ions between the intracellular and the extracellular spaces. Figure taken from [15].

2.1.3.1 Basics of Cell Electrophysiology

The cardiac cell is enclosed by a plasma membrane $\approx 5\,\text{nm}$ thick, consisting of a phospholipid bilayer. This membrane acts as a hydrophobic barrier, preventing the free diffusion of charged ions and maintaining a strictly regulated intracellular environment. As Figure 2.4 shows, embedded within this lipid milieu are various amphipathic proteins, including receptors for biochemical signaling and ion-specific pumps and channels that regulate the cell's internal ionic composition [14].
In cardiomyocytes (Figure 2.5), the plasma membrane (sarcolemma) features deep invaginations known as transverse tubules (T-tubules). These tubules form a reticular network that brings the extracellular environment into close proximity with the internal myofibrils. The T-tubules are closely associated with the sarcoplasmic reticulum (SR), a specialised organelle for calcium storage. This anatomical arrangement is critical for excitation-contraction coupling, as it allows the action potential (AP) to propagate into the cell interior and trigger the release of intracellular calcium stores [14].

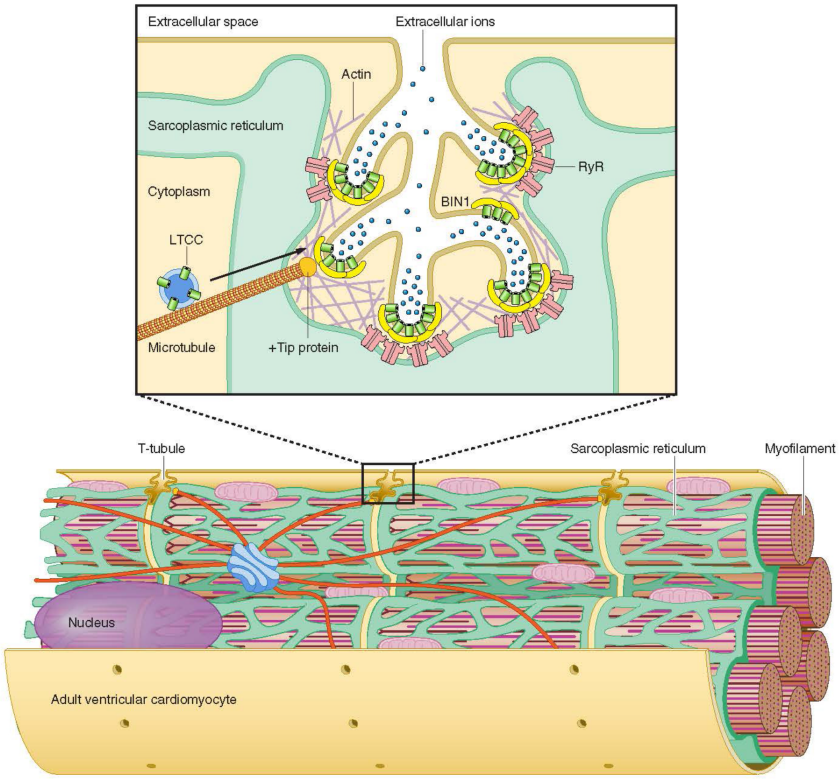

Figure 2.5: Representation of a cardiomyocyte with an enlargement fo a T-tubule. Figure taken from [16].

2.1.3.2 Action Potential

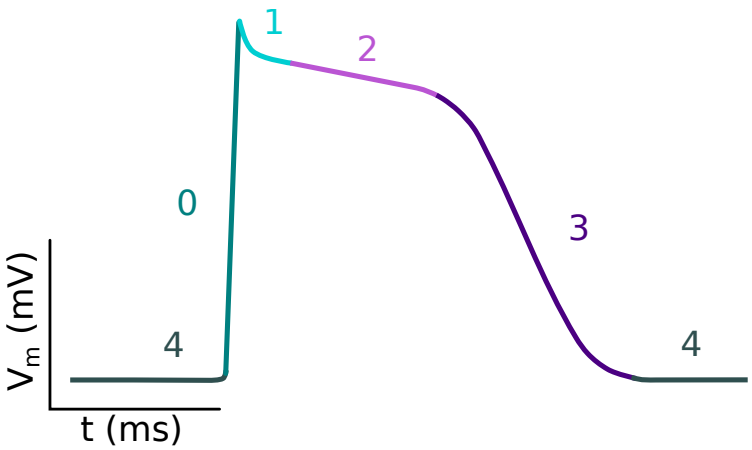

Figure 2.6: The course of transmembrane voltage (V_m) during a cardiac AP with its different phases: (0) upstroke, (1) initial repolarisation, (2) plateau, (3) repolarisation, (4) resting potential.

Cardiac function relies on the generation of electrical gradients across the cell membrane. By utilising adenosine tri-phosphate (ATP)-dependent pumps and selective ion channels, cardiomyocytes maintain a resting transmembrane voltage (V_m) where the interior is negatively charged (approximately 90 mV) relative to the exterior.
The equilibrium potential for a specific ion (E_{ion}), at which the chemical and electrical driving forces are balanced, is defined by the Nernst equation:

$$E_{ion} = \frac{RT}{zF} \ln \frac{[ion]_{out}}{[ion]_{in}}. \tag{2.2}$$

While several ions contribute to the electrical state, the resting potential of a myocyte is primarily determined by potassium (K^+), as the membrane is most permeable to K^+ at rest. To account for the simultaneous influence of multiple ions (K^+, Na^+, Ca^{2+}) and their respective membrane conductances (g), the overall membrane potential (E_m) can be described by a simplified Goldman-Hodgkin-Katz relation:

$$E_m = \frac{g_{Na}}{g_{tot}} E_{Na} + \frac{g_K}{g_{tot}} E_K + \frac{g_{Ca}}{g_{tot}} E_{Ca}. \tag{2.3}$$

The cardiac AP is characterised by transient changes in these ionic permeabilities and is traditionally described in five phases (Figure 2.6):

- **Phase 0 (Upstroke):** Triggered when the membrane potential reaches a threshold (approx. 40,mV above rest), causing voltage-gated Na^+ channels to open rapidly.
- **Phase 1 (Initial Repolarisation):** A brief period where Na^+ channels inactivate and transient K^+ currents initiate.

- **Phase 2 (Plateau):** Unique to cardiac tissue, this phase is sustained by an inward flux of Ca^{2+} through L-type channels, balancing the outward K^+ current.
- **Phase 3 (Repolarisation):** Closure of Ca^{2+} channels and increased K^+ efflux drive the potential back toward E_K.
- **Phase 4 (Resting Potential):** The cell returns to its resting state.

Crucial to cardiac safety is the refractory period, which occurs from Phase 0 through mid-Phase 3. During this time, Na^+ channels transition from an inactive to a closed (but responsive) state, preventing the cell from responding to premature stimuli and ensuring the heart has adequate time to relax and fill with blood.

2.1.3.3 Gap Junctions and Propagation

Electrical coordination across the myocardium is achieved through gap junctions (see Figure 2.7), which connect the cytoplasms of adjacent cells to form a functional syncytium. These junctions are composed of two docked hemichannels (connexons), each formed by six connexin proteins. These aqueous pores allow for the low-resistance passage of ions and small molecules, enabling the APs to propagate rapidly throughout the tissue, resulting in a synchronised and efficient contraction [14].

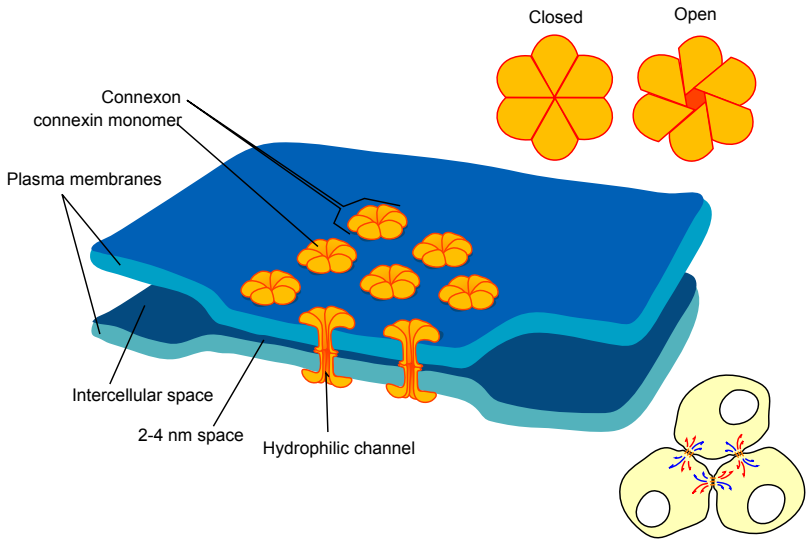

Figure 2.7: Representation of a cluster of gap junctions. They allow the passage of ions from one cell to the other, enabling the propagation of APs. Each junction is composed of two docked connexons, which are in turn formed by six connexin proteins. Figure taken from [17].

2.2 The Sinoatrial Node

As a director guides the orchestra, the astonishingly complex function of the heart is directed by the SAN, which relentlessly paces the atria to initiate the contraction that provides the rest of the body with freshly oxygenated blood.
The SAN was discovered relatively recently by Keith and Flack in 1907 [18] (Figure 2.8). Its anatomy and the details of its function have long been subject of discussion and are still being pieced together [19]. In this section the state-of-the-art regarding the SAN will be discussed.

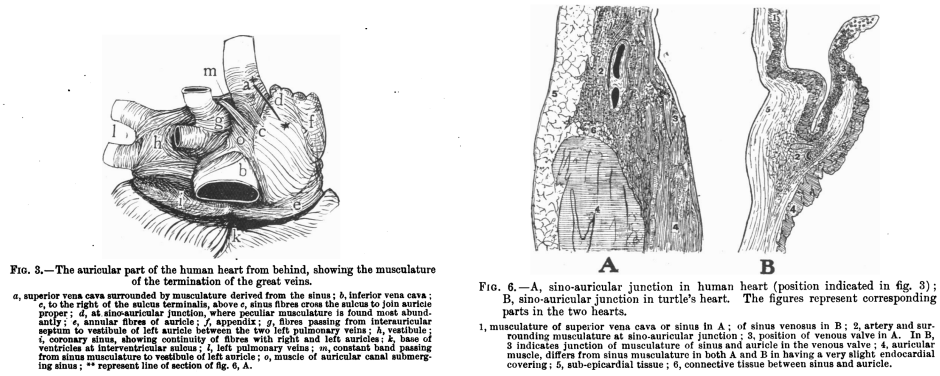

FIG. 3.—The auricular part of the human heart from behind, showing the musculature of the termination of the great veins.

a, superior vena cava surrounded by musculature derived from the sinus; *b*, inferior vena cava; *c*, to the right of the sulcus terminalis, above *c*, sinus fibres cross the sulcus to join auricle proper; *d*, at sino-auricular junction, where peculiar musculature is found most abundantly; *e*, annular fibres of auricle; *f*, appendix; *g*, fibres passing from interauricular septum to vestibule of left auricle between the two left pulmonary veins; *h*, vestibule; *i*, coronary sinus, showing continuity of fibres with right and left auricles; *k*, base of ventricles at interventricular sulcus; *l*, left pulmonary veins; *m*, constant band passing from sinus musculature to vestibule of left auricle; *o*, muscle of auricular canal submerging sinus; ** represent line of section of fig. 6, A.

FIG. 6.—A, sino-auricular junction in human heart (position indicated in fig. 3); B, sino-auricular junction in turtle's heart. The figures represent corresponding parts in the two hearts.

1, musculature of superior vena cava or sinus in A; of sinus venosus in B; 2, artery and surrounding musculature at sino-auricular junction; 3, position of venous valve in A. In B, 3 indicates junction of musculature of sinus and auricle in the venous valve; 4, auricular muscle, differs from sinus musculature in both A and B in having a very slight endocardial covering; 5, sub-epicardial tissue; 6, connective tissue between sinus and auricle.

Figure 2.8: Illustrations of the SAN location and its anatomy from the seminal work of Keith and Flack. Figures taken from [18].

2.2.1 Anatomy

The SAN consists of a crescent shaped mass of specialised cardiomyocytes, collagen, fibroblasts and fatty tissue [20]. Table 2.1 shows the dimensions of the SAN reported in literature.

Table 2.1: Studies of SAN structure and dimensions. Table adapted from [20].

Study	Length (mm)	Width (mm)	Depth (mm)	Step Size (µm)	Sectioning
James, 1961 (n=79)	15	5	1.5	NA	Perpendicular to Epi
Truex *et al.* , 1967 (n=5)	7.3	NA	1.6	50	Perpendicular to Epi
Alings *et al.* , 1995 (n=32)	NA	4.8	1.2	100	Perpendicular to Epi
Sanchez-Quintana *et al.* , 2005 (n=47)	13.5	5.3	1.5	200	Perpendicular to Epi
Chandler *et al.* , 2001 (n=1)	29.5	6.4	1.8	500	Perpendicular to Epi
Federov *et al.* , 2010 (n=4)	14.3	6.7	1	480	Perpendicular to Epi
Csepe *et al.* , 2016 (n=1)	12.0	3.3	2.2	21	Parallel to Epi
Csepe *et al.* , 2016 (n=1)	17.0	3.5	1.2	13	Parallel to Epi

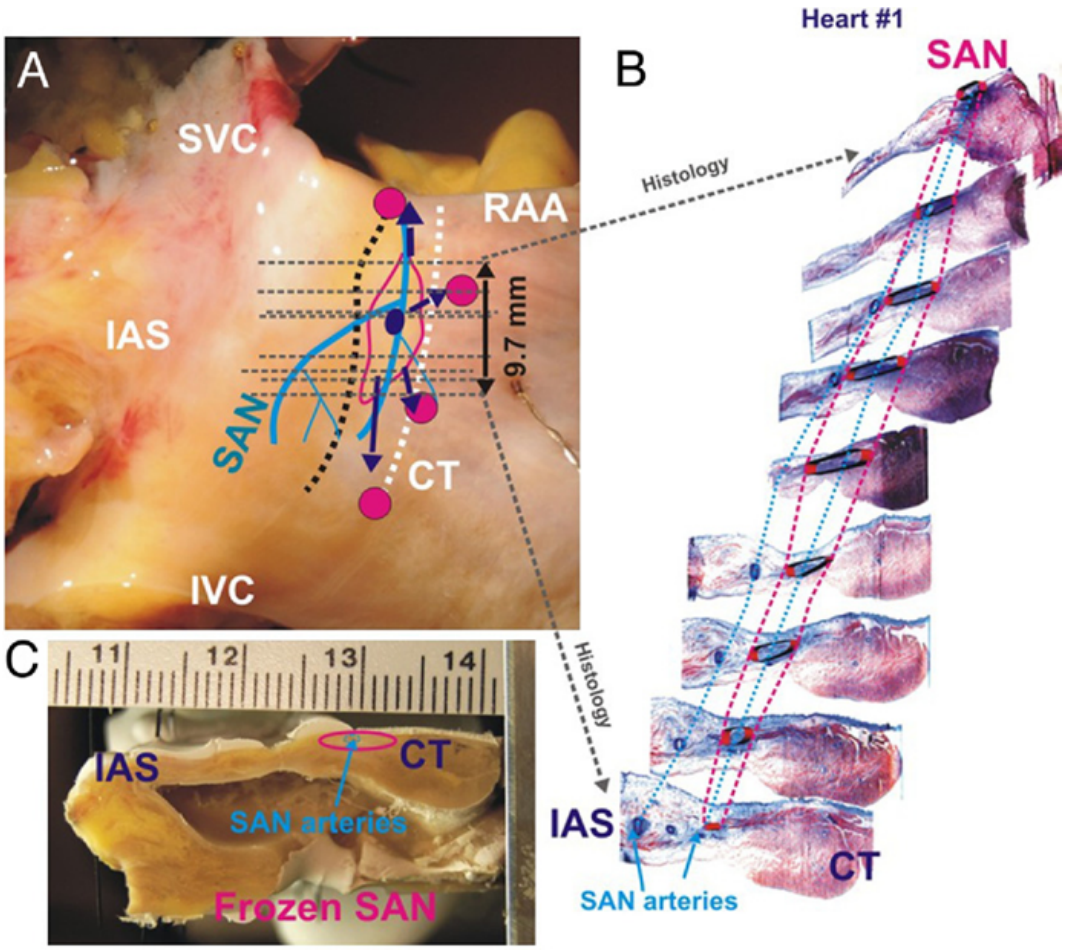

Figure 2.9: SAN location and histological slices. Panels A and C show two perpendicular perspectives of the human SAN including anatomical (arteries – blue lines, SAN – red outline) and functional (SAN conduction pathways (SACPs) – purple arrows, leading pacemaker site – purple dot, breakthrough sites – magenta dots) features. Grey dashed lines represent location of histology sections shown in Panel B and had the same perpendicular orientation as in Panel C. Figure taken from [21].

It is located in the right atrium (RA) between the superior vena cava (SVC) and inferior vena cava (IVC). More precisely, it spans laterally from the interatrial septum (IAS) to the crista terminalis (CT) [21] (Figure 2.9) and twists intramurally from the endocardium to the epicardium [22] (Figure 2.10).

The nature of the boundary between the SAN and the surrounding RA has long been subject of discussion [23]. Some research groups advocated for the presence of diffused interdigitations that would have connected the SAN to the RA [24, 25], while others supported the hypothesis of an insulating wall constituted by fibrotic and fatty tissue and/or discontinuous fibres, which would open at specialised SAN conduction pathways (SACPs), also known as SAN exit pathways (SEPs) [20, 21].

As reported by Csepe *et al.* , the contradictory hypothesis regarding the boundary between the SAN and the RA have probably arisen from a lack of resolution of both functional and

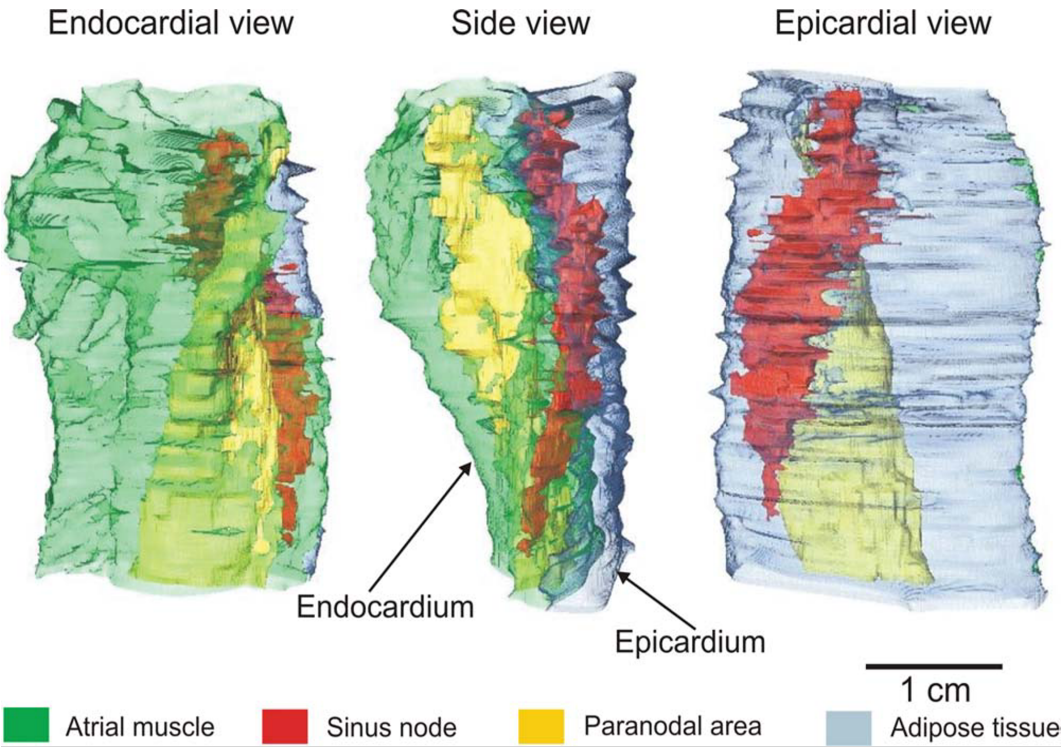

Figure 2.10: 3D reconstruction of the SAN. Endocardial, side and epicardial views shown. The SAN is located beneath the epicardium of the CT, with a layer of atrial muscle separating it from the endocardium. The paranodal area expresses characteristics transitional between those of the SAN and the atrial muscle, and extends towards the IVC. Figure taken from [22].

structural mapping of the SAN as well as human SAN studies that only analysed SAN structure from 2D sections [20]. Thanks to their innovative method that combined functional and structural high-resolution analysis, they were able to provide definitive evidence of the presence of SACPs (Figure 2.11). These have since been included in the latest whole SAN computational models [10–12].

2.2.2 Electrophysiology

In contrast to the cells of the working myocardium, SANCs exhibit automaticity, i.e. they periodically depolarise, giving rise to APs without the need of external stimuli.
As it can be appreciated in Figure 2.12 SANCs APs differ from ventricular and atrial cells APs. Firstly, the upstroke is not mediated by Na^+ (through fast sodium channels), but instead by Ca^{2+} through the L-type Ca^{2+} channels. The slower dynamics of this transport results in a lower upstroke velocity $\frac{dV_m}{dt}_{max}$. Secondly, in contrast to ventricular cells, SANCs do not have a plateau phase, and soon after the peak potential, which from here on will be referred to as overshoot (OS), is reached, the repolarisation takes place. This phase concludes with the

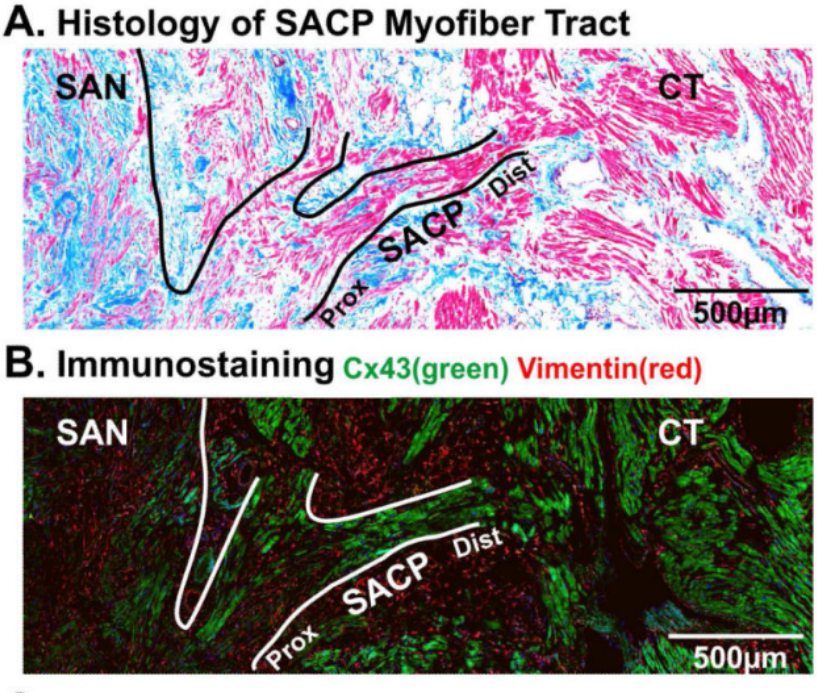

Figure 2.11: SACP histological mapping. A. Masson's Trichrome histological staining with lateral SACP outlined. The blue area coincides with the collagen typical of fibrotic tissue, while the magenta represents the myocites. B. Immunostained sister section to the one shown in panel A. The SACP shows a larger expression of connexin43 (Cx43), compared to the rest of SAN. Figure taken from [20].

maximum diastolic potential (MDP), identified by the minimum of V_m. Lastly, an imbalance between inward and outward currents prevents SANCs from reaching a resting potential, instead a so called DD phase takes place. In this phase the cells slowly depolarise, until they reach a threshold named take off potential (TOP) from which a new upstroke takes place. The TOP can be defined as in Equation (4.8). The time difference between two consecutive OSs is known as cycle length (CL) and is measured in ms. Similarly, the BR describes how many APs occur in a minute and can be calculated as:

$$BR = \frac{60000}{CL}. \tag{2.4}$$

The action potential duration (APD) is measured in ms and is defined as the time that occurs from the TOP to the MDP and, given that the DD is calculated as the time between the MDP and the TOP, it follows that:

$$CL = APD + DD. \tag{2.5}$$

The difference between the value of V_m at the OS and its value at the MDP is instead known as the action potential amplitude (APA).

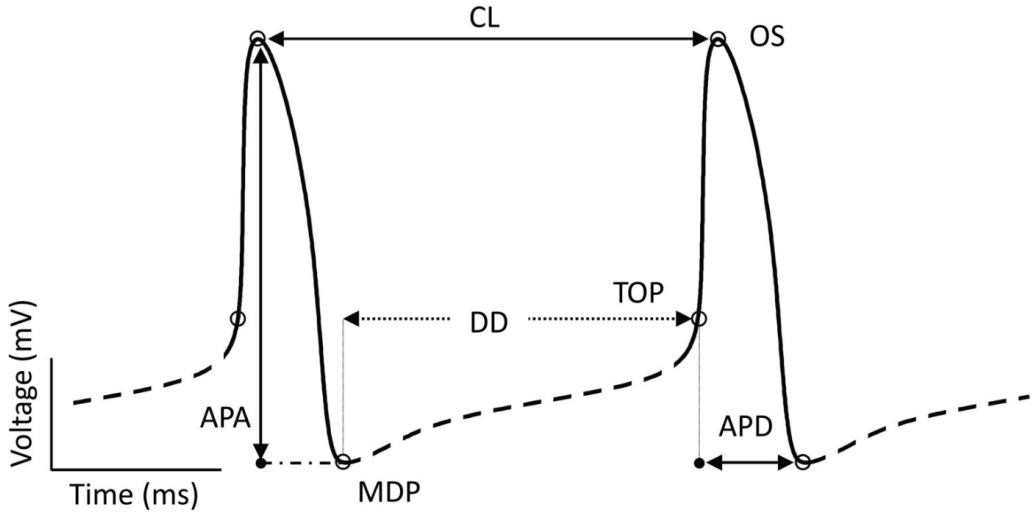

Figure 2.12: Representation of two consecutive APs of a human SANC. Different AP markers are highlighted, namely the OSs, the MDPs and the TOPs. This markers are then used to calculate the APA, the CL, the DD and the APD. Figure taken from [9]

2.2.2.1 Pacemaking Origin

Several theories about the mechanism behind the spontaneous activity of SANCs exist and over the years the general consensus has shifted from one to the other [23]. While it is outside the scope of this manuscript to give an exhaustive overview of all of them, this section will describe the three most relevant ones i.e. I_{K2} decay, *membrane clock* and Ca^{2+} *clock* hypothesis. The reader can find more information in [23, 26].

I_{K2} Decay Hypothesis
The first models of cardiac pacemaking were developed in the sixties by Noble *et al.* [27] for Purkinjie fibres. They were based on the assumption that the decay of an outward K^+ current named I_{K2} would unmask the contribution of inward background Na^+ carrying currents that would cause the DD.
After almost twenty years, this hypothesis would quickly become outdated when in 1979 Brown *et al.* would experimentally show the existence of an inward current activated by hyperpolarisation carrying both Na^+ and K^+ ions in the rabbit SAN. This current would later be named "funny" since no other current had ever been shown to be activated by hyperpolarising potentials.

Membrane Clock Hypothesis
The discovery of the "funny" current I_f, led to a reinterpretation of the mechanism behind pacemaking. In 1981 DiFrancesco *et al.* showed that I_{K2} was actually I_f and therefore the DD phase was not due to the decay of an outward current but to the activation of an inward one.

I_f has a comparatively slow dynamics with respect to other currents, it does not rely on ATP consumption, and it increases in amplitude with adrenergic stimulation while it is inhibited by muscarinic stimulation. These properties make it well suited for the role of pacemaking current.

Ca^{2+} Clock Hypothesis
According to this hypothesis, pacemaking does not depend on the *membrane clock*, but instead to periodic local calcium releases from the SR. These would in turn give rise to the DD thanks to the increased action of the electrogenic sodium calcium exchanger (NCX), which, by exchanging one Ca^{2+} ion from the intracellular space with three Na^{+} ions from the extracellular space causes the net inward I_{NaCa} current [23].

Nowadays the only valid options are the *membrane clock* and the *Ca^{2+} clock* hypothesis, however both of these have their drawbacks.
On one hand, bifurcation analyses performed by varying the maximum conductance for I_f, showed that this current unlike I_{CaL} and I_{Na} does not contribute to equilibrium point destabilisation, suggesting a lesser role in pacemaking.
On the other hand, only minor *in vivo* changes in BR were observed in mice with ≈80% NCX block, in opposition to another experiment showing absence of automaticity with complete block. This discrepancy could be explained by the large reserve of the I_{NaCa} current: the block of the exchanger causes accumulation of Ca^{2+} inside the cell, which in turn increases the activity of the pump thus compensating for the block.
Ultimately the general consensus agrees that both of these mechanisms play a role in determining the automaticity of SANCs. The combination of both the *membrane clock* and the *Ca^{2+} clock*, nowadays known as the *coupled clock*, provides a trade-off in terms of robustness and flexibility unachievable by either clock alone [23].

2.2.2.2 Entrainment

In cardiac modelling and, up to a certain extent, in electrophysiology properties such as APA or APD are often regarded as global characteristics of a tissue e.g. every cell of the SAN has the same APD as all the others, however this could not be further from the truth. When cells are isolated they all show different properties. Then, how is it possible for the thousands of cells in the SAN, each of them with its own BR, to synchronously pace the heart?
The answer lies within gap junction coupling. Like the myocytes of the working myocardium (see Section 2.1.3.3), SANCs are connected with one another by gap junctions.
The resulting electrical connections make SANCs behave as coupled oscillators, allowing them to beat at the same frequency. This process, known as entrainment, is said to be "democratic": the BR to which cells synchronise is not necessarily that of the fastest cells, instead lies within the range of the BRs of individual cells [23].

Entrainment might be mistaken for apparent conduction, with activation spreading radially from faster pacemakers. However it is a different phenomenon, not given by the continuous propagation of a stimulus, but as a consequence of synchronisation [28].
The strength of the coupling determines what becomes the driver for synchronisation: with higher gap junction conductance the tonic components of the DD phase are more important, while with poor coupling the phasic components of the AP drive the synchronisation [28].

2.2.2.3 Cellular Heterogeneity and Fibroblasts

As explained in the previous section, the SAN is constituted by heterogeneous cells, that, thanks to entrainment, give rise to synchronous activity. This heterogeneity, and in particular the spatial distribution of cell properties, might be vital in ensuring the correct pace-and-drive of the atria.

Comparison of Structural Models: Gradient vs. Mosaic
Current research indicates that both the gradient and mosaic models of SAN organization are functionally capable of supporting pacemaking and atrial driving. However, each model faces specific empirical challenges.
The gradient model posits a smooth transition in both cellular electrophysiology and intercellular coupling from the centre to the periphery. Its primary limitation is the lack of direct histological evidence; while peripheral-type cells (larger cells with specific current densities) have been identified, they have not been definitively isolated from the anatomical periphery of the SAN [24]. Furthermore, studies by Monfredi *et al.* found no significant correlation between cell size and current density, suggesting that the SAN may be characterised by a more complex, stochastically distributed heterogeneity rather than a strict spatial gradient [29].
In contrast, the mosaic model suggests that the observed transition in AP morphology is not due to a gradient of SANC phenotypes, but rather to the varying density of atrial cells interspersed within the SAN tissue. Gradients in gap junctional conductance, particularly connexin expression, are known to exist, but their exact ratios and spatial distributions remain experimentally unverified.
Despite these contradictions, computational studies have provided significant insights. Simulations using monodomain models have shown that spatial changes in diffusion coefficients can successfully reproduce central activation [30]. Recent evidence suggests that these two architectures may coexist; mixed gradient-mosaic models, which combine increasing intercellular coupling with a higher density of atrial cells toward the periphery, have demonstrated superior physiological accuracy.
This type of hybrid setup has successfully reproduced key phenomena, including:

1. Central activation and leading pacemaker migration following acetylcholine administration in 2D tissues [31].
2. Physiological CL and conduction velocity (CV) in 3D human models featuring SEPs [11].

Fibroblasts
The presence of fibroblasts around and within the SAN tissue has traditionally been associated with the insurgence of arrhythmias. However, experimental data retrieved from healthy tissue shows that up to 50% of the human SAN is composed by fibrotic tissue. Furthermore, fibroblasts have been shown to be electrically coupled to the myocytes via gap junctions. It is therefore unlikely for the role of fibrosis to be purely pathogenic, instead mounting evidence shows that fibroblast have a positive impact in physiologic pacemaking [23].
Computational studies showed that, depending on density, distribution and coupling strength, fibroblasts modulate the DD and the CV. Furthermore, together with the heterogeneity previously discussed in this section, they increase the safety factor (SF) for conduction [12].

2.2.2.4 Autonomic Nervous System Regulation

The SAN is predominantly innervated by branches of the right vagus nerve. Experimental denervation of the right vagus, or antagonisation of the muscarinic receptors, lead to sudden increases of the BR when this is inferior to 100 beats/min at rest. This shows that at rest, the SAN is under constant parasympathetic tone that brings the intrinsic BR of the SAN (100-110 beats/min) down to the resting HR.
On the other hand, during physical activity, the medullary centres reduce the vagal tone and simultaneously increase the sympathetic activity leading to higher HRs [32].
Further details on the molecular processes behind the autonomic regulation of the BR are given in [8, 33] .

2.3 Kidney Anatomy and Physiology

The kidneys are a pair of bean shaped organs located retroperitoneally between the transverse processes of T12-L3 vertebrae. Their core function is the removal of waste products from the blood, but they also play a crucial role in a plethora of secondary mechanisms related to the maintenance of homeostasis of fluids, ions and acid-base. Furthermore, they have an endocrine function producing renin, erythropoietin and calcitriol. [34]

2.3.1 Anatomy

The kidneys are (Figure 2.13 left) located in the retroperitonoeum just below the diaphragm on either side of the midline. Each of them is about the size of a closed fist, being 5-7 cm wide, 3-5 cm thick, and 10-12 cm long, with an average weight of 135-136 g in women and 160-162 g in men [34]. They consist of the renal parenchyma and the collecting system. The parenchyma comprises the cortex and the medulla, both containing specific segments of nephrons i.e. the functional units of kidneys. The collecting system is the series of conduits that transport the filtrate out of the parenchyma. It begins with the collecting ducts, which

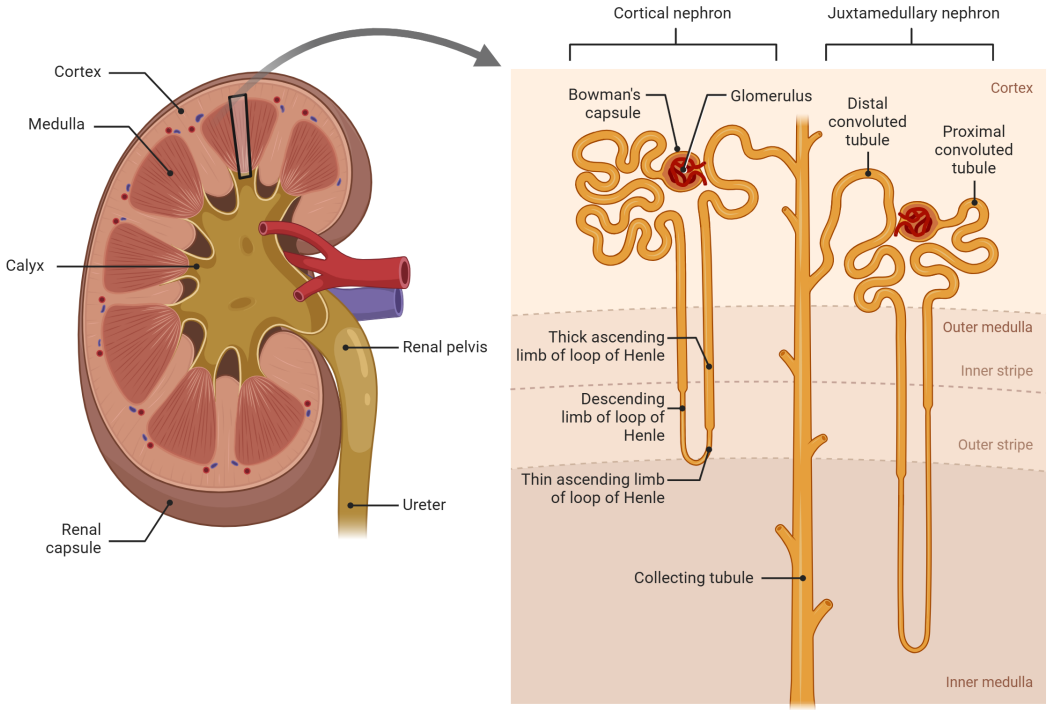

Figure 2.13: Illustration of a kidney on the (left). Representation of cortical and juxtamedullary nephrons (right). Figure created with BioRender.com.

converge at the renal papillae to drain into the minor calyces. These join to form major calyces, which eventually blend into the renal pelvis.

Two different kind of structures make up the cortex: cortical labyrinths and medullary rays. The former can be either glomeruli or proximal and distal convoluted tubules, whereas the latter include straight proximal tubules, loops of Henle and cortical ducts [35].

The medulla is divided into 8-12 so called pyramids, which span from the cortex to the innermost papilla. It is divided into outer and inner medulla. The outer medulla is in turn subdivided into an outer stripe that is in contact with the cortex, and an inner stripe which is in contact with the inner medulla [35].

Nephrons are the structural and functional units of the kidneys. They consist of the glomerulus, also known as renal corpuscle, and the tubule. Depending on the location of the glomerulus, they can be classified into cortical or juxtamedullary nephrons (Figure 2.13 right). Cortical nephrons have their glomeruli in the superficial regions of the cortex and a short loop of Henle that penetrates the outer medulla only. On the other hand, juxtamedullary nephrons have their glomeruli deeper in the cortex, near the corticomedullary boundary, and have longer loops of Henle that reach the inner medulla.

2.3.2 Physiology

The main function of the kidneys is the removal of metabolites and exogenous substances from the blood. In order to achieve this goal, the kidneys, and in particular the nephrons, exploit the principles of filtration, reabsorption and secretion. Indeed, each kidney can be thought of as a black box with a single input, i.e. the renal artery, and two outputs, i.e. the renal vein and the ureter. If a substance appears in the urine, it means that it is being excreted from the body, whereas, if it appears in the renal vein, it means that it is returned to it.
Filtration takes place in the glomerulus; here the difference between the hydrostatic pressure of the glomerular capillaries P_{gc} and that of the Bowman's space P_{bs} drives plasma and solutes outside the capillaries and into the Bowman's space. On the other hand, since proteins are confined inside the capillaries, their oncotic pressure π_{gc} is greater than the oncotic pressure in the Bowman's space π_{bs} (which is almost zero) and opposes the movement of fluids. This process is described by Starling's equation:

$$GFR = L_{\mathsf{p}} S[(P_{\mathsf{gc}} - P_{\mathsf{bs}}) - (\pi_{\mathsf{gc}} - \pi_{\mathsf{bs}})], \tag{2.6}$$

where GFR represents the glomerular filtration rate (GFR), which corresponds to the volume of water filtered out of the plasma through the glomerular capillary walls and into the Bowman's space [36]; L_{p} is the hydraulic permeability and S is the surface available for filtration.
Normal GFR varies from $120\,\mathrm{mL\,min^{-1}}$ to $125\,\mathrm{mL\,min^{-1}}$. The macula densa maintains the GFR constant in spite of changes in systemic and renal artery pressure thanks to a process called autoregulation [36].

Both reabsorption and secretion occur in the tubules. These two processes, together with filtration, determine how much of a given substance is retained in the body. Depending on the balance of these three mechanisms, five different scenarios depicted in Figure 2.14 can occur:

1. **Filtration without reabsorption nor secretion**. Some metabolites are disposed in this way. In this case the excreted amount coincides with the filtered amount.
2. **Filtration with partial reabsorption**. This is what happens to most electrolytes, for which, generally, the excreted amount is way lower than the filtered amount.
3. **Filtration with complete reabsorption** is typical of useful substances such as glucose.
4. **Filtration with complete secretion**. In this case the substance is absent from the renal vein.
5. **Filtration with partial secretion**. In this case the excreted amount is greater than the filtered amount.

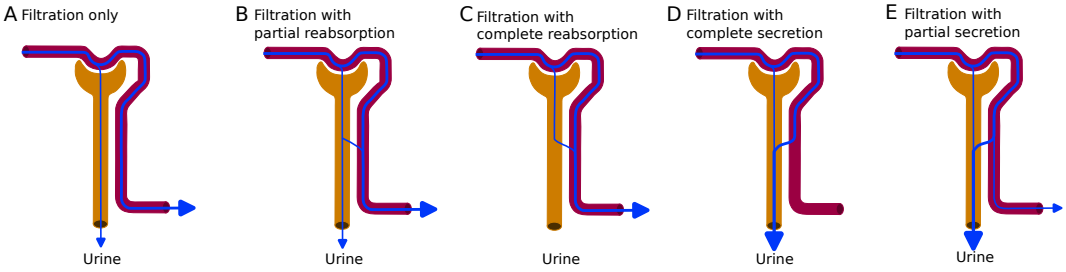

Figure 2.14: Types of filtration and reabsorption. Depending on the type of substance being processed by the kidneys, the different combinations of filtration and reabsorption described in Section 2.3.1 are possible.

2.4 Pathophysiology of Chronic Kidney Disease and Sudden Cardiac Death

This chapter has so far focused on the anatomy and the physiology of two seemingly unrelated organs: the heart (with particular attention to the SAN) and the kidney. In the following, the nuanced interplay of these two structures will be described, with a strong focus on the effects of CKD on the SAN.

2.4.1 Chronic Kidney Disease

The latest guidelines published by Kidney Disease: Improving Global Outcomes (KDIGO) define CKD as *abnormalities of kidney function or structure, present for a minimum of three months, with implication for health* [2]. It is a slowly but continuously progressing syndrome that, as will be described in the following of this section, comes with elevated risk of complications and mortality, often cardiovascular related [37].
CKD is not the result of a single pathology, instead it can arise as the consequence of diabetes, hypertension, chronic glomerulonephritis, chronic pyelonephritis, chronic use of anti-inflammatory medication, autoimmune diseases, polycystic kidney disease, Alport disease, congenital malformations, or prolonged acute renal disease [37].

2.4.1.1 Classification

KDIGO classification of CKD is based on three factors: (C) cause, (G) kidney function determined by GFR (see Section 2.3.2), and (A) degree of albuminuria [2]; and it is therefore named CGA.
In particular, patients are classified based on five GFR stages (Table 2.2) and three albumin excretion ratio (AER) or albuminuria to creatine ratio (ACR) stages (Table 2.3). The combination of these two metrics is often used for estimating the risk of progression of renal dysfunction (Table 2.4). Stage G5 is also known as end stage renal disease (ESRD).

Table 2.2: Stages of GFR. Table adapted from [2, 37].

Category	GFR (ml/min per 1.73 m^2)	Classification
G1	$>= 90$	Normal or high
G2	60-89	Mildly decreased
G3a	45-59	Mildly to moderately decreased
G3b	30-44	Moderately to severely decreased
G4	15-29	Severely decreased
G5	< 15	Kidney failure

Table 2.3: Stages of albuminuria. Table adapted from [2, 37].

Category	AER (mg/24 h)	ACR (mg/g)	Classification
A1	< 30	< 30	Normal to mildly increased
A2	30-300	30-300	Moderately increased
A3	> 300	> 300	Severely increased

Table 2.4: Risk of renal dysfunction progression. Table adapted from [37].

	Albuminuria		
GFR	A1	A2	A3
G1	low risk	moderate risk	high risk
G2	low risk	moderate risk	high risk
G3a	moderate risk	high risk	very high risk
G3b	high risk	very high risk	very high risk
G4	very high risk	very high risk	very high risk
G5	very high risk	very high risk	very high risk

2.4.1.2 Epidemiology

The GBD defines disease "burden" as the impact of a health problem in terms of financial cost, mortality, morbidity, or other indicators. Disease burden can be measured by combining two indicators to describe the disability-adjusted life-years (DALYs): the number of years of life lost to disease and the number of years lived with disability due to disease (see Figure 2.15) [2].

Globally, in 2017, a systematic analysis from the all-age GBD project found 697.5 million (95% uncertainty interval (UI): 649.2–752.0) cases of all-stage CKD, for a global prevalence of 9.1% (8.5%–9.8%). By 2021, a joint statement from the American Society of Nephrology, European Renal Association, and International Society of Nephrology indicated that more than 850 million people suffer from some form of kidney disease, roughly double the number of people who live with diabetes (422 million) and 20 times more than the prevalence of cancer worldwide (42 million) or people living with AIDS/HIV (36.7 million). In 2017,

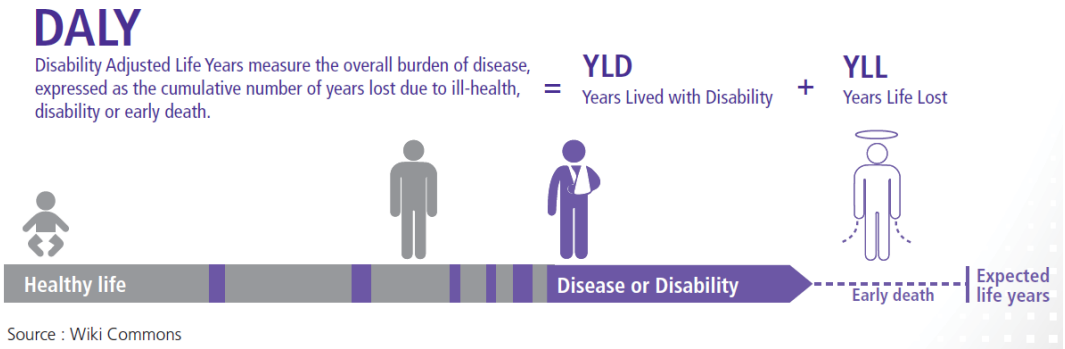

Figure 2.15: DALYs diagram. DALYs are calculated as the sum of the years of life lost (compared to the life expectancy) and years lived with disability. Figure taken from [38].

CKD was estimated to account for 35.8 million (95% UI: 33.7-38.0) DALYs, and 1.2 million people died from CKD [2].

2.4.1.3 Treatment Options

As highlighted in Section 2.3, the kidneys perform a wide array of functions essential for life. Therefore, when their residual function gets reduced, it is important for the patient to find strategies to ensure sufficient quality of life in the form of kidney replacement theraphy (KRT).
There is no threshold in laboratory exam results to decide whether to initiate KRT, instead the following factors are evaluated: aspects of quality of life, psychological aspects associated with the anxiety of undergoing complex therapy, the perception of the nephrologist on the health state of the patient, the decline of renal function, and the risks associated with renal replacement therapy [37].
The optimal care model presented in [2] suggests that patients in category G4 should be educated on KRT (Figure 2.16). Indeed, its ultimately the patient who decides which kind of KRT option to go for, and, unless medical contraindications exist, patients decision must be respected [39]. In the following a brief overview of the current most common KRTs is given.

Renal Transplant
Allograft renal transplantation is the most preferred form of renal replacement therapy. However only about 16,000 transplants are performed annually in the US while over 100,000 patients are in the waiting lists. Furthermore, the elderly and those with multiorgan failure are generally excluded from receiving a transplant given the risks associated with surgery and post surgery immunosuppresion [39]. Therefore, people ineligible for or unwilling of transplantation, or those needing an alternative therapy while waiting for organ availability

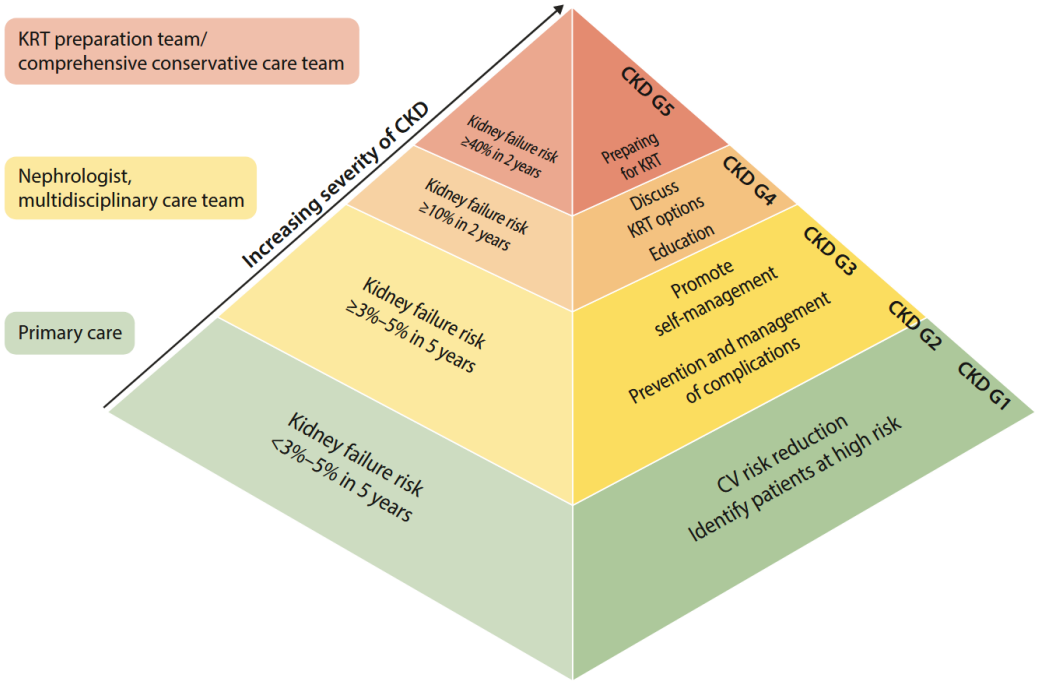

Figure 2.16: Optimal care model. As the disease progresses, different strategies and levels of care are required. KRT strats to be considered from level G4. Figure taken form [2]

are forced to seek other options, namely HD or peritoneal dialysis (PD).

Dialysis

During dialysis, the toxic metabolic waste products from the blood compartment are removed when the blood is run across a semi-permeable membrane (artificial or natural), resulting in 'clearance of blood' of the toxic metabolic waste. In the U.S., large majority of patients are on HD, approximately 86% as opposed to only 14% on PD. The overwhelming preference of HD over PD is an enigma and is a subject of intense discussion among the leadership in the community. The subject is a complex issue and is multi-factorial. Although there is no survival advantage with either of the dialysis therapy over four to five years, several non-medical factors, like economics of dialysis, lack of well trained dialysis team and psychological factors have been implicated in the biased preference of one form of dialysis over the other [39].

In PD, the dialysis solution (2 to 2.5 liters) is instilled in the peritoneal cavity within 15 to 20 minutes using a pre-inserted PD catheter. This is followed by a 'dwell time' ranging from four, six or twelve hours (depending upon the individual patient's membrane type) in which the dialysis solution comes in contact with the peritoneal membrane. During this process, the transfer of solute and fluid takes place across the peritoneal membrane by the process of diffusion, (driven by concentration gradients across the membrane) and by convection (driven by osmotic and hydrostatic pressure gradients). Different solutes, based on their

molecular size, equilibrate differently during the dwell time. At the end of the pre-determined dwell time, equilibrated dialysate is then 'drained' out and the next 'exchange' is started [39].

In HD, the patient is connected via a double catheter to the dialysis machine, which takes blood from a vein and, after cleaning it, pumps it back into an artery. The core of the machine is the filter or dialyser, where blood is pumped through thousands of hollow fibres while, at the same time, the dialysate runs in the opposite direction on the outside of said fibres. Inside the filter, the principles of diffusion, convection and ultrafiltration are exploited to remove unwanted solutes and fluids from the blood. Diffusion is the movement of solutes across a semipermeable membrane from regions of high solute concentration to regions of low solute concentration. Ultrafiltration occurs when a fluid moves across a semipermeable membrane as a result of a pressure gradient being applied across the membrane. Convection is the process of solute movement across the membrane thanks to the movement of the liquid because of ultrafiltration.
Patients with ESRD routinely undergo HD three times per week interspersed by two 48 h short interdialytic period (SIDP) and one 72 h long interdialytic period (LIDP).

2.4.1.4 Sudden Cardiac Death in Haemodialysis Patients

SCD is defined as sudden, unexpected death caused by loss of heart function (sudden cardiac arrest). In general, SCD events are defined as those deaths that are either preceded by a witnessed collapse, or occur within one hour of an acute change in clinical condition, or occur within twenty-four hours since the deceased individual was known to be in his or her usual state of health. It is the largest cause of natural death in the U.S. with estimated risk-adjusted incidence of sudden cardiac arrest of 76 per 100,000 per year (≈230,000 per year in the United States) [5].
About 25% percent of HD patients die because of SCD, a 100-fold increase compared to the general population [6] and a 14-fold increase compared to subjects with a history of cardiovascular disease (CVD) and normal kidney function [5]. SCD episodes are not uniformly distributed in time, with a 50% increase occurring at the end of the LIDP [4].
Furthermore, studies with implanted loop recorders showed that the terminal rhythm leading to SCD in HD patients is sinus bradycardia followed by asystole [3, 4].
In 2019 Loewe *et al.* investigated the effect of altered electrolyte levels on SAN pacemaking in a computational study and found out that hypocalcaemia, in particular, slows down the BR [1]. This was later confirmed in 2024 by Santini *et al.* , who reported a unique case of an 80-year-old woman who experienced sinus arrest followed by bradycardia, which was caused by severe iatrogenic hypocalcaemia. Normal sinus node function was successfully restored during the hospitalisation [7].
Furthermore the ANS is frequently dysfunctional and imbalanced in HD patients with sympathetic overactivity driven by afferent sensory renal nerves stimulated by renal injury. CKD was also associated with a reduced BR response to sympathetic stimulation, and it was found that an abrupt reduction in sympathetic tone acutely precedes SCD in a rat model [6].

Chapter 3

Mathematical Fundamentals

In this chapter the basic mathematical concepts upon which this project has been developed on will be presented. The chapter starts with the description of cell models, and how these have historically been used for single-cell simulations. In the same section, the Severi rabbit SANC model [40] and how it was modified to introduce the effects of the ANS [8] are described. Next, the chapter will cover the basics of tissue simulations, giving a brief overview of the possible strategies to represent the electrical activity of the heart at the tissue-level, and finally explaining the simplified Kirchhoff network model (SKNM) [41]. Lastly the basics of FEM will be introduced.

3.1 Single-Cell Models

Cardiac cell models mathematically describe the course of APs using systems of ordinary differential equations (ODEs). These can represent the ionic currents due to voltage gated ion channels, the changes in the concentration of ions due to their movement between the compartments of the cell and the extracellular space, and the overall effect of these phenomena on V_m.

3.1.1 Hodgkin and Huxley Formalism

This way of describing the APs of cardiomyocytes arises from the pioneering work of Alan Hodgkin and Andrew Huxley, who in 1952 published the first model of an excitable cell [42]. By using the newly developed voltage clamp technique on the giant axons of squids (not on the axons of giant squids as often reported) they were able to describe the dependence of ionic currents on V_m. This work won them the 1963 Nobel Prize in Physiology or Medicine. In the Hodgkin and Huxley model, the cell membrane is represented by an electrical equivalent circuit (as shown in Figure 3.1) constituted by a capacitor in parallel with three branches each of which contains a variable conductance in series with a voltage generator. The

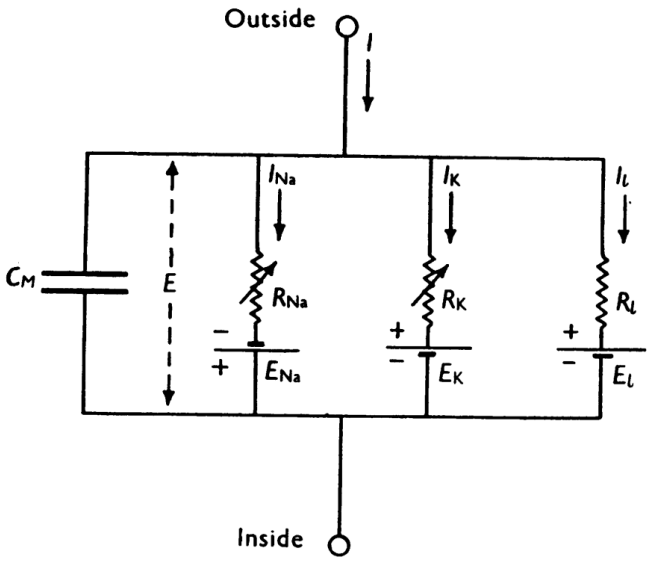

Fig. 1. Electrical circuit representing membrane. $R_{Na}=1/g_{Na}$; $R_K=1/g_K$; $R_l=1/\bar{g}_l$. R_{Na} and R_K vary with time and membrane potential; the other components are constant.

Figure 3.1: Equivalent circuit of the cellular membrane of the squid giant axon from the groundbreaking work of Alan Hodgkin and Andrew Huxley. The variable conductances represent the permeability of the membrane to ions, while the voltage generators represent the Nerst potentials for a given ion. Figure taken from [42].

capacitor represents the phospholipidic bilayer, the conductances model the permeability of the ion channels while the generators represent the Nerst potentials.

In the Hodgkin-Huxley scheme each ionic current, I_i, is macroscopically represented as the result of the flow of ions through a large ensemble of ion channels. Therefore, it can be calculated as the product between its conductance g_i and a driving force given by the difference between V_m and its Nerst potential E_i, and is typically expressed as current density through a unit area of membrane [43]:

$$I_i = g_i(V_\mathrm{m} - E_i). \tag{3.1}$$

The conductance, g_i, is computed as a function of parameters (hypothetical *gates*) that provide voltage and time dependence. In particular the value of the conductance for the ion i is given by:

$$g_i = \bar{g}_i \prod_j \gamma_j, \tag{3.2}$$

where $\bar{g}_i$ is the maximum conductance for the ion i, and γ_j are the gates.

Each gate γ_j can transition from 0 (*closed* position) to 1 (*open* position) or vice versa as V_m changes. The position of a given gate and its rate of transition are assumed independent of the positions of all other gates. The evolution in time of γ_j follows a first order kinetics:

$$\frac{d\gamma_j}{dt} = \alpha(1-\gamma_j) - \beta\gamma_j, \tag{3.3}$$

where α and β are the V_m dependent opening and closing rates, respectively; while γ_j is the *open* probability and $1-\gamma_j$ is the *closed* probability.
The Hodgkin and Huxley model uses only three voltage dependent gates: one for the potassium and two for the sodium channels. The model is thus constituted by a system of four ODEs, the fourth being the equation for the membrane potential:

$$C_m \frac{dV_\mathsf{m}}{dt} = -[g_{Na}(V_\mathsf{m} - E_{Na}) + g_K(V_\mathsf{m} - E_K) + g_l(V_\mathsf{m} - E_l)] - I_{stim}. \tag{3.4}$$

The Hodgkin and Huxley model inspired the work of Denis Noble, who in 1962 adapted it to the Purkinje fibres and published the first electrophysiological model of a cardiac cell [44]. Since then models have grown in complexity and have specialised to represent the different cells present in the heart.

3.1.2 Severi DiFrancesco Model

The Severi DiFrancesco (SDiF) model describes the AP of rabbit SANCs. It does so with 33 ODEs that describe both membrane currents and ion concentrations within the intracellular compartments of the cell.
Its parent model, i.e. the Maltasev and Lattakka 2009 model, features a *coupled clock* architecture where both the Ca^{2+} *clock* and the *membrane clock* work in synergy to achieve pacemaking. However, it fails to reproduce the reduction in BR experimentally observed upon I_f block in rabbit SAN preparations.
The SDiF model builds on its predecessor by keeping the same detailed calcium handling while retaining only the membrane mechanisms for which clear experimental evidence is available for a quantitative relevant contribution to rabbit SAN activity. Furthermore, several currents, pumps and exchangers are reformulated based on experimental data.
The SDiF model is built on the hypothesis that I_f is the main inward current until the late DD. This enables rapid and energy-efficient regulation of the CL, as modulation is achieved solely by adjusting the magnitude of this current during early DD. A further strength of the model is that the net diastolic current (I_{net}) arises from the balance between relatively small inward (I_{in}) and outward (I_{out}) currents. The reliance on smaller inward and outward currents minimises the required transmembrane ion fluxes to maintain ionic gradients, thereby supporting more energy-efficient pacemaking through reduced sodium–potassium pump activity [23].

3.1.3 Extended Severi DiFrancesco Model

One limitation of the SDiF model is that it cannot model the effects of graded concentrations of isoprenaline (ISO), which can only be ON (1 µM) or OFF (0 µM). ISO is commonly used in vivo to simulate the effect of sympathetic stimulation. Indeed it binds to the same β-AR receptors to which adrenaline and noradrenaline bind.
To overcome this limitation, Linder *et al.* included in the model the β-AR cascade described by [33] (see Figure 3.2), which directly models the effects of ISO on I_f, I_{CaL} and a number of

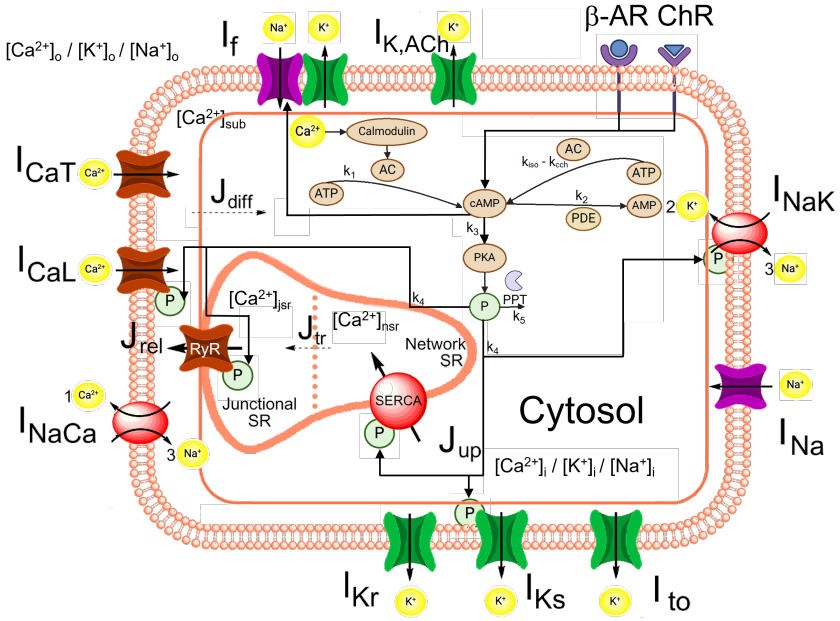

Figure 3.2: The extended SDiF model, with the representation of the β-AR cascade described by Behar *et al.* and its effects on the BR. Figure adapted from [8]

other currents relevant for Ca^{2+} handling (SR uptake J_{up} and release J_{rel}) and pacemaking. The extended model was then validated against new Langendorff-perfused rabbit heart experiments and literature data [8].

3.2 Tissue Simulations

While membrane models offer great insights in the functioning of isolated cells, they cannot recapitulate complex physiological behaviours, e.g. conduction, nor pathological ones, e.g. reentries, observed at the tissue level. Therefore, different strategies have been developed to simulate tissue patches, particular structures, chambers or even the whole heart.
These approaches can be defined as 'spatial models' and, as shown in Figure 3.3, allow for different levels of approximation of the cardiac tissue and, in turn, different computational costs.

Bidomain
On one end of the spectrum there is the bidomain model. In this representation of the cardiac tissue the membrane, the extracellular space, and the intracellular space are distributed uniformly in the computational domain. It allows the representation of complex interactions between the tissue and the surrounding environment, e.g. the effects of pacing or cardioversion through extracellular electrodes. However, it relies on the homogenisation of the properties of cells within the domain, meaning that cells are not individually represented and therefore it does not allow the analysis of variables at the cell scale. Furthermore, even

if the domain discretisation is refined, cardiomyocytes do not appear in the mathematical model: after homogenisation, the myocytes are no longer part of the models regardless of the mesh resolution [41].
On the other hand, the simplification of the model that comes with homogenisation makes bidomain computationally efficient for whole heart simulations.

$$C_m \frac{dV_\mathrm{m}}{dt} = \beta^{-1}[\nabla \cdot (M_i \nabla V_\mathrm{m})] - \nabla \cdot (M_i \nabla \phi_e) - I_\mathrm{ion}(s, V_\mathrm{m}), \tag{3.5}$$

$$\nabla \cdot (M_i \nabla V_\mathrm{m}) + \nabla \cdot [(M_i + M_e)\nabla \phi_e] = 0, \tag{3.6}$$

$$\frac{ds}{dt} = F(s, V_\mathrm{m}), \tag{3.7}$$

Monodomain
A simplification of bidomain comes if one assumes that the extracellular conductivity is proportional to the intracellular conductivity in every direction:

$$M_e = \lambda M_i. \tag{3.8}$$

Monodomain is a more efficient method compared to bidomain, that however lacks the ability to model the interaction of the tissue with extracellular electrodes.

$$C_m \frac{dV_\mathrm{m}}{dt} = \beta^{-1} \frac{\lambda}{\lambda + 1} \nabla \cdot (M_i \nabla V_\mathrm{m}) - I_\mathrm{ion}(s, V_\mathrm{m}), \tag{3.9}$$

$$\frac{ds}{dt} = F(s, V_\mathrm{m}). \tag{3.10}$$

Extracellular-Membrane-Intracellular Models
On the other end of the spectrum there are extracellular-membrane-intracellular (EMI) models, which represent each cell individually allowing for sub cellular resolution. This means that not only the properties of the tissue can be changed on a cell basis, but that they can vary within every single cell. Yet, these models require extremely fine meshes, dramatically increasing the computation time required for simulations and relegating their use to the

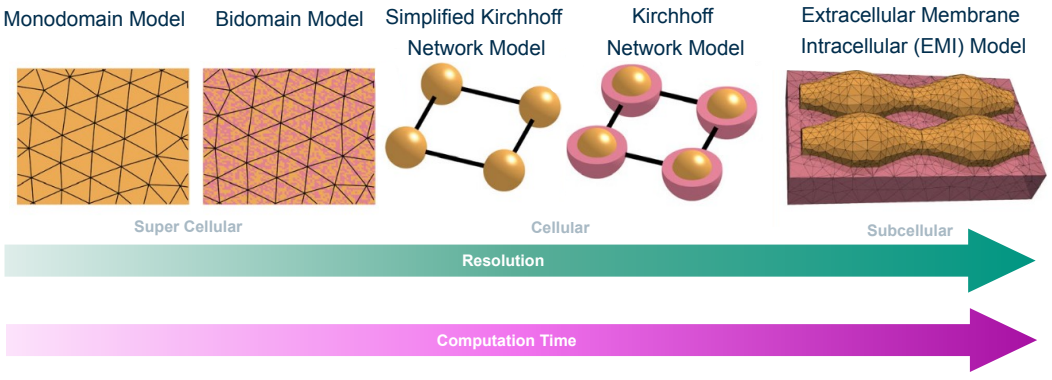

Figure 3.3: Representation of the different levels of approximation achievable by using monodomain, bidomain, Kirchhoff network model (KNM), SKNM or extracellular-membrane-intracellular (EMI) models. Figure adapted from [45].

simulation of small tissue slabs. If interested, the reader can find the equations for the EMI models in [46].

Kirchhoff Network Model

The Kirchhoff network model (KNM) developed by Jaeger *et al.* represents each myocyte and allows manipulation at the cellular level, and between cells, but not within individual cells. It therefore constitutes a compromise between the spatial resolution of EMI models and the computational efficiency of bidomain. Actually, when the tissue slab being simulated is particularly small, and the mesh resolution approaches the cell size, KNM is faster than bidomain. This is not the case when bigger portions of the heart are simulated, as in this case the number of cells needed by the KNM becomes extremely large, while the bidomain mesh can be coarsened.

The equations for KNM can be derived, as in [47], by thinking at each cell and the extracellular space surrounding it as nodes in a computational grid. The currents between neighbouring nodes are calculated in accordance to Ohm's current law:

$$I_i^{j,k} = G_i^{j,k}(\phi_i^j - \phi_i^k), \tag{3.11}$$

$$I_e^{j,k} = G_e^{j,k}(\phi_e^j - \phi_e^k). \tag{3.12}$$

where $G_i^{j,k}$ and $G_e^{j,k}$ represent the conductances in mS connecting the intracellular and the extracellular spaces, respectively, of cells j and k. Furthermore, I_m^k i.e. the total current flowing through the membrane of cell k, from the intracellular to the extracellular space, is given by:

$$I_m^k = A_m^k[C_m \frac{dV_\mathsf{m}^k}{dt} + I_\mathsf{ion}^k(s^k, V_\mathsf{m}^k)]. \tag{3.13}$$

By applying Kirchhoff's current law to a cell, the current flowing out, i.e. I_m^k, must equal the sum of those flowing in from the N^k neighbouring cells:

$$I_m^k = \sum_{j \in N^k} I_i^{j,k}. \tag{3.14}$$

Similarly, the application of Kirchhoff's current law to the extracellular space yields:

$$I_m^k + \sum_{j \in N^k} I_e^{j,k} = 0. \tag{3.15}$$

Using Equation (3.14) in Equation (3.15):

$$\sum_{j \in N^k} I_i^{j,k} + \sum_{j \in N^k} I_e^{j,k} = 0. \tag{3.16}$$

Finally, rearranging Equation (3.13) and substituting I_m^k with Equation (3.14) returns the Equation (3.17) that together with Equation (3.16) and Equation (3.19) constitutes the KNM system:

$$C_m \frac{dV_\mathsf{m}^k}{dt} = \frac{1}{A_m^k} \sum_{j \in N^k} I_i^{j,k} - I_\mathsf{ion}^k(s^k, V_\mathsf{m}^k), \tag{3.17}$$

$$\sum_{j \in N^k} I_i^{j,k} + \sum_{j \in N^k} I_e^{j,k} = 0. \tag{3.18}$$

$$\frac{ds^k}{dt} = F(s^k, V_{\mathsf{m}}^k). \tag{3.19}$$

Equations (3.17) and (3.18) can be rearranged to resemble those of bidomain as shown in [41]:

$$C_m \frac{dV_{\mathsf{m}}^k}{dt} = \frac{1}{A_m^k} \sum_{j \in N^k} [G_i^{j,k}(V_{\mathsf{m}}^j - V_{\mathsf{m}}^k) + G_i^{j,k}(\phi_e^j - \phi_e^k)] - I_{\mathsf{ion}}^k(s^k, V_{\mathsf{m}}^k), \tag{3.20}$$

$$\sum_{j \in N^k} G_i^{j,k}(V_{\mathsf{m}}^j - V_{\mathsf{m}}^k) + \sum_{j \in N^k} (G_i^{j,k} + G_e^{j,k})(\phi_e^j - \phi_e^k) = 0. \tag{3.21}$$

3.2.1 Simplified Kirchhoff Network Model

The SKNM is designed as computationally efficient approximation of the KNM. As its parent model, it represents each cell individually, allowing the manipulation of the membrane properties of individual cells and of each connection [41].
In the same way in which bidomain can be reduced to monodomain, the KNM can be approximated with the SKNM if one assumes that:

$$G_e^{j,k} = \lambda G_i^{j,k}. \tag{3.22}$$

Using Equation (3.22) and following the steps reported in [41] the SKNM equations are obtained:

$$C_m \frac{dV_{\mathsf{m}}^k}{dt} = \frac{1}{A_m^k} \frac{\lambda}{\lambda + 1} \sum_{j \in N^k} G_i^{j,k}(V_{\mathsf{m}}^j - V_{\mathsf{m}}^k) - I_{\mathsf{ion}}^k(s^k, V_{\mathsf{m}}^k), \tag{3.23}$$

$$\frac{ds^k}{dt} = F(s^k, V_{\mathsf{m}}^k). \tag{3.24}$$

3.2.2 Finite Element Method

As it will be described in Chapter 4, openCARP was used to perform simulations with a surrogate of the SKNM. It is a software commonly used to solve monodomain or bidomain problems and it does so by exploiting the FEM. To understand the limitations that come with implementing the SKNM in openCARP, it is necessary to introduce the basics of FEM.
FEM is commonly used to numerically solve partial differential equations (PDEs). The method takes its name from the spatial discretisation of the domain in finite elements. This step, also known as meshing, is the first to be performed in the procedure and consists of subdividing the domain Ω in non overlapping domains Ω^m [48], so that:

$$\Omega = \bigcup_{m=1}^{N} \Omega^m, \tag{3.25}$$

$$\Omega^m \cap \Omega^n = 0 \text{ for } m \neq n. \tag{3.26}$$

The elements are geometrically simple shapes, such as tetrahedrons and prisms in three-dimensional space, quadrilaterals and triangles in two-dimensional space, or lines in mono-dimensional space. Commonly, node points are placed at the corners of the elements, and are shared between adjacent elements.
Node variables are attributed to the node points, and describe the values of the solution function u, e.g. the value of V_m, at the nodes.
To allow the determination of the value of the solution function u at any point x in the domain Ω, node variables are interpolated through the use of shape functions ϕ_i^m, which are local to the elements Ω^m. The interpolation is generally carried out through the summation of the shape functions [48]:

$$u(x) = \sum_{i=1}^{N} \phi_i^m u_i^m. \tag{3.27}$$

By applying the Galerkin weighted residual method, the continuous problem is transformed into a discrete system. In the context of the monodomain equation, two fundamental matrices arise from the integration of shape functions over the element domains Ω^m: the stiffness matrix $\mathbf{K}$ and the mass matrix $\mathbf{M}$.

Stiffness Matrix
The stiffness matrix $\mathbf{K}$ represents the diffusive properties of the tissue, governing the spatial spread of the electrical potential. For a single element e, the local entries k_{ij}^e are defined by the integration of the gradients of the shape functions:

$$k_{ij}^e = \int_{\Omega_e} \nabla\phi_i \sigma \nabla\phi_j \mathrm{d}\Omega_e, \tag{3.28}$$

where σ represents the conductivity tensor. In openCARP, the unit of the elements of the stiffness matrix is [mS].

Mass Matrix
The mass matrix $\mathbf{M}$ accounts for the capacitive nature of the cell membrane and the temporal evolution of the system. The consistent local entries m_{ij}^e are defined as:

$$m_{ij}^e = \int_{\Omega_e} \phi_i \phi_j \mathrm{d}\Omega_e. \tag{3.29}$$

In openCARP, the unit of the elements of the mass matrix is [$\mu\mathrm{m}^3$].
Mass lumping is a numerical technique employed to accelerate the solution of the parabolic step of the FEM (see also Appendix A), and it is enabled by default in openCARP. By summing the entries of the consistent mass matrix row-wise, a diagonal lumped mass matrix is obtained:

$$m_{ii}^{e,\mathrm{lump}} = \sum_j m_{ij}^e. \tag{3.30}$$

Chapter 4

Methods

4.1 Discrete Coupling Mechanism

To preserve the advantages of the SKNM (see Section 3.2) while using openCARP, monodomain simulations were conducted on a mesh composed exclusively of one-dimensional line elements. The resulting mesh comprised 1,600 uniformly spaced nodes, with each node connected to its four nearest neighbours as illustrated in Figure 4.1.
This configuration enabled node-wise adjustment of cellular properties through the adjustment file functionality in openCARP. Simultaneously, because each element connects exactly two cells, the properties of intercellular coupling could be modified by altering the conductivity assigned to individual elements through the `gregions` command [49].

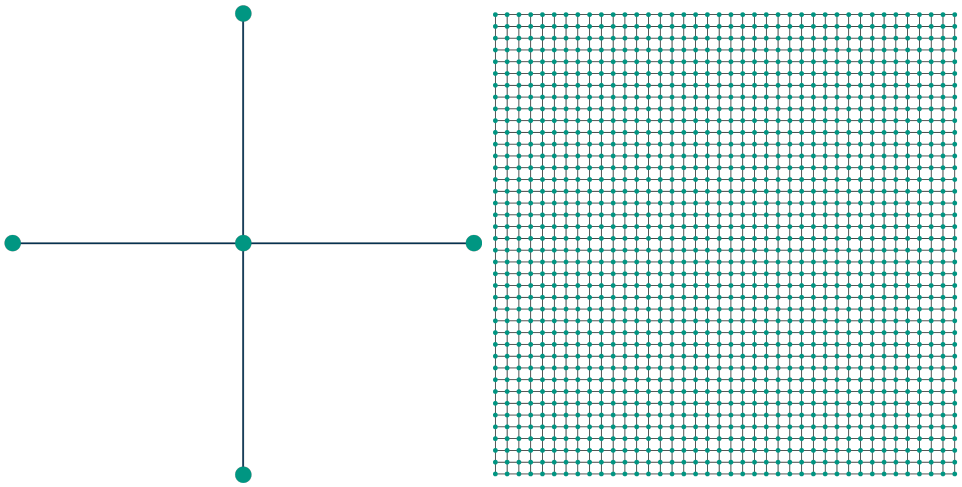

Figure 4.1: Representation of the mesh used to reproduce the SKNM in openCARP. Each node is connected to its four nearest neighbours by mono-dimensional line elements (left). Because the nodes are uniformly spaced, the resulting pattern is a uniform grid where the elements are aligned to the two orthogonal directions (right).

The meshes were generated through a python script that created the *.elem*, *.block* and *.lon* files required by openCARP.

4.1.1 Verification of the Discrete Coupling Mechanism

To assess the correctness of the present implementation, it was benchmarked against the code provided in the supplementary material of Jæger *et al.* [41], which will hereafter be referred to as the reference implementation. Since the used human induced pluripotent stem cell model was not available in the openCARP model repository, nor in CellML format, we opted instead to incorporate the comparatively simple Aliev–Panfilov model [50] into their existing code base.

Both implementations were tested on a 40×40 mesh, with a resolution of 16 µm. A stimulus current of $100\,\mu\mathrm{A\,cm^{-2}}$ was applied to the 10 central cells of the two leftmost columns of the grid for 20 ms. The local activation time (LAT) was defined as the time of crossing of the -20 mV threshold. The LATs of the 10^{th} and the 35^{th} cell along the central row of the patch were used to calculate the CV in the patch as follows:

$$CV = \frac{x_{35} - x_{10}}{LAT_{35} - LAT_{10}}, \tag{4.1}$$

where x_{35} and x_{10} are the spatial x coordinates, and LAT_{35} and LAT_{10} are the LATs of the 10^{th} and the 35^{th} cell, respectively.

The conduction velocity was tested for different levels of intercellular coupling, in the isotropic case. The entity of the intercellular coupling was determined by the intracellular G_i and the extracellular G_e conductances, which are given by:

$$G_i = \frac{1}{\frac{l}{\delta_i A \sigma_i} + R_g}, \tag{4.2}$$

$$G_e = \delta_e \frac{A\sigma_e}{l}, \tag{4.3}$$

where δ_e is the extracellular volume fraction and $\delta_i = 1 - \delta_e$ is the associated intracellular volume fraction. σ_i and σ_e are the intracellular and extracellular conductivities, respectively. A is the cross-sectional area between adjacent cells and l is the distance between their centres. R_g is the gap junction resistance.

Since in openCARP the only parameters affecting the coupling are the intracellular g_i and the extracellular g_e conductivities assigned to the elements, we set them according to the following formulas:

$$g_i = \frac{\delta_i \sigma_i}{1 + \delta_i \sigma_i l_z R_g}, \tag{4.4}$$

$$g_e = \delta_e \sigma_e, \tag{4.5}$$

where we assumed $l_z = l(1 + \delta_e)$ as in Jæger *et al.* [41].

This allowed us to have the same parameters determining the coupling in both the openCARP and the reference implementations of the SKNM. For the verification we set $l = 16\,\mu\text{m}$, $\delta_e = 0.2$, $\sigma_i = 0.4\,\text{S}\,\text{m}^{-1}$ and $\sigma_e = 2\,\text{S}\,\text{m}^{-1}$. R_g was varied between $500\,\text{k}\Omega$ and $10\,\text{M}\Omega$.

4.2 Sinoatrial Node Tissue Simulations

To investigate the effects of hypocalcaemia and the compensatory response of the ANS, a square patch similar to the one exploited for the verification was used. The mesh was still constituted by 1,600 nodes equally spaced in a 40×40 grid. The extended SDiF model [8] was assigned to the nodes of the mesh and therefore a resolution of $70\,\mu\text{m}$ was set to match the cell size.

4.2.1 Population of Models

Inspection of Equation (3.23) reveals that assigning an identical ionic model to every node within the patch is effectively equivalent to performing the same single-cell simulation at each node. Indeed, the term representing the current exchanged with neighbouring cells vanishes, as there is no difference in V_m between adjacent cells, and the equation reduces to:

$$C_m \frac{dV_\text{m}^k}{dt} = -I_\text{ion}^k(s^k, V_\text{m}^k). \tag{4.6}$$

Furthermore, channel proteins half-lives range from hours to days, and are affected by genetic environmental and temporal factors [51, 52] leading to pronounced parameter uncertainty and heterogeneity. Therfore, we elected to recapitulate the physiological variability observed in the SAN through the use of a population of models (POM).

The population was created by a Latin Hypercube Sampling of the 12-dimensional parameter space comprising the permeabilities, the maximum conductances and the rate constants of the SDiF model depicted in Figure 4.2. Each parameter was varied between 0.25 and 4 times its baseline value to obtain a space-filling and physiologically broad initial particle population, which ultimately consisted of 500 different parameter sets. For each sampled parameter vector, the extended SDiF model was simulated for 250,000 ms, and five action potential biomarkers were extracted from the last 5,000 ms of the simulation: (1) $\frac{dV_\text{m}}{dt}_{max}$, computed as the maximum of the first-order time derivative of the transmembrane voltage; (2) APD50, defined as the interval between $\frac{dV_\text{m}}{dt}_{max}$ and the time point at which V_m repolarised to 50%; and the biomarkers already defined in Section 2.2.2, namely (3) OS, (4) CL, and (5) MDP. A log-likelihood was then computed by evaluating each biomarker under its corresponding one-dimensional kernel density estimation derived from experimental data. Starting from this uniformly distributed particle set, a sequential Monte Carlo (SMC) scheme gradually shifted the population towards the target distribution as in Lawson *et al.* [51]. After each iteration,

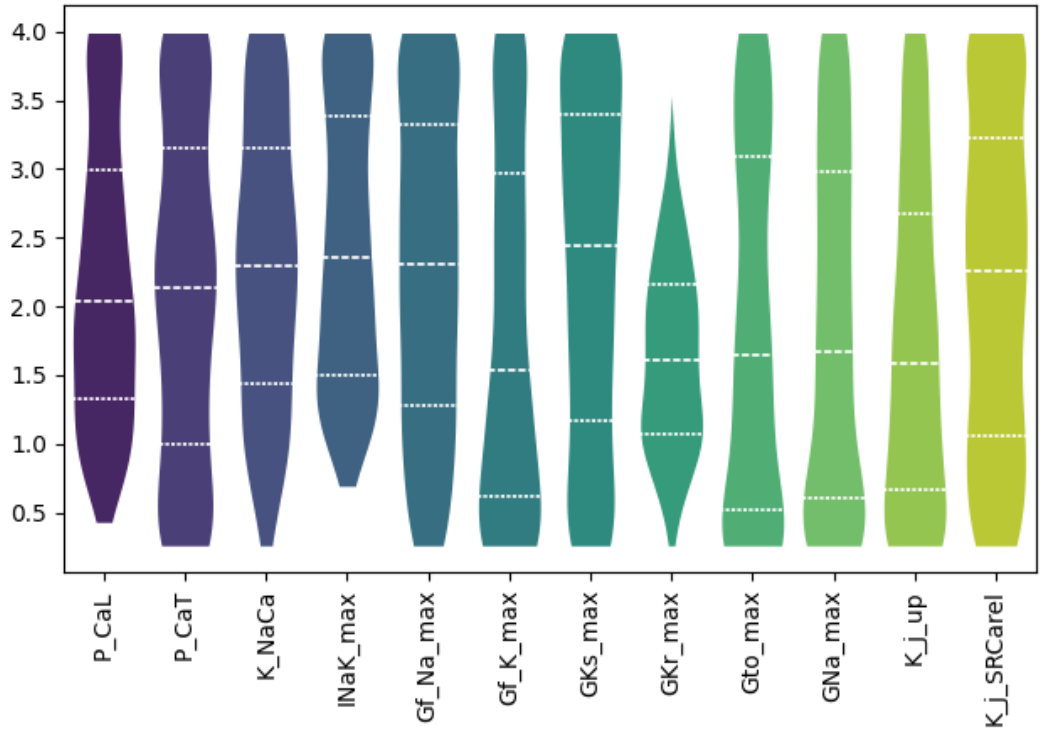

Figure 4.2: Violin plot representation of the distribution of the parameters sampled to produce the POM. Each parameter was varied between 0.25 and 4 times its baseline value. Variants were generated by sampling the resulting parameter space. Only those which fell within the experimental range and which did not produce numerical error in 1,000 s long simulations with $[Ca^{2+}]_o = 0.6, 0.8$ and 1.2 mM and $[ISO] = 28, 90$ and 170 nM were selected to be part of the final population.

particles were resampled according to their importance weights and rejuvenated using a custom Metropolis–Hastings move that combined Gaussian random walks in parameter space with Gaussian mixture model-based proposals in a transformed latent space. The final SMC population thus consisted of parameter sets approximately distributed according to the tempered posterior, forming a calibrated POM consistent with the experimental biomarker distributions.

Finally only the baseline variants that fell within the $\pm 3\sigma$ interval of the experimental distributions and which did not produce numerical errors when simulated for 1,000 s under the influence of different $[Ca^{2+}]_o = 0.6$, 0.8 and 1.2 mM and $[ISO] = 28$, 90 and 170 nM were retained in the population. The distribution of the sampled parameters in the final population is presented in Figure 4.2.

After the selection process, the POM consisted of 356 variants which were randomly assigned to the nodes of the mesh exploiting the adjustment file functionality of openCARP. Because the number of nodes (1,600) was greater than the number of variants, there are multiple instances of the same variants in the patch.

4.2.2 Intercellular Coupling

Given that the results of the verification (see Chapter 5) showed scarce agreement between the openCARP and the reference implementation of the SKNM, and considering that other studies, such as [9, 12], did not explicitly separate the contributions of intracellular conductivity and gap junctional conductance to the overall intercellular coupling, we adopted the following formulation for the conductivities assigned to the line elements of the mesh:

$$g_i = g_e = 2\frac{l_e}{\tilde{A}R}, \tag{4.7}$$

where l_e represents the length of the element and coincides with the mesh resolution, R is the desired coupling resistance and is measured in MΩ, and $\tilde{A}$ is the cross-sectional area of the line element and corresponds to 1 μm^{-2}.
We did not select Equation (4.7) over Equation (4.4) and Equation (4.5) for defining the conductivities in order to achieve better agreement with the CV observed in the reference implementation—CV was not a parameter of interest in our purely SAN configuration. Instead, this choice was made to guarantee that the resistance of the elements, as calculated in the stiffness matrix, corresponded to the desired coupling resistance (see Appendix A).
Simulations were conducted using resistances of 10 MΩ, 100 MΩ, 1,000 MΩ and 10,000 MΩ for the coupled configurations, and ∞ MΩ to represent the uncoupled configuration. The set comprising the simulation in the uncoupled configuration and the four simulations in the coupled configurations was considered as a single simulation pack.

4.2.3 Hypocalcaemia and Autonomic Nervous System Compensation

Each simulation pack was tested in the presence of different extracellular calcium concentrations. In particular the baseline condition of $[Ca^{2+}]_o = 1.8$ mM and the three hypocalcaemic concentrations reported in Table 4.1 were tested. Then for each of those, a simulation pack with the amount of ISO that was shown to be able to compensate for hypocalcaemia in single-cell simulations of the baseline extended SDiF model was tested as shown in Table 4.1. Before launching the tissue simulations, the variants were simulated individually for 1,000 s in order to allow them to reach steady state. The values of the state variables were then used to initialise the models in the patch.

4.2.4 Fibroblasts

Given the large amount of fibroblasts found in the SAN tissue [20], we decided to see if it was possible to include them in our experimental setup. Therefore we generated another 40×40 mesh where the elements had a 1% chance of belonging to a fibroblast region. We then assigned the Morgan model [53] to these elements. Due to the way openCARP resolves

Table 4.1: $[Ca^{2+}]_o$ and [ISO] used for the simulations under hypocalcaemia and under the ANS compensation.

Hypocalcaemia		ANS compensation	
$[Ca^{2+}]_o$ (mM)	[ISO] (nM)	$[Ca^{2+}]_o$ (mM)	[ISO] (nM)
1.2	0.0	1.2	28.0
0.8	0.0	0.8	90.0
0.6	0.0	0.6	170.0

the conflicts at the borders between regions [54], this assignment resulted in 8% of the nodes being fibroblasts. The coupling resistance between fibroblasts and SANCs was assumed to be the same as the coupling resistance between SANCs.

4.2.5 Simulation Study

As already outlined in Section 3.2.2 and reiterated in this chapter, openCARP (version 18.1) was employed to conduct all numerical simulations. The parabolic solver was configured to use the monodomain formulation, with the intracellular volume fraction δ_i fixed at 1. The surface-to-volume ratio was chosen to correspond to that of a cylindrical cell with a radius of 4 µm and a height of 70 µm. The time integration was performed using the forward Euler method. Simulations including ISO were advanced in time with a time step of 1 µs, whereas all other simulations used a time step of 5 µs. In both settings, the temporal resolution of the recorded output was 0.5 ms.
All simulations lasted 20 s, but only the last 5 s were used to compute the metrics already defined in Section 2.2.2. In particular, following the work of Campana *et al.* [9], the OSs and the MDPs were identified, then the TOPs were defined as the first point between a MDP and an OS where:

$$\frac{d^2V_m}{dt^2} \geq 0.15 \max \frac{d^2V_m}{dt^2}. \tag{4.8}$$

Lastly, DDs, CLs and APAs were calculated as described in Section 2.2.2.

4.2.6 Classification

In accordance with the methodology described by Campana *et al.* [9] and represented in Figure 4.3, each cell within the patch was classified based on its electrophysiological behaviour in both the uncoupled and coupled conditions. In the uncoupled configuration, cells were categorised as *spontaneous* if they satisfied all of the following criteria:

1. they exhibited at least three APs within the final 5 s of the simulation;
2. the mean V_m at the OSs was greater than 0 mV;
3. the mean V_m at the MDPs was lower than -40 mV.

Cells that did not meet these conditions were classified as *dormant*.

In the coupled state *spontaneous* cells were divided into:

- *driving*, if they provided current to their neighbours at the TOPs;
- *follower*, if they received current from their neighbours at the TOPs;
- *stopped*, if they ceased to show any of the characteristics of *spontaneous* cells.

Instead, when coupled *dormant* cells were deemed:

- *driven*, if they met the criteria for *spontaneous* cells;
- *unexcitable*, if one or more of the criteria was not met.

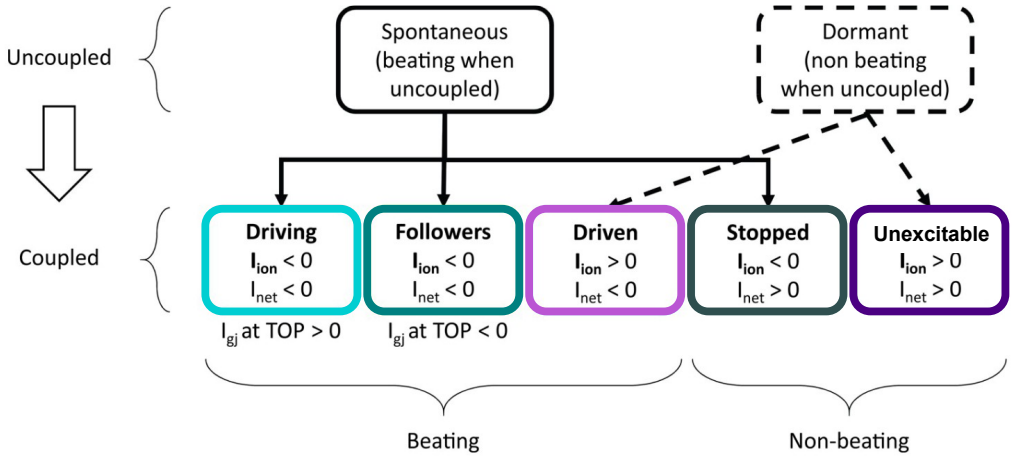

Figure 4.3: Rationale used to classify the variants based on their electrophysiological behaviour. In the uncoupled condition, cells were classified as either *spontaneous*, if they exhibited spontaneous beating activity, or *dormant*, if no beating was observed. Under coupled conditions, *spontaneous* cells were further subdivided into *driving* or *follower* cells, depending on whether they provided or received current from their neighbours, respectively. *Spontaneous* cells that ceased beating upon coupling were classified as *stopped*. Similarly, *dormant* cells were classified as *driven* if they started beating when coupled, or *unexcitable* if they remained non-beating under the same conditions. Figure adapted from [9].

Chapter 5

Results

This chapter will be divided into two sections. Section 5.1 reports on the results obtained when benchmarking the openCARP implementation of the SKNM against the reference implementation of Jæger *et al.* [41]. Moreover, Section 5.2 focuses on the results gathered from tissue simulations on the 40×40 cell patch with different levels of intercellular coupling, $[Ca^{2+}]_o$ and ANS stimulation, to evaluate the compensatory effect of sympathetic stimulation on hypocalcaemia-induced bradycardia, which had already been demonstrated in single-cell simulations.

5.1 Discrete Coupling Verification

To verify the discrete coupling mechanism, the CV was measured for different values of the gap junction resistance R_g in the patch, as described in Section 4.1. Hereby, the CV for the openCARP implementation was computed with both mass lumping enabled and disabled. As shown in Figure 5.1, the reference implementation regularly showed faster conduction compared to the openCARP implementation, irrespective of whether mass lumping was applied.

The relative error between the CVs in the two implementations was calculated for every value of R_g according to:

$$e_{\%}^{R_\mathrm{g}} = 100 \frac{|CV_{reference}^{R_\mathrm{g}} - CV_{openCARP}^{R_\mathrm{g}}|}{CV_{reference}^{R_\mathrm{g}}}. \tag{5.1}$$

The relative error ranged between 18 % to 29 %, spiking for $R_g = 1.5$ MΩ and then converged again to 18 % for higher gap junction resistance as it is shown in Figure 5.2.

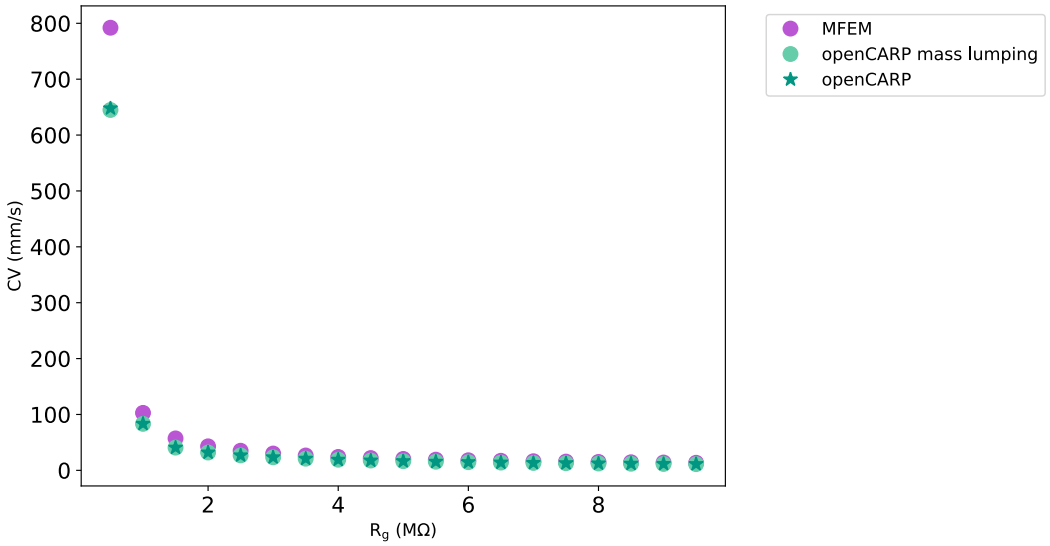

Figure 5.1: CV in the patch for different values of gap junction resistance R_g. Both the reference and the openCARP implementations showed the same trend between CV and R_g, however the reference implementation regularly showed faster conduction compared to the openCARP implementation.

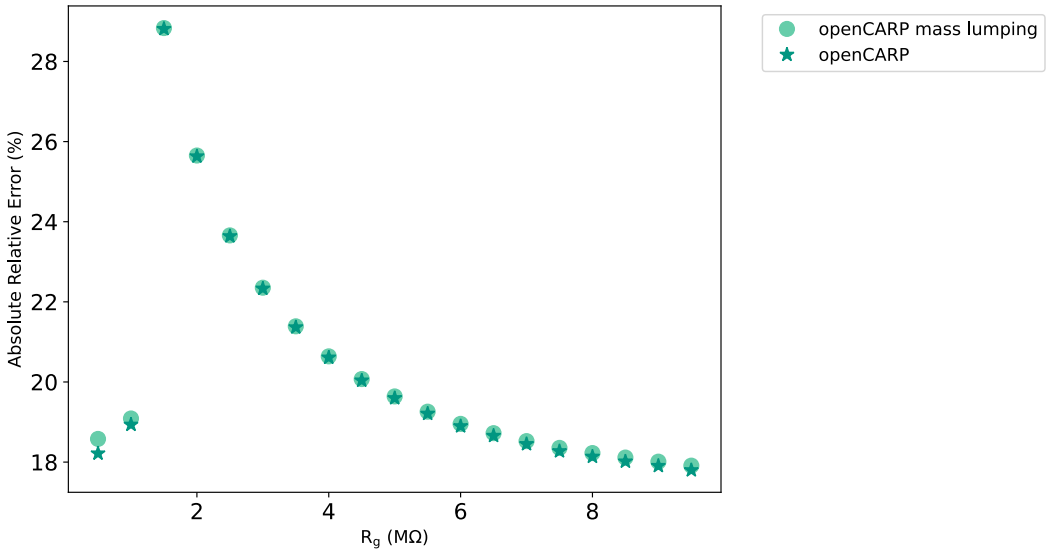

Figure 5.2: Relative error expressed in terms of percentage between the CV in the reference and in the openCARP implementations. Mass lumping does not make a relevant difference.

5.2 Sinoatrial Node Tissue Simulations

In this section, the results regarding the SAN are presented. The section begins with a description of the baseline condition, followed by the findings for the hypocalcaemic

conditions, first in the absence and subsequently in the presence of ANS stimulation to compensate for the hypocalcaemia-induced bradycardia. Finally, a brief subsection is devoted to simulations incorporating fibroblasts dispersed throughout the tissue.

5.2.1 Baseline

Under baseline conditions ($[Ca^{2+}]_o = 1.8\,\text{mM}$, $[ISO] = 0.0\,\text{nM}$), all cells in the patch spontaneously depolarised and were thus classified as *spontaneous* (see Section 4.2.6). Moreover, they exhibited heterogeneous AP characteristics in the uncoupled state that lessened when coupling was introduced as the cells synchronised. Figure 5.3 provides an example of this phenomenon in case of a coupling with R of $1,000\,\text{M}\Omega$. For instance, the CL spanned from 196 ms to 390 ms when the cells were uncoupled but converged to 233 ms with 1,000 MΩ coupling.

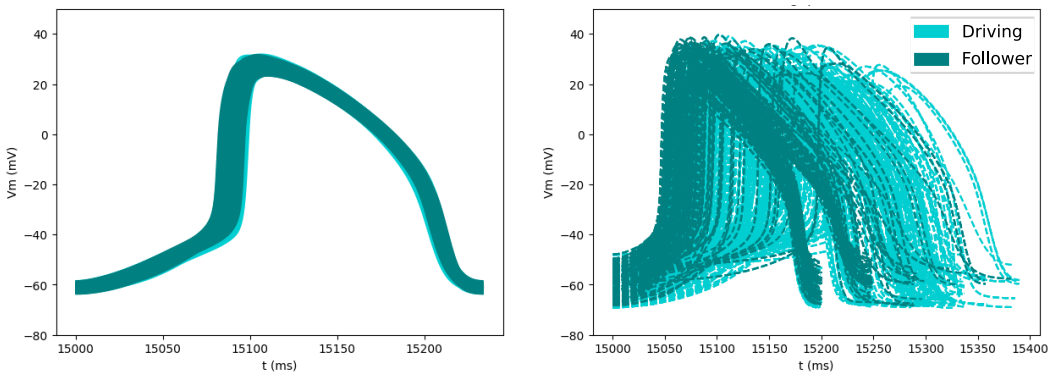

Figure 5.3: APs of the variants in the population under baseline conditions, both in the uncoupled ($R = \infty\,\text{M}\Omega$, right) and in the coupled ($R = 1,000\,\text{M}\Omega$, left) case. When coupling is present, the otherwise diverse APs of individual variants converge to a single shape.

Figure 5.4 shows the distribution of CL, APA and DD in both the uncoupled and 1,000 MΩ coupled case. In particular the CL, converged from 256 ± 50 ms, when uncoupled, to 233 ms when 1,000 MΩ coupling was introduced. Similarly, the mean DD changed from 105 ± 47 ms to 86 ± 3 ms, and the APA from 89 ± 9 mV to 89 ± 2 mV.

As already mentioned, all the variants were *spontaneous* under baseline conditions, but the different levels of coupling determined a variation in the proportion of *driving* and *follower* cells in the patch. As the intercellular coupling resistance R increased, so did the amount of *driving* cells, which went from 56.0 % in the 10 MΩ case to 87.6 % in the 10,000 MΩ case (Figure 5.6). Similar results can be observed in the maps shown in Figure 5.5, in which it is clearly visible how the amount of driving cells increased with R.

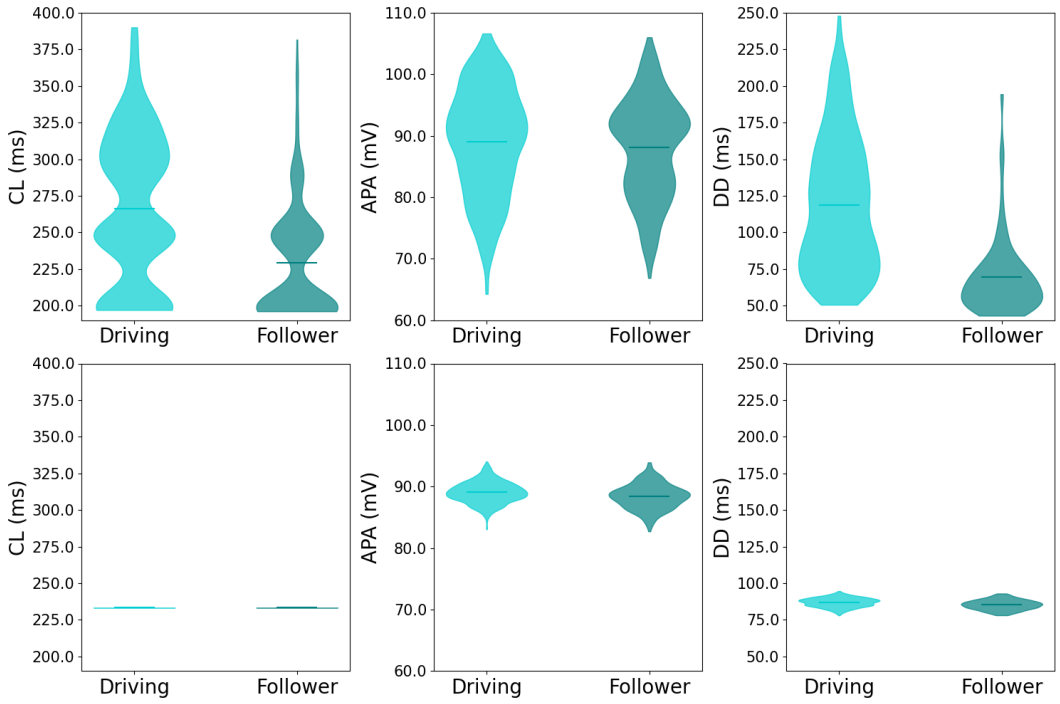

Figure 5.4: Violin plots of the distribution of CL, APA and DD for the uncoupled (top) and the coupled (bottom) case. When coupling was present the spread in the distribution of these metrics decreased as a result of the entrainment in the tissue.

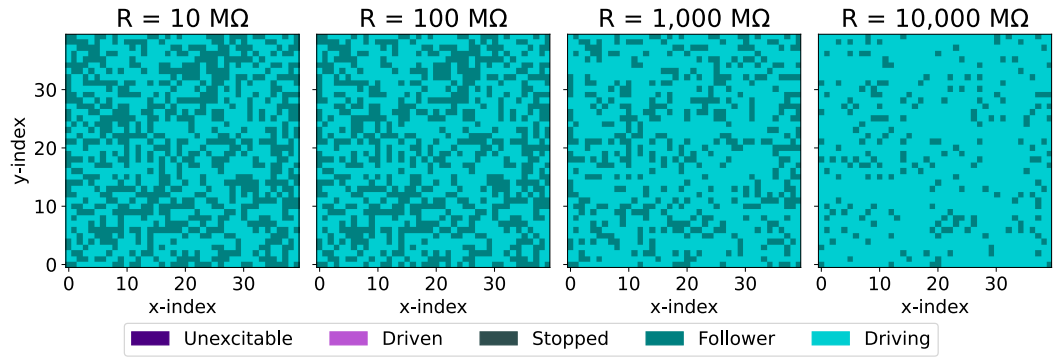

Figure 5.5: Spatial distribution of the different cell categories for the different R values. Under baseline conditions all the cells are either *driving* or *follower*, but as R increases, so does the number of driving cells.

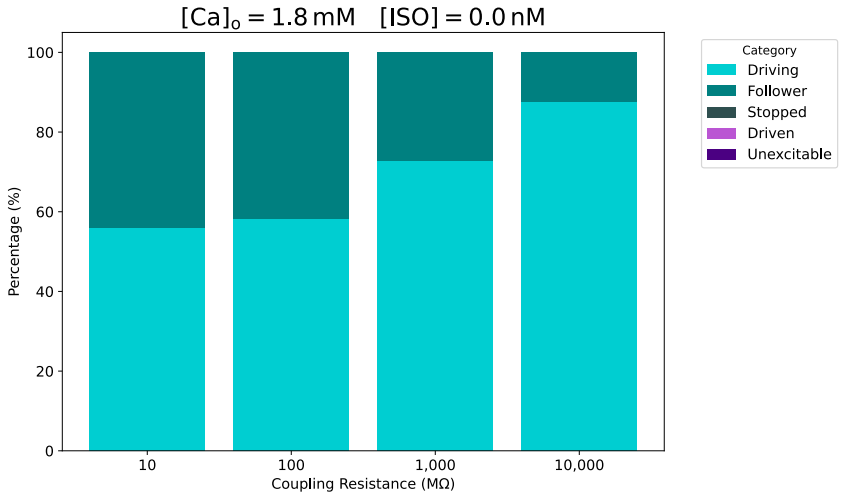

Figure 5.6: Proportion of cells belonging to each category for the values of R tested. Under baseline conditions all the cells in the patch were *spontaneous* and were thus categorised as *driving* or *follower* when coupled. As R increased, so did the quantity of driving cells.

5.2.2 Hypocalcaemia

After performing simulations under baseline conditions, the patch was tested under the different hypocalcaemic conditions, namely 1.2, 0.8 and 0.6 mM $[Ca^{2+}]_o$ (Table 4.1). Before assessing the results of the tissue simulations, it is important to acknowledge that, in single-cell simulations under these conditions, the extended SDiF suffered evident prolongation of the CL as $[Ca^{2+}]_o$ decreased. Indeed, it increased from 330 ms at $[Ca^{2+}]_o = 1.8$ mM to 387 ms at $[Ca^{2+}]_o = 1.2$ mM, and to 520 ms at $[Ca^{2+}]_o = 0.8$ mM, until the model became silent at $[Ca^{2+}]_o = 0.6$ mM.

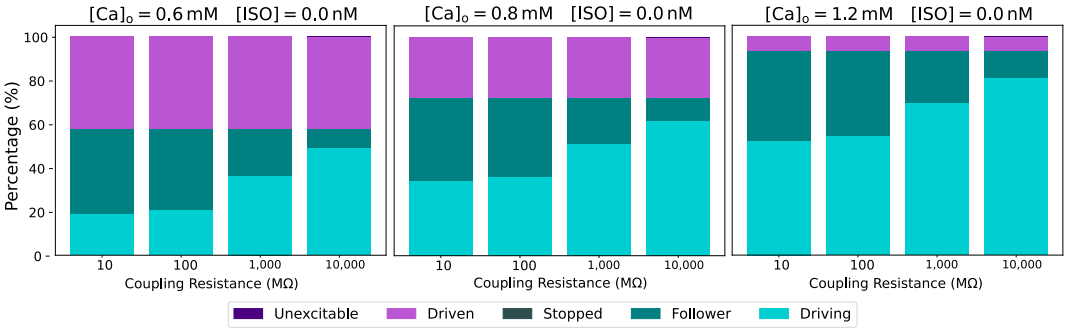

Figure 5.7: Proportion of cells belonging to each category from the simulation packs with hypocalcaemia. As $[Ca^{2+}]_o$ decreased (from top to bottom), so did the percentage of *spontaneous* cells. In spite of this, at any $[Ca^{2+}]_o$ all the dormant cells became driven once coupling was introduced, with the exception of just a few cells when $R = 10,000$ MΩ.

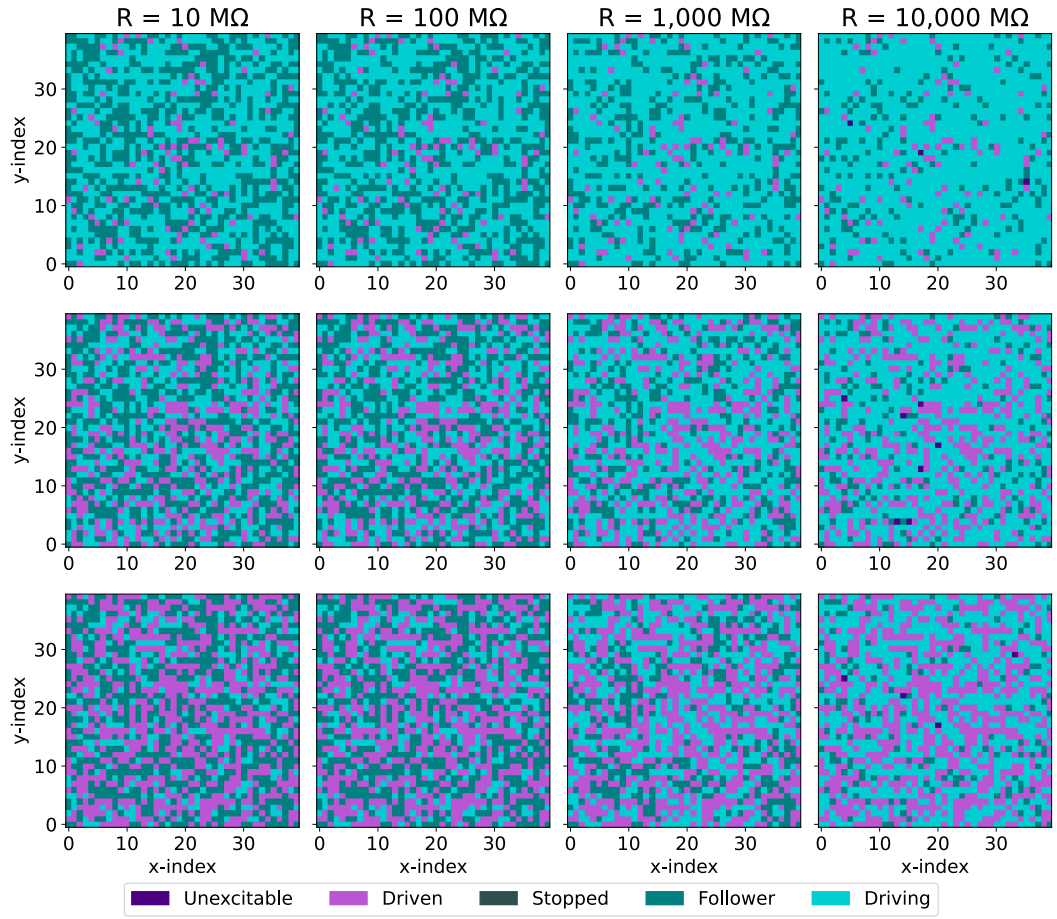

Figure 5.8: Spatial distribution of the different cell categories from the simulation packs with hypocalcaemia. It is evident that the quantity of *unexcitable* cells increased as extracellular calcium decreased from top ($[Ca^{2+}]_o = 1.2$ mM) to bottom $[Ca^{2+}]_o = 0.6$ mM. Nevertheless, almost all of them are driven. Only for $R = 10{,}000\,\text{M}\Omega$ some cells became *unexcitable*.

Regardless of the hypocalcaemic condition tested, all cells in the POM were either *spontaneous* or got *driven* by neighbouring ones (Figure 5.7), with only a few cells being *unexcitable* when R was 10,000 MΩ (3 at $[Ca^{2+}]_o = 1.2$ mM, 7 at $[Ca^{2+}]_o = 0.8$ mM and 4 at $[Ca^{2+}]_o = 0.6$ mM), as can be appreciated in the maps of Figure 5.8. Conversely, the quantity of *spontaneous* cells was dependent on $[Ca^{2+}]_o$, with 92.4 % of the cells still spontaneously depolarising at 1.2 mM, 72.4 % at 0.8 mM and 57.7 % at 0.6 mM. The same trend in the proportion of *driving* and *follower* cells already observed under baseline conditions was present in all hypocalcaemic simulations. Indeed the amount of *driving* cells increased with R (Figure 5.7).

At any $[Ca^{2+}]_o$, cells synchronised when coupling was present, albeit showing greater variability for the highest values of R. For example, in the most severe condition ($[Ca^{2+}]_o = 0.6$ nM), the CL decreased from 321.88 ± 122.34 ms when uncoupled, to 282.58 ± 0.07 ms

with $R = 1,000\,\text{M}\Omega$, and to $275.50 \pm 1.78\,\text{ms}$ with $R = 10,000\,\text{M}\Omega$. At the same time the CL increased as the $[Ca^{2+}]_o$ decreased as shown in Figure 5.9.

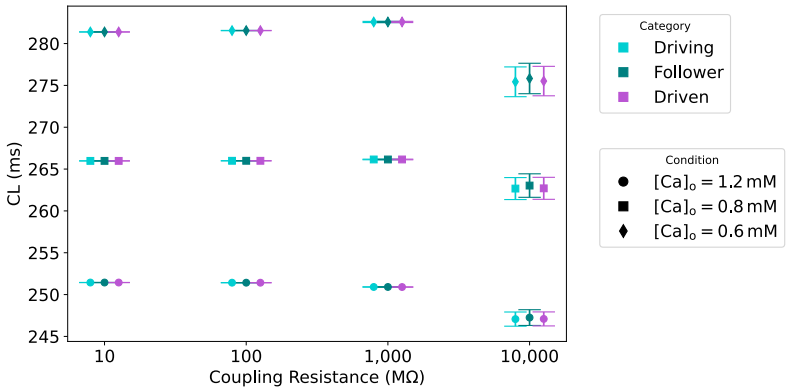

Figure 5.9: CL of the different cell categories when coupling was present. The CL increased as $[Ca^{2+}]_o$ decreased, and stayed mostly constant for all values of R at any given $[Ca^{2+}]_o$.

5.2.3 Autonomic Nervous System Compensation

In order to asses whether ANS regulation was able to prevent bradycardia caused by hypocalcaemia, as previously shown in single-cell simulations of the baseline extended SDiF model [8], sympathetic activation was simulated using various doses of ISO. Thus, ISO was administered at the concentration required to maintain a constant CL in the baseline extended SDiF model under the different hypocalcaemic conditions (see Section 4.2.3). In the corresponding single-cell simulations, this resulted in exponentially increasing [ISO] with decreasing $[Ca^{2+}]_o$, while CL remained fixed at 319 ms.

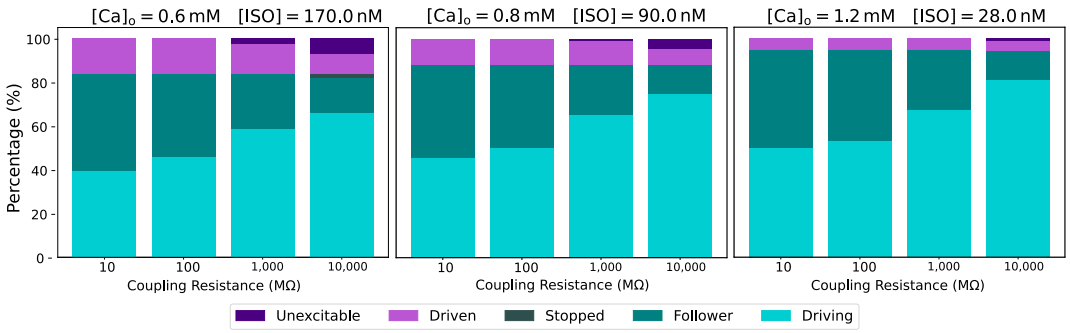

Figure 5.10: Proportion of cells belonging to each category from the simulation packs with ANS compensation. Compared to Figure 5.7, the compensation increased the quantity of *spontaneous* cells at any $[Ca^{2+}]_o$. At the same time the amount of *unexcitable* cells grew for the highest values of R. Together with these, some stopped cells appeared for $R = 10,000\,\text{M}\Omega$.

Figure 5.10 illustrates that the percentage of *spontaneous* cells increased when ISO was introduced compared to the simulation packs were ISO was absent. Namely, at $[Ca^{2+}]_o = 1.2$ mM, 94.6 % of the cells were *spontaneous* with $[ISO] = 28.0$ nM compared to 92.4 % with $[ISO] = 0.0$ nM, at $[Ca^{2+}]_o = 0.8$ mM, 88.2 % remained *spontaneous* with $[ISO] = 90.0$ nM against 72.4 % with no ISO, and at $[Ca^{2+}]_o = 0.6$ mM 83.7 % continued to show automaticity with $[ISO] = 170.0$ nM compared to only 57.7 % without ISO.
At the same time, the amount of *unexcitable* cells unexpectedly grew for the 1,000 MΩ and the 10,000 MΩ cases for the $[Ca^{2+}]_o = 0.8$ mM $[ISO] = 90.0$ nM and the $[Ca^{2+}]_o = 0.6$ mM $[ISO] = 170.0$ nM simulation packs (see Table 5.1), reaching 0.8 % and 4.4 % for the former, and 2.6 % and 7.2 % for the latter. Instead, the number of *unexcitable* cells only increased for the 10,000 MΩ case for the $[Ca^{2+}]_o = 1.2$ mM $[ISO] = 28.0$ nM simulation pack, where it rose to 1.25 %. This becomes apparent by comparing side by side the maps of Figure 5.8 and Figure 5.11.

Table 5.1: Percentage of *unexcitable* cells under different conditions. The administration of ISO increases the portion of *unexcitable* cells in all cases except for the 1,000 MΩ $[Ca^{2+}]_o = 1.2$ mM one.

Condition		% of unexcitable cells	
$[Ca^{2+}]_o$ (mM)	[ISO] (nM)	1,000 MΩ	10,000 MΩ
1.2	0.0	0.00	0.19
	28.0	0.00	1.25
0.8	0.0	0.00	0.44
	90.0	0.81	4.44
0.6	0.0	0.0	0.25
	170.0	2.62	7.19

Furthermore, for $R = 10,000$ MΩ some stopped cells were present: 0.4 % at $[Ca^{2+}]_o = 0.8$ mM $[ISO] = 90.0$ nM and 1.6 % at $[Ca^{2+}]_o = 0.6$ mM $[ISO] = 170.0$ nM.

The introduction of ISO led to a sharp reduction of the CL compared to the simulation packs were the ANS compensation was not active. For example, considering the 1,000 MΩ case, the introduction of 170.0 mM of ISO at $[Ca^{2+}]_o = 0.6$ mM reduced the mean CL from 282.58 ± 0.07 ms to 210.38 ± 0.12 ms. Similarly, at $[Ca^{2+}]_o = 0.8$ mM the mean CL was decreased from 266.15 ± 0.04 ms ($[ISO] = 0.0$ nM) to 215.74 ± 0.11 ms ($[ISO] = 90.0$ nM), and at $[Ca^{2+}]_o = 1.2$ mM it was shortned from 250.91 ± 0.11 ms ($[ISO] = 0.0$ nM) to 222.19 ± 0.04 ms ($[ISO] = 28.0$ nM).
It is also worth to mention that, contrary to the results in Section 5.2.2, in the presence of $[ISO]$, the CL increased with the $[Ca^{2+}]_o$, albeit the variation was much less pronounced (Figure 5.12).

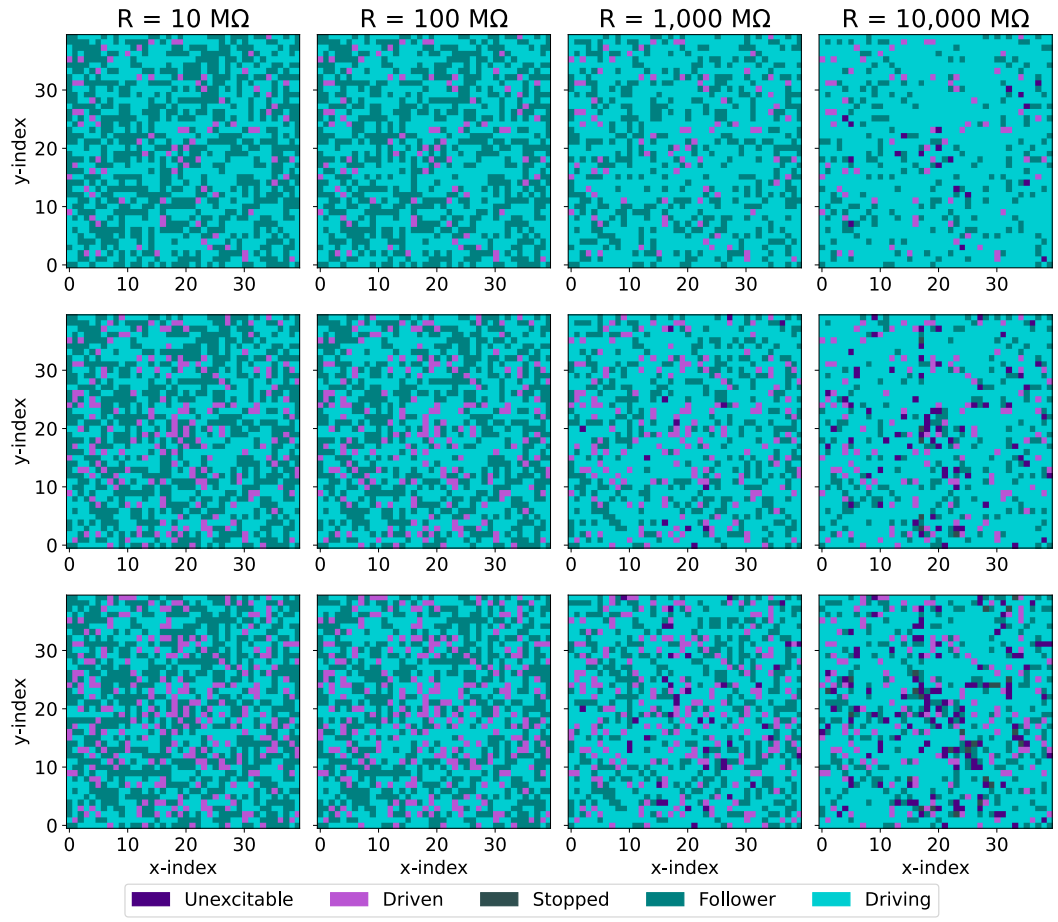

Figure 5.11: Spatial distribution of the different cell categories from the simulation packs with ANS compensation. By comparing these results to Figure 5.8, the generalised increase in the amount of *spontaneous* cells and the growth of the number of *unexcitable* and stopped cells for the highest values of R are clearly visible.

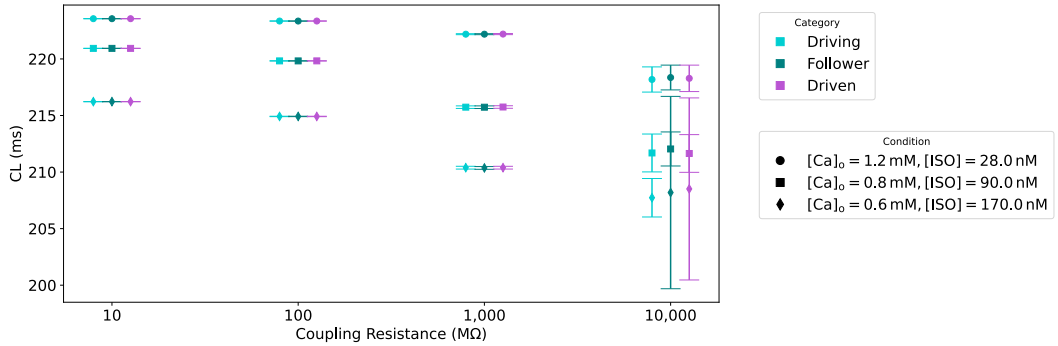

Figure 5.12: CL of the different cell categories when coupling was present. With $[ISO]$, the CL was reduced compared to the simulation packs without $[ISO]$ of Figure 5.9.

5.2.4 Fibroblasts

The introduction of fibroblasts did not cause significant changes in the metrics measured (see Appendix B), with the only exception being the percentage of stopped cells in the $[Ca^{2+}]_o = 0.6\,\text{mM}$, $[ISO] = 170.0\,\text{nM}$, $R = 10,000\,\text{M}\Omega$ case, which increased to 2.1 % compared to 1.6 % without fibroblasts.

Chapter 6

Discussion

6.1 Discrete Coupling in openCARP

The SKNM presented by Jæger *et al.* [41] and described in Section 3.2.1 constituted the foundation that enabled the realisation of this work. Despite openCARP not having a native implementation of this method, we were able to retain the cellular resolution and the control over the individual conductances connecting cells by performing monodomain simulations on a mesh constituted exclusively by line elements (see Section 4.1).
The results of the verification presented in Section 5.1 showed a low degree of agreement between the CVs of the reference and openCARP implementations, with the relative error ranging between 18 % and 28 % depending on the gap junction resistance R_g tested. Furthermore, other studies using the SKNM for SAN tissue simulations (such as [9, 12]) did not distinguish between the contributions of cytoplasm, extracellular milieu, and R_g in the determination of the intercellular coupling resistance R.
Consequently, we used Equation (4.7), instead of Equation (4.5) and Equation (4.4), to determine the conductivity assigned to the elements of the SAN tissue simulations. Despite loosing some control over the physiological factors determining R, this ensured that the resistance of the elements, as calculated in the stiffness matrix (see Section 3.2.2), coincided with the desired R.

6.2 Sinoatrial Node Tissue Simulations

6.2.1 Baseline

Under baseline conditions, all cells in the patch were already *spontaneous* (see Section 4.2.6 for the classification into different categories) when uncoupled. However, when coupling was present, clear signs of the entrainment mechanism described in Section 2.2.2.2 appeared.

Indeed, the otherwise diverse APs of the SANCs in the POM converged to a common AP shape as a result of synchronisation. Furthermore, as already observed by Michaels *et al.* [28], entrainment proved to be a democratic process, with cells not synchronising to the CL of the fastest cell (196.11 ms), but to an intermediate value that was dependent on R. For example for $R = 1,000\,\text{M}\Omega$ the mean CL was 233 ± 0 ms, which was still 23 ms faster than the mean CL of the POM (256 ± 51 ms), and almost 100 ms shorter than the CL of the standard extended SDiF model (330 ms).

6.2.2 Hypocalcaemia

As introduced in Section 4.2.3 and in Section 5.2.2, the patch was tested in three different reduced $[Ca^{2+}]_o$ conditions. At $[Ca^{2+}]_o = 0.6$ mM, a level of hypocalcaemia not compatible with the spontaneous activity of the baseline extended SDiF model, 57.7 % of the variants in the POM could still be classified as *spontaneous*, and were able to drive the rest of the cells in the tissue for any R value tested. Simulating higher $[Ca^{2+}]_o$ increased the percentage of *spontaneous cells* compared to the 0.6 mM case, and as expected these cells were able to drive the dormant ones.

At any $[Ca^{2+}]_o$ tested, the entrainment phenomenon was observed, with cells synchronising to a common CL regardless of R. However, as R increased, so did the variability in the measured metrics. Thus, with due diligence, these results, obtained by lowering $[Ca^{2+}]_o$, can be compared to those gathered by Campana *et al.* [9] when I_{CaL} was blocked. They observed that with a 50 % blockade, less than 40 % of the cells remained *spontaneous*, but these were still able to drive the rest of the tissue at intermediate coupling values. Instead, we saw almost 60 % of *spontaneous* cells, which were able to drive the tissue regardless of the coupling. These differences can be ascribed to several factors, such as the different way in which Ca^{2+} was inhibited, the methods used to generate the POMs, and the spatial distribution of the variants in the tissue.

The comparison to the findings of Campana *et al.* [9] can also be extended to the CLs. In both cases, the mean CL in the tissue increased as Ca^{2+} was reduced (in our case by lowering $[Ca^{2+}]_o$ and in their case by blocking I_{CaL}). In the most severe case (50 % I_{CaL} blockade), they also noticed a reduction in the CL as micro-reentries were present, which was something we did not observe. It is important to acknowledge that they reported this CL results for a POM generated starting from the Fabbri model [55]. Therefore, together with the other factors that were already mentioned, interspecies differences also play a role in determining this discrepancy. Indeed, the bradycardic effects of reduced $[Ca^{2+}]_o$ are known to be much more pronounced in human models (as the Fabbri model) compared to models of small mammals (as the SDiF model) [56].

6.2.3 Autonomic Nervous System Compensation

The administration of ISO had two major expected effects (see Section 5.2.3):

1. It increased the quantity of *spontaneous* cells at any $[Ca^{2+}]_o$ compared to the corresponding simulation packs without ISO.
2. It shortened the mean CL in the tissue, bringing it to values comparable to the baseline simulations, regardless of the coupling value and $[Ca^{2+}]_o$.

Although these results point to a compensatory role of ANS stimulation in hypocalcaemia-induced bradycardia, at the same time, ISO unexpectedly increased the amount of *unexcitable* cells. This last finding must be contextualised: Cells were classified as *unexcitable* when they failed to meet the criteria of Section 4.2.6 both in the uncoupled and in the coupled state, and this did not necessarily mean a complete lack of activity (see Figure 6.1).
Nevertheless, most of these cells were classified as *driven* in the corresponding simulations under hypocalcaemia without ISO. This indicates that in some variants the sympathetic stimulation altered the cell properties, causing them to fail to meet the aforementioned criteria. This could mean, for instance, that already elevated depolarisation currents in one variant increased further due to an increased $[ISO]$, leading to an imbalance that repolarising currents were then unable to compensate for. This becomes clearer by comparing Figure 6.1 with Figure 6.2, where the APA is visibly larger.

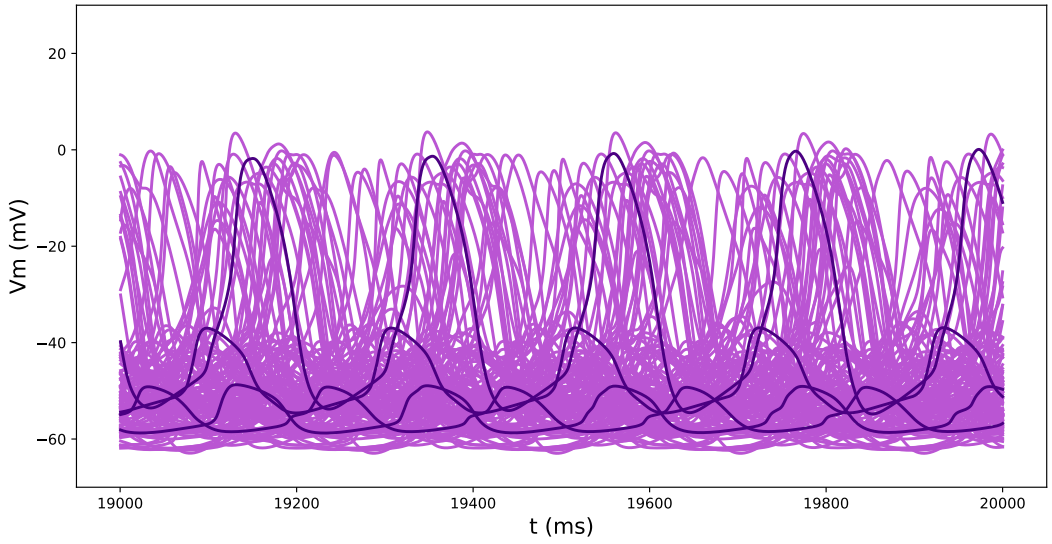

Figure 6.1: AP traces from the last second of simulation of cells that were classified as *unexcitable* in the $[Ca^{2+}]_o = 0.6\,\text{mM}$ $[ISO] = 170.0\,\text{nM}$ $R = 10,000.0\,\text{M}\Omega$. In purple, four representative traces are highlighted, whereas the other cell variants are shown in fuchsia. It can be appreciated that *unexcitable* cells did not necessarily lack spontaneous activity, but simply failed to meet the criteria presented in Section 4.2.6. For example the entirety of the cells fail to have the mean $OS \geq 0\,\text{mV}$.

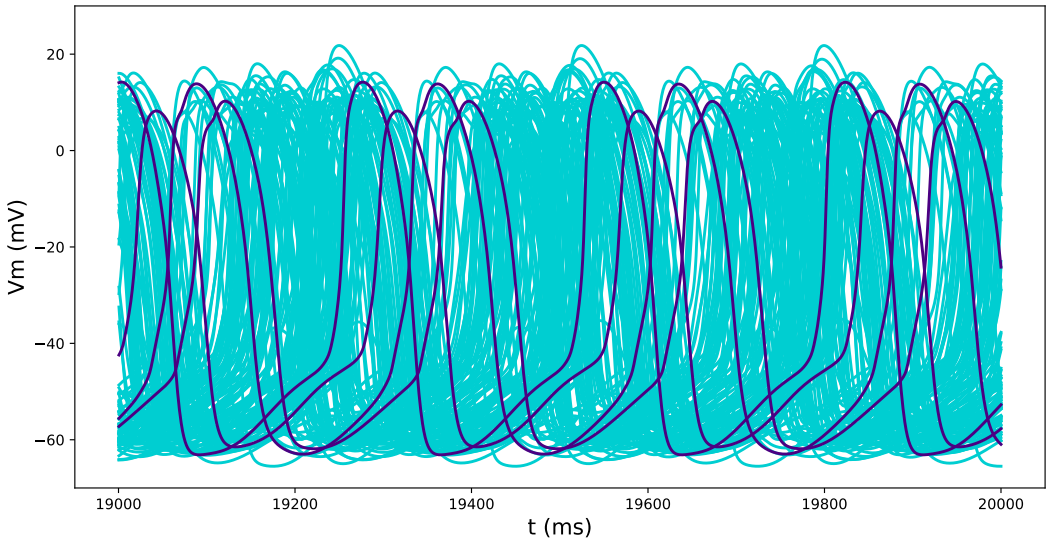

Figure 6.2: Corresponding AP traces to those presented in Figure 6.1 but at $[ISO] = 0.0\,\text{nM}$. In the absence of ISO, the CL increased and so did the APA. Therefore most of the cells are classified as driven.

6.2.4 Heterogeneity

While single-cell simulations were able to reproduce the sinus bradycardia followed by asystole observed in HD patients upon withdrawal of the sympathetic stimulation [4, 6, 8], our tissue simulations could not. Indeed, the heterogeneity of the population, together with the coupling in the tissue, were able to prevent sinus arrest, or even severe prolongation of the CL, as the *spontaneous* cells could always drive those that did not show spontaneous activity when uncoupled.

Arguably, the astonishing resilience of the patch to hypocalcaemia may be due to shortcomings of our setup. First of all, the POM was calibrated using experimental data that expanded the pool of experiments used to fit the SDiF model with more recent data. Most samples were obtained from the works of Vinogradova *et al.* [57] and Bucchi *et al.* [58] . This could mean that the differences in the APs of the variants reflect both intra-individual and inter-individual variability. Therefore we cannot rule out the possibility that POMs calibrated on tailored data would not have shown the same resilience. Secondly, if the scaling of the conductances of the model used to generate the variants was to be considered as a representation of the expression of channel proteins, then the random assignment of the variants in the patch becomes a bold assumption. Indeed, this setup allows one cell to have 16 times the amount of channels for a given current compared to its neighbour, which is not realistic for SANCs, which are known to form clusters with similar properties in the SAN.
Having acknowledged these limitations, the present work suggests that the asystole observed in HD patients under hypocalcaemia may not arise from a lack of spontaneous activity in

the SAN, but instead to its inability to successfully pace and drive the atria, which could be motivated by the reduction in APA observed with ISO and discussed in the previous section.

6.2.5 Fibroblasts

Even though investigating the role of fibroblasts was outside the scope of the research question, given the large amount present in the SAN tissue, we decided to perform a set of simulations that included them as discussed in section Section 4.2.4.
As mentioned in Section 5.2.4, the introduction of fibroblasts in the patch did not bring meaningful differences to metrics measured, nor to the percentage of SANCs that was classified in each category under the different conditions. The only exception being the increase of the quantity of *unexcitable* SANCs from 1.6 % to 2.1 % when fibroblasts were present (at $[Ca^{2+}]_o = 0.6\,\text{mM}$, $[ISO] = 170.0\,\text{nM}$, $R = 10,000\,\text{M}\Omega$).

This finding should not be interpreted as definitive evidence that fibroblast do not play a significant role in the electrophysiology of the SAN. On the contrary, it highlights the limitations of our "proof of concept" integration of fibroblasts in the patch.
As a matter of fact, using the quick and easy to implement region tagging functionality of openCARP meant that we had little control over the quantity of fibroblasts that actually ended up in the tissue. This prevented us from thoroughly testing the effects that different quantities of fibroblasts could have had. It also did not allow us to investigate what would have happened if the connections among fibroblasts were different to those between fibroblasts and SANCs, and from those between SANCs and SANCs as they are *in vivo* [59] .

Chapter 7

Outlook

In this work, we implemented a novel method to retain the cellular resolution achieved by the SKNM while using openCARP monodomain solver. This allowed a streamlined integration of existing ionic models in our setup.
As our approach was not mathematically equivalent to the SKNM, and scaling factors were introduced (see Appendix A), these modifications should be carefully considered when intending to exploit this implementation of the SKNM in openCARP. This is especially relevant for anisotropic meshes, where the scaling factors would vary within the tissue.

SAN tissue simulations provided great insights into the interplay of coupling, heterogeneity, and ANS stimulation in the determination of the BR under different $[Ca^{2+}]_o$. Still, some of the assumptions used in the generation of the POM and in the assignment of the variants to the nodes of mesh distanced our simulations from the physiology of the SAN. Namely, the POM was calibrated against a large pool of experimental data, and the random assignment of variants opened the possibility for neighbouring cells to have completely different electrophysiological properties.
Hence, the role that these factors had in the determination of the resilience of the patch to hypocalcaemia needs to be further investigated. Using different, more restricted, POMs may shed light on the mechanisms underlying SCD, which is observed only in a portion of HD patients. Moreover, assigning cell properties based on gradients in the tissue would better represent SAN physiology.
In contrast to single-cell simulations, we were not able to reproduce the sinus bradycardia followed by asystole observed in HD patients, suggesting that it may also arise from a loss of atrial driving rather than a lack of spontaneous activity in the SAN.
While the aforementioned limitations may be the cause of this discrepancy, the effects that hypocalcaemia and ANS stimulation have on pace-and-drive could be further evaluated by coupling the current SAN model to a portion of the RA, as implemented by Ricci *et al.* [12].

The introduction of fibroblasts via region tagging (see Section 4.2.4) enabled us to partially recapitulate the structural and functional characteristics observed in histological sections of the SAN [20], by exploiting a well-integrated functionality of the openCARP framework.

However, this approach limited our ability to fine-tune the concentration and the coupling of fibroblasts in the tissue.
Lastly, the inconclusive results arising from this implementation require a more thorough investigation of the role of fibroblasts in SAN electrophysiology. Such work necessarily needs to start from a node-wise integration of fibroblasts in the tissue, as this would overcome these limitations.

Chapter 8

Conclusion

In this work, we developed a strategy to retain the advantages of the SKNM within openCARP by performing monodomain simulations on meshes composed exclusively of one-dimensional line elements. This implementation preserved node-wise control of cellular properties and enabled direct manipulation of intercellular coupling through element conductivities. Since the verification study revealed quantitative discrepancies in conduction velocity compared to the reference implementation, we adopted a different formulation for the conductivities of elements which was more in line with the work of Ricci *et al.* [12] and Campana *et al.* [9]. This ensured that the resistance embedded in the stiffness matrix corresponded to the desired coupling resistance, allowing for a controlled investigation of tissue-level interactions.

This framework enabled the integration of a calibrated POM of the extended SDiF model into a two-dimensional SAN tissue patch. By assigning heterogeneous variants to individual nodes, we reproduced electrophysiological variability while preserving electrical coupling between cells.
In single-cell simulations, hypocalcaemia reduced automaticity and, in severe cases, abolished spontaneous activity. However, in tissue simulations, coupling and heterogeneity fundamentally altered this behaviour. Even at the lowest $[Ca^{2+}]_o$ tested (0.6 mM), a substantial fraction of variants remained *spontaneous* and were able to entrain and drive the remainder of the tissue across all coupling resistances considered. Consequently, sinus arrest was not observed in the tissue model and the mean CL never exceeded that of the baseline single-cell model.
Administration of ISO shortened CL and increased the proportion of *spontaneous* cells, confirming its expected positive chronotropic effect. However, unlike in single-cell simulations, ISO was not required to preserve global *spontaneous* activity in the tissue. Interestingly, the $[ISO]$ that compensated for hypocalcaemia at the single-cell level appeared to overcompensate in tissue, suggesting that lower levels of sympathetic stimulation may be sufficient when intercellular coupling and heterogeneity are present.
Together, these findings indicate that the deleterious electrophysiological effects of hypocalcaemia observed in single-cell simulations are buffered at tissue level. The resilience

observed in the heterogeneous coupled patch could suggest that sinus bradycardia and asystole reported in HD patients may not arise from a complete loss of excitability within the SAN itself, but rather from an impaired ability of the SAN to effectively pace and drive the atrial myocardium under hypocalcaemic conditions.
Overall, this study highlights the critical role of cellular heterogeneity and electrical coupling in SAN electrophysiology and underscores the importance of tissue-level modelling when interpreting mechanisms inferred from single-cell simulations.

Appendix A

(Non) Equivalence of Simplified Kirchhoff Network Model and OpenCARP Implementation

In this appendix, we provide an example that shows what actually happens when using openCARP's FEM solver on a mesh composed exclusively of line elements. Later, the system matrix will be compared with the SKNM on the same mesh. The minimal case comparable to our setup is an isotropic mesh of 3×3 nodes.

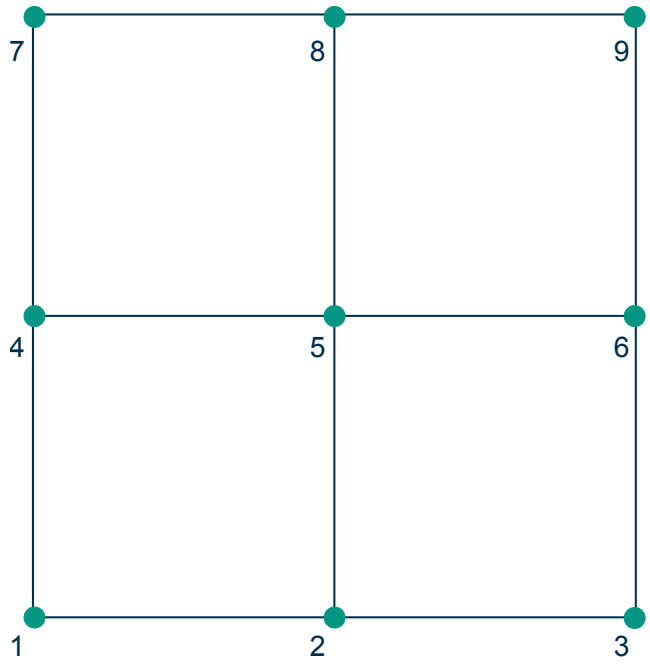

Figure A.1: Example 3×3 mesh with nodes connected exclusively by line elements

A.1 Finite Element Method Solution

The interpolation of the solution on the elements is performed by summation of the shape functions. In particular, since each element connects two nodes, two linear shape functions can be defined on each element so that their sum is 1 at the nodes. If the element connects the nodes with the coordinates $(x_1,0)$ and $(x_2,0)$, the shape functions will be:

$$\phi_1^x = -\frac{x-x_2}{x_2-x_1}, \tag{A.1}$$

$$\phi_2^x = \frac{x-x_1}{x_2-x_1}, \tag{A.2}$$

and can be summarised in the shape function vector:

$$\phi = \begin{bmatrix} \phi_1 \\ \phi_2 \end{bmatrix}. \tag{A.3}$$

We can map the shape functions to a reference element extending from $(-1,0)$ to $(1,0)$ using the transformation $T : \xi \to x$:

$$T(\xi) = \frac{1-\xi}{2}x_1 + \frac{1+\xi}{2}x_2. \tag{A.4}$$

The Jacobian of T is:

$$\frac{dx(\xi)}{d\xi} = -\frac{x_1}{2} + \frac{x_2}{2} = \frac{l}{2}. \tag{A.5}$$

The transformation can be used to define the shape functions on the reference element as follows:

$$\phi_1^\xi = \frac{1}{2}(1-\xi), \tag{A.6}$$

$$\phi_2^\xi = \frac{1}{2}(1+\xi). \tag{A.7}$$

Therefore we can define the shape function vector for the reference element as:

$$\phi^\xi = \begin{bmatrix} \phi_1^\xi \\ \phi_2^\xi \end{bmatrix}, \tag{A.8}$$

from where it follows that:

$$\frac{d\phi^\xi}{d\xi} = \begin{bmatrix} \frac{d\phi_1^\xi}{d\xi} \\ \frac{d\phi_2^\xi}{d\xi} \end{bmatrix} = \begin{bmatrix} -\frac{1}{2} \\ \frac{1}{2} \end{bmatrix}. \tag{A.9}$$

A.1.1 Stiffness Matrix

The stiffness matrix K represents the diffusive properties of the domain. For a single line element e with length l and constant conductivity σ aligned with a grid axis, the local entries are calculated as:

$$k_{ij}^e = \int_{\Omega_e} \sigma \frac{d\phi_i}{dx} \frac{d\phi_j}{dx} dx \tag{A.10}$$

By applying the transformation to the reference coordinate $\xi \in [-1,1]$, the spatial derivative is expressed as $\frac{d\phi}{dx} = \frac{d\phi}{d\xi}\frac{d\xi}{dx}$. Using the inverse of the Jacobian, $\frac{d\xi}{dx} = \frac{2}{l}$, the integral becomes:

$$k_{ij}^e = \int_{-1}^{1} \sigma \left(\frac{d\phi_i^\xi}{d\xi}\frac{2}{l}\right)\left(\frac{d\phi_j^\xi}{d\xi}\frac{2}{l}\right)\frac{l}{2} d\xi \tag{A.11}$$

Factoring out the constants yields:

$$k_{ij}^e = \frac{2\sigma}{l}\int_{-1}^{1} \frac{d\phi_i^\xi}{d\xi}\frac{d\phi_j^\xi}{d\xi} d\xi \tag{A.12}$$

Evaluating this for the linear shape functions $\phi_1^\xi = \frac{1}{2}(1-\xi)$ and $\phi_2^\xi = \frac{1}{2}(1+\xi)$, whose derivatives with respect to ξ are $-1/2$ and $1/2$ respectively, the product of the derivatives is $\pm 1/4$. Integrating over $\xi \in [-1,1]$ results in the local stiffness matrix:

$$k^e = \frac{\sigma}{l}\begin{bmatrix} 1 & -1 \\ -1 & 1 \end{bmatrix} \tag{A.13}$$

Let $G = \sigma/l$. We can have G be exclusively dependent on the intercellular coupling resistance R by setting $\sigma = l/R$. In this way $G = 1/R$.
The global stiffness matrix $K \in \mathbb{R}^{9\times 9}$ is a symmetric, sparse matrix. The diagonal entry K_{ii} is the sum of all G values from elements connected to node i. The off-diagonal K_{ij} is $-G$ if nodes i and j are connected, and 0 otherwise.

$$K = G\begin{bmatrix} 2 & -1 & 0 & -1 & 0 & 0 & 0 & 0 & 0 \\ -1 & 3 & -1 & 0 & -1 & 0 & 0 & 0 & 0 \\ 0 & -1 & 2 & 0 & 0 & -1 & 0 & 0 & 0 \\ -1 & 0 & 0 & 3 & -1 & 0 & -1 & 0 & 0 \\ 0 & -1 & 0 & -1 & 4 & -1 & 0 & -1 & 0 \\ 0 & 0 & -1 & 0 & -1 & 3 & 0 & 0 & -1 \\ 0 & 0 & 0 & -1 & 0 & 0 & 2 & -1 & 0 \\ 0 & 0 & 0 & 0 & -1 & 0 & -1 & 3 & -1 \\ 0 & 0 & 0 & 0 & 0 & -1 & 0 & -1 & 2 \end{bmatrix} \tag{A.14}$$

The centre node has a diagonal of $4G$, while corners have $2G$, and edges have $3G$.

A.1.2 Mass Matrix

The mass matrix M accounts for the temporal evolution and capacitive scaling of the system. The consistent local mass matrix is defined as the integral of the product of the shape functions:

$$m_{ij}^e = \int_{x_1}^{x_2} \phi_i \phi_j dx = \int_{-1}^{1} \phi_i^\xi \phi_j^\xi \frac{l}{2} d\xi \tag{A.15}$$

Evaluating the integral for the combinations of ϕ_1^ξ and ϕ_2^ξ yields:

$$m^e = \frac{l}{6} \begin{bmatrix} 2 & 1 \\ 1 & 2 \end{bmatrix} \tag{A.16}$$

To improve computational efficiency and avoid non-physical oscillations, openCARP defaults to *mass lumping*. This procedure sums the row entries onto the diagonal, effectively approximating the continuous distribution of capacity as discrete "tributary" volumes at the nodes. The lumped local mass matrix is:

$$m_{lumped}^e = \frac{l}{2} \begin{bmatrix} 1 & 0 \\ 0 & 1 \end{bmatrix} \tag{A.17}$$

In the global diagonal matrix M, an interior node connected to 4 line elements represents a total length of $4 \times \frac{l}{2} = 2l$. This geometric "weight" is subsequently scaled by the physical parameters $\frac{\beta C_m}{\Delta t}$ during the assembly of the system matrix.
This matrix is sparse but not diagonal, as it accounts for the coupling between adjacent nodes.

$$M_{cons} = \frac{l}{6} \begin{bmatrix} 4 & 1 & 0 & 1 & 0 & 0 & 0 & 0 & 0 \\ 1 & 6 & 1 & 0 & 1 & 0 & 0 & 0 & 0 \\ 0 & 1 & 4 & 0 & 0 & 1 & 0 & 0 & 0 \\ 1 & 0 & 0 & 6 & 1 & 0 & 1 & 0 & 0 \\ 0 & 1 & 0 & 1 & 8 & 1 & 0 & 1 & 0 \\ 0 & 0 & 1 & 0 & 1 & 6 & 0 & 0 & 1 \\ 0 & 0 & 0 & 1 & 0 & 0 & 4 & 1 & 0 \\ 0 & 0 & 0 & 0 & 1 & 0 & 1 & 6 & 1 \\ 0 & 0 & 0 & 0 & 0 & 1 & 0 & 1 & 4 \end{bmatrix} \tag{A.18}$$

In the lumped version used by openCARP, the off-diagonal "1"s from the consistent matrix are summed into the diagonal. This makes the matrix strictly diagonal, representing the total tributary length assigned to each node.

$$M_{lump} = \frac{l}{2}\begin{bmatrix} 2 & 0 & 0 & 0 & 0 & 0 & 0 & 0 & 0 \\ 0 & 3 & 0 & 0 & 0 & 0 & 0 & 0 & 0 \\ 0 & 0 & 2 & 0 & 0 & 0 & 0 & 0 & 0 \\ 0 & 0 & 0 & 3 & 0 & 0 & 0 & 0 & 0 \\ 0 & 0 & 0 & 0 & 4 & 0 & 0 & 0 & 0 \\ 0 & 0 & 0 & 0 & 0 & 3 & 0 & 0 & 0 \\ 0 & 0 & 0 & 0 & 0 & 0 & 2 & 0 & 0 \\ 0 & 0 & 0 & 0 & 0 & 0 & 0 & 3 & 0 \\ 0 & 0 & 0 & 0 & 0 & 0 & 0 & 0 & 2 \end{bmatrix} \tag{A.19}$$

A.1.3 System Matrix

When solving the monodomain equation

$$\nabla \cdot (\sigma_m \nabla V_m) = \beta I_{ion} + \beta C_m \frac{dV_m}{dt} \tag{A.20}$$

with FEM we get the discretised equation:

$$KV_m = \frac{\beta C_m}{\Delta t} M_{lump} \Delta V_m + \beta M_{lump} I_{ion}. \tag{A.21}$$

By rearranging and multiplying both sides by the inverse of the lumped mass matrix M_{lump}^{-1} we get:

$$C_m \frac{\Delta V_m}{\Delta t} = \frac{1}{\beta} M_{lump}^{-1} K V_m - I_{ion}, \tag{A.22}$$

where

$$A = M_{lump}^{-1} K = \\ = \frac{2}{l} G \begin{bmatrix} 1 & -1/2 & 0 & -1/2 & 0 & 0 & 0 & 0 & 0 \\ -1/3 & 1 & -1/3 & 0 & -1/3 & 0 & 0 & 0 & 0 \\ 0 & -1/2 & 1 & 0 & 0 & -1/2 & 0 & 0 & 0 \\ -1/3 & 0 & 0 & 1 & -1/3 & 0 & -1/3 & 0 & 0 \\ 0 & -1/4 & 0 & -1/4 & 1 & -1/4 & 0 & -1/4 & 0 \\ 0 & 0 & -1/3 & 0 & -1/3 & 1 & 0 & 0 & -1/3 \\ 0 & 0 & 0 & -1/2 & 0 & 0 & 1 & -1/2 & 0 \\ 0 & 0 & 0 & 0 & -1/3 & 0 & -1/3 & 1 & -1/3 \\ 0 & 0 & 0 & 0 & 0 & -1/2 & 0 & -1/2 & 1 \end{bmatrix} \tag{A.23}$$

A.2 Simplified Kirchhoff Network Model Solution

If we assume that the conductances connecting the nodes are equal everywhere, and that all the cells share the same cross-sectional area A_m, then the SKNM equation becomes:

$$C_m \frac{dV_{\mathsf{m}}^k}{dt} = \frac{1}{A_m} \sum_{j \in N^k} G(V_{\mathsf{m}}^j - V_{\mathsf{m}}^k) - I_{\mathsf{ion}}^k(s^k, V_{\mathsf{m}}^k), \tag{A.24}$$

which can be rewritten in vector form as:

$$C_m \frac{dV_{\mathsf{m}}}{dt} = \frac{1}{A_m} G_{SKNM} V_{\mathsf{m}} - I_{\mathsf{ion}}, \tag{A.25}$$

where the matrix G_{SKNM} is the graph Laplacian of the grid scaled by the conductance. For the 3×3 grid, this matrix is defined by:

$$G_{SKNM} = G \begin{bmatrix} -2 & 1 & 0 & 1 & 0 & 0 & 0 & 0 & 0 \\ 1 & -3 & 1 & 0 & 1 & 0 & 0 & 0 & 0 \\ 0 & 1 & -2 & 0 & 0 & 1 & 0 & 0 & 0 \\ 1 & 0 & 0 & -3 & 1 & 0 & 1 & 0 & 0 \\ 0 & 1 & 0 & 1 & -4 & 1 & 0 & 1 & 0 \\ 0 & 0 & 1 & 0 & 1 & -3 & 0 & 0 & 1 \\ 0 & 0 & 0 & 1 & 0 & 0 & -2 & 1 & 0 \\ 0 & 0 & 0 & 0 & 1 & 0 & 1 & -3 & 1 \\ 0 & 0 & 0 & 0 & 0 & 1 & 0 & 1 & -2 \end{bmatrix}. \tag{A.26}$$

A.3 Comparison and (Non) Equivalence

Comparing the FEM formulation derived from openCARP and the SKNM formulation, we can identify a structural equivalence in the differential equations. Both systems describe the rate of change of the membrane potential as a function of the neighbouring potentials and the ionic current. However, a significant discrepancy arises in the coefficients of the diffusion term. In the FEM case, the matrix A is normalised by the diagonal of the lumped mass matrix. The non-equivalence is clearly visible at the boundaries. In openCARP's line-element FEM implementation, the lumped mass matrix accounts for the reduced "volume" of boundary and corner nodes. This leads to the diffusion term at a corner node having the same magnitude as that of an interior node. Conversely, in the SKNM formulation, unless the cross-sectional area A_m is adjusted locally to reflect the boundary conditions, the total current leaving a boundary node is strictly lower because it has fewer neighbours. This implies that openCARP's implementation acts as a normalised network where the conductivity is effectively scaled by the local connectivity to ensure consistency with the underlying continuous PDE (the cable equation) across the entire domain.

Appendix B

Fibroblast Results

B.1 Baseline

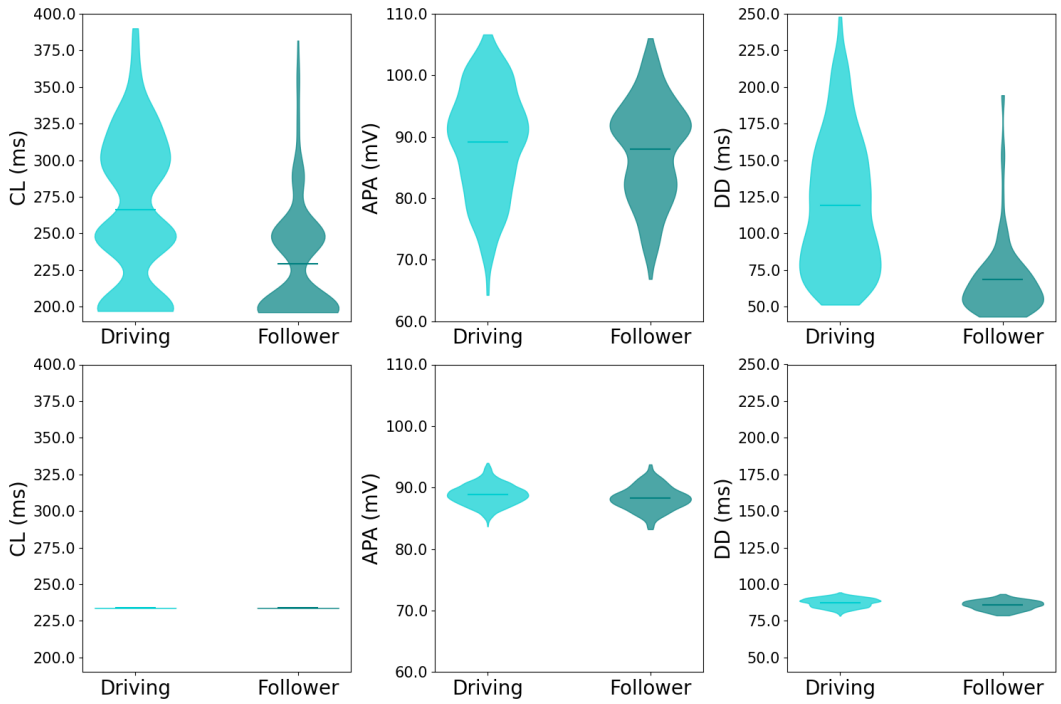

Figure B.1: Violin plots of the distribution of CL, APA and DD for the uncoupled (top) and the coupled (bottom) case. When coupling was present the spread in the distribution of these metrics decreased as a result of the entrainment in the tissue.

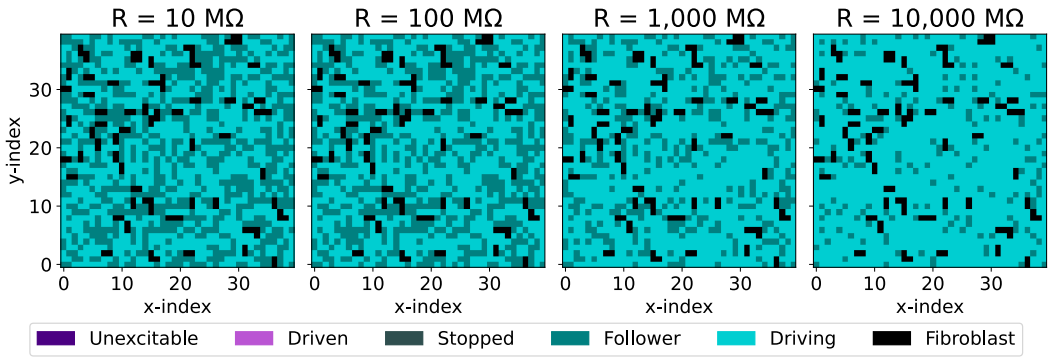

Figure B.2: Spatial distribution of the different cell categories for the different R_g values. Under baseline conditions all the cells are either *driving* or *follower*, but as R_g increases, so does the number of driving cells. The randomly distributed fibroblast form connected regions of at least two nodes because region tagging was used instead of the adjustment files.

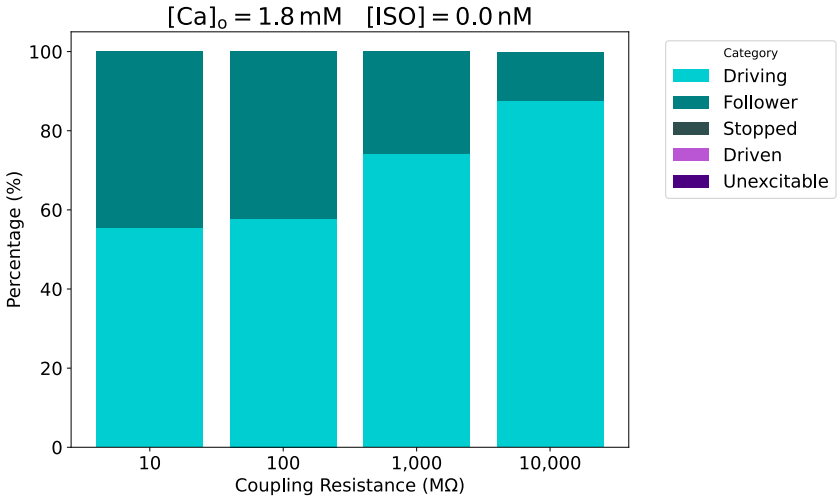

Figure B.3: Proportion of cells belonging to each category from the simulation pack under baseline condition and with fibroblasts.

B.2 Hypocalcaemia

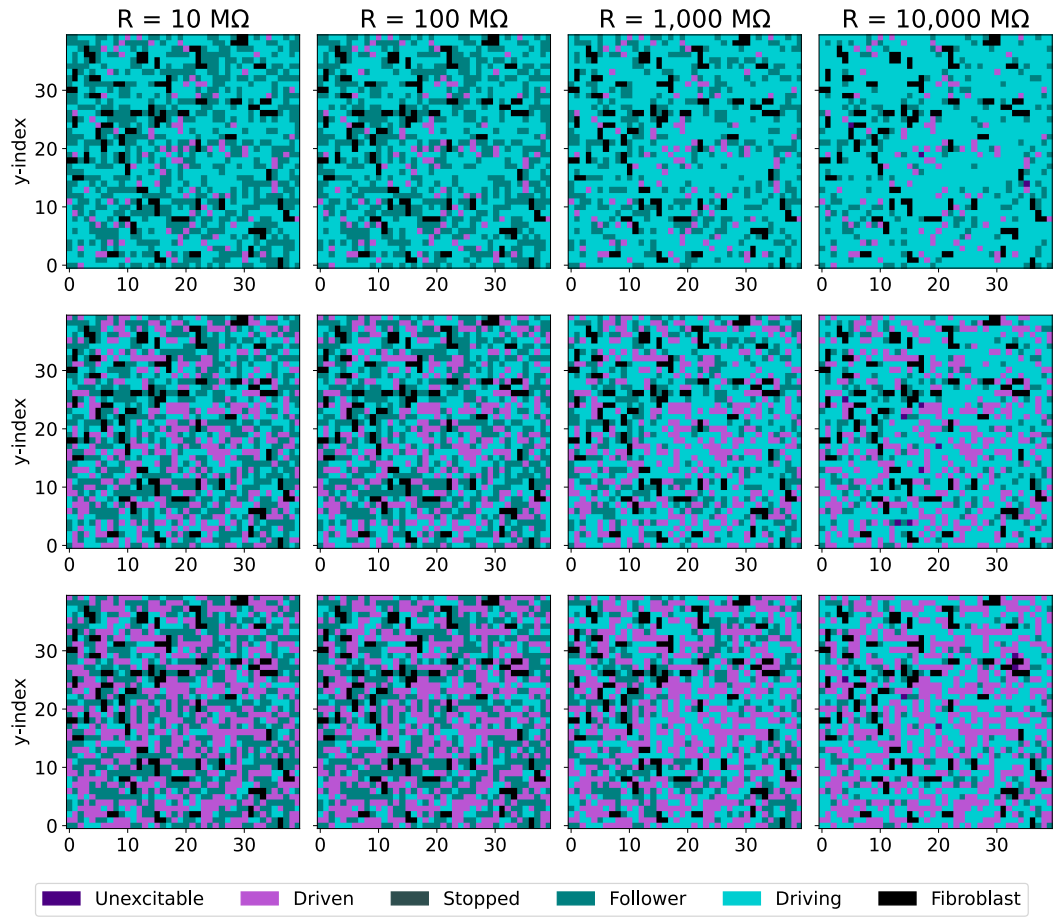

Figure B.4: Spatial distribution of the different cell categories from the simulation packs with hypocalcaemia and fibroblasts. It is evident that the quantity of unexcitable cells increased as extracellular calcium decreased from top ($[Ca^{2+}]_o = 1.2$ mM) to bottom $[Ca^{2+}]_o = 0.6$ mM. Nevertheless, almost all of them are driven. Only for $R_g = 10,000\,\text{MΩ}$ some cells became unexcitable.

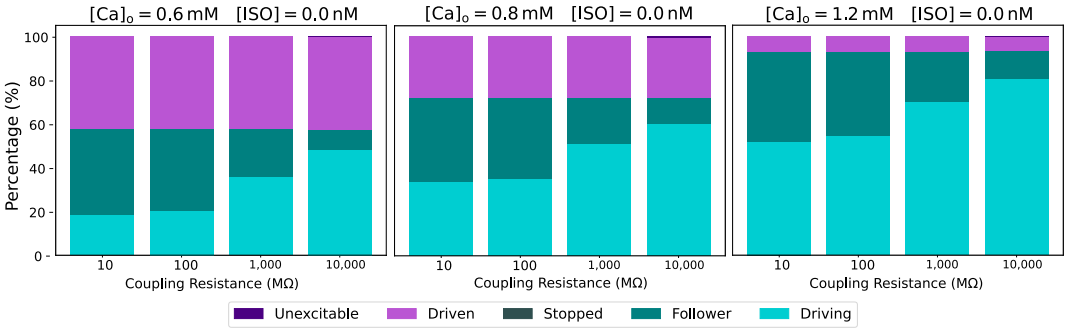

Figure B.5: Proportion of cells belonging to each category from the simulation packs under hypocalcaemia and with fibroblasts.

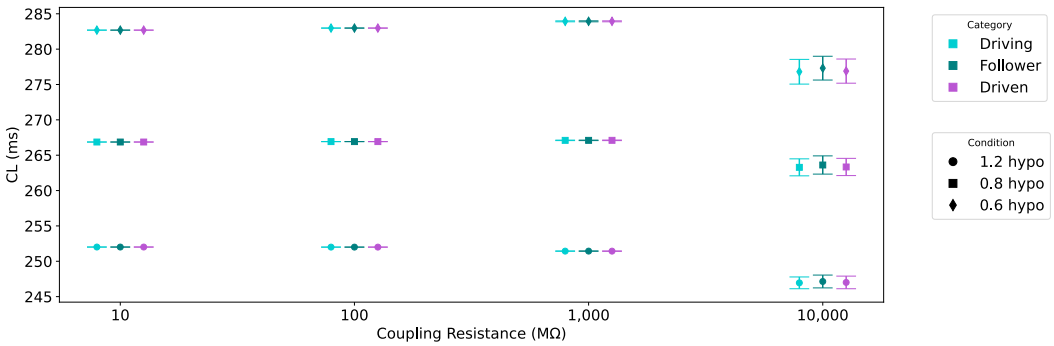

Figure B.6: CL of the different cell categories when coupling and fibroblasts were present. The CL increased as $[Ca^{2+}]_o$ decreased, and stayed mostly constant for all values of R_g at any given $[Ca^{2+}]_o$.

B.3 Autonomic Nervous System Compensation

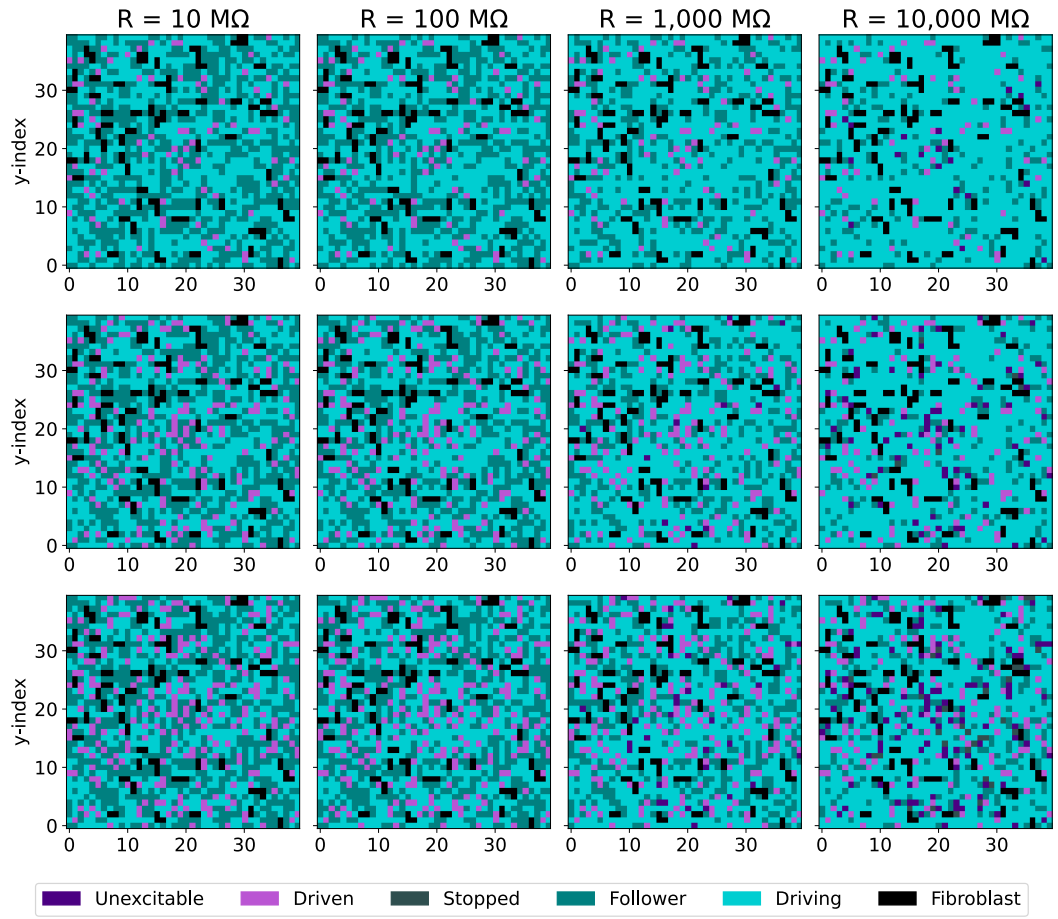

Figure B.7: Spatial distribution of the different cell categories from the simulation packs with hypocalcaemia and fibroblasts. For $R_g = 10,000\,\mathrm{M\Omega}$ cells were stopped by the large amount of fibroblasts.

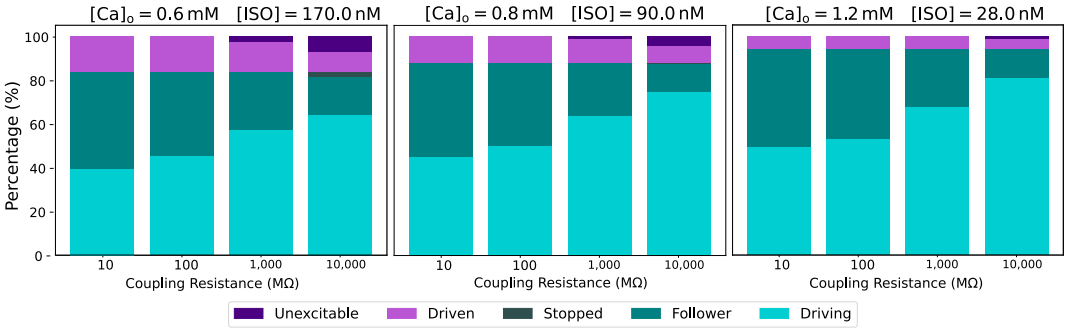

Figure B.8: Proportion of cells belonging to each category from the simulation pack under hypocalcaemia and simpathetic stimulation, with fibroblasts present.

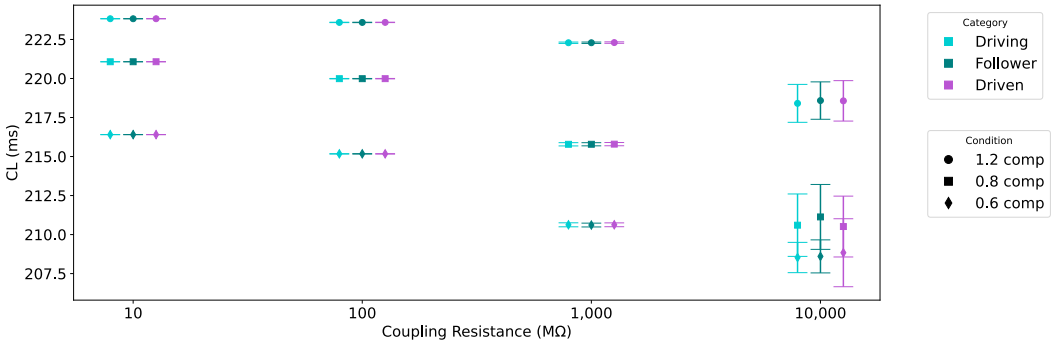

Figure B.9: CL of the different cell categories when coupling, fibroblast and sympathetic stimulation were present.

References

[1] A. Loewe, Y. Lutz, D. Nairn, et al., "Hypocalcemia-Induced Slowing of Human Sinus Node Pacemaking," *Biophysical Journal*, vol. 117, pp. 2244–2254, 2019. doi:10.1016/j.bpj.2019.07.037

[2] P. E. Stevens, S. B. Ahmed, J. J. Carrero, et al., "KDIGO 2024 Clinical Practice Guideline for the Evaluation and Management of Chronic Kidney Disease," *Kidney International*, vol. 105, pp. S117–S314, 2024. doi:10.1016/j.kint.2023.10.018

[3] F. Sacher, L. Jesel, C. Borni-Duval, et al., "Cardiac Rhythm Disturbances in Hemodialysis Patients," *JACC: Clinical Electrophysiology*, vol. 4, pp. 397–408, 2018. doi:10.1016/j.jacep.2017.08.002

[4] M. C. Wong, J. M. Kalman, E. Pedagogos, et al., "Temporal distribution of arrhythmic events in chronic kidney disease: Highest incidence in the long interdialytic period," *Heart Rhythm*, vol. 12, pp. 2047–2055, 2015. doi:10.1016/j.hrthm.2015.06.033

[5] L. Di Lullo, R. Rivera, V. Barbera, et al., "Sudden cardiac death and chronic kidney disease: From pathophysiology to treatment strategies," *International Journal of Cardiology*, vol. 217, pp. 16–27, 2016, publisher: Elsevier BV. doi:10.1016/j.ijcard.2016.04.170

[6] Y. Zhao, N. X. Chen, J. T. Shirazi, et al., "Subcutaneous nerve activity and mechanisms of sudden death in a rat model of chronic kidney disease," *Heart Rhythm*, vol. 13, pp. 1105–1112, 2016, publisher: Elsevier BV. doi:10.1016/j.hrthm.2015.12.040

[7] M. Santini, L. Schneider, M. Bištirlić, et al., "Case report: a unique case of sinus arrest and consequent symptomatic bradycardia caused by severe iatrogenic hypocalcemia," *Cardiologia Croatica*, vol. 19, pp. 408–408, 2024, publisher: Medicinska Naklada d.o.o. doi:10.15836/ccar2024.408

[8] M. Linder, T. Stary, G. Bitay, N. Nagy, and A. Loewe, "Sympathetic stimulation can compensate for hypocalcaemia-induced bradycardia in human and rabbit sinoatrial node cells," *The Journal of Physiology*, 2025, publisher: Wiley. doi:10.1113/jp287557

[9] C. Campana, E. Ricci, C. Bartolucci, S. Severi, and E. A. Sobie, "Coupling and heterogeneity modulate pacemaking capability in healthy and diseased two-dimensional sinoatrial node tissue models," *PLOS Computational Biology*, vol. 18, p. e1010098, 2022. doi:10.1371/journal.pcbi.1010098

[10] J. Zhao, R. Sharma, A. Kalyanasundaram, et al., "Mechanistic insight into the functional role of human sinoatrial node conduction pathways and pacemaker compartments heterogeneity: A computer model analysis," *PLOS Computational Biology*, vol. 19, p. e1011708, 2023, publisher: Public Library of Science (PLoS). doi:10.1371/journal.pcbi.1011708

[11] A. Amsaleg, J. Sánchez, R. Mikut, and A. Loewe, "Characterization of the pace-and-drive capacity of the human sinoatrial node: A 3D in silico study," *Biophysical Journal*, vol. 121, pp. 4247–4259, 2022, publisher: Elsevier BV. doi:10.1016/j.bpj.2022.10.020

[12] E. Ricci, F. Mazhar, M. Marzolla, S. Severi, and C. Bartolucci, "Sinoatrial node heterogeneity and fibroblasts increase atrial driving capability in a two-dimensional human computational model," *Frontiers in Physiology*, vol. 15, 2024, publisher: Frontiers Media SA. doi:10.3389/fphys.2024.1408626

[13] W. Roberts, S. Salandy, G. Mandal, et al., "Across the centuries: Piecing together the anatomy of the heart," *Translational Research in Anatomy*, vol. 17, p. 100051, 2019. doi:10.1016/j.tria.2019.100051

[14] P. A. Iaizzo, Ed., *Handbook of Cardiac Anatomy, Physiology, and Devices*. Cham: Springer Nature Switzerland, 2024. doi:10.1007/978-3-031-72581-4

[15] Molecular view of the cell membrane. https://www.britannica.com/science/cell-membrane#/media/1/463558/45550

[16] T. Hong and R. M. Shaw, "Cardiac T-Tubule Microanatomy and Function," *Physiological Reviews*, vol. 97, pp. 227–252, 2017. doi:10.1152/physrev.00037.2015

[17] M. Ruiz, "File:gap cell junction-en.svg," Wikimedia Commons, 2006, accessed: 2026-01-14. https://commons.wikimedia.org/wiki/File:Gap-cell-junction-en.svg

[18] A. Keith and M. Flack, "The Form and Nature of the Muscular Connections between the Primary Divisions of the Vertebrate Heart," *Journal of Anatomy and Physiology*, vol. 41, pp. 172–189, 1907.

[19] J. N. Weiss and Z. Qu, "The Sinus Node," *JACC: Clinical Electrophysiology*, vol. 6, pp. 1841–1843, 2020. doi:10.1016/j.jacep.2020.09.017

[20] T. A. Csepe, J. Zhao, B. J. Hansen, et al., "Human sinoatrial node structure: 3D microanatomy of sinoatrial conduction pathways," *Progress in Biophysics and Molecular Biology*, vol. 120, pp. 164–178, 2016. doi:10.1016/j.pbiomolbio.2015.12.011

[21] V. V. Fedorov, A. V. Glukhov, R. Chang, et al., "Optical Mapping of the Isolated Coronary-Perfused Human Sinus Node," *Journal of the American College of Cardiology*, vol. 56, pp. 1386–1394, 2010. doi:10.1016/j.jacc.2010.03.098

[22] N. Chandler, O. Aslanidi, D. Buckley, et al., "Computer Three-Dimensional Anatomical Reconstruction of the Human Sinus Node and a Novel Paranodal Area," *The Anatomical Record*, vol. 294, pp. 970–979, 2011. doi:10.1002/ar.21379

[23] E. Ricci, C. Bartolucci, and S. Severi, "The virtual sinoatrial node: What did computational models tell us about cardiac pacemaking?" *Progress in Biophysics and Molecular Biology*, vol. 177, pp. 55–79, 2023. doi:10.1016/j.pbiomolbio.2022.10.008

[24] M. Boyett, "The sinoatrial node, a heterogeneous pacemaker structure," *Cardiovascular Research*, vol. 47, pp. 658–687, 2000. doi:10.1016/S0008-6363(00)00135-8

[25] G. López Garza, N. P. Castellanos, and R. Godínez, "Cell-to-cell modeling of the interface between atrial and sinoatrial anisotropic heterogeneous nets," *Computational Biology and Chemistry*, vol. 68, pp. 245–259, 2017. doi:10.1016/j.compbiolchem.2017.04.008

[26] D. DiFrancesco, "A Brief History of Pacemaking," *Frontiers in Physiology*, vol. 10, p. 1599, 2020. doi:10.3389/fphys.2019.01599

[27] D. Noble, "A modification of the Hodgkin—Huxley equations applicable to Purkinje fibre action and pacemaker potentials," *The Journal of Physiology*, vol. 160, pp. 317–352, 1962. doi:10.1113/jphysiol.1962.sp006849

[28] D. C. Michaels, E. P. Matyas, and J. Jalife, "Mechanisms of sinoatrial pacemaker synchronization: a new hypothesis." *Circulation Research*, vol. 61, pp. 704–714, 1987. doi:10.1161/01.RES.61.5.704

[29] O. Monfredi, K. Tsutsui, B. Ziman, M. D. Stern, E. G. Lakatta, and V. A. Maltsev, "Electrophysiological heterogeneity of pacemaker cells in the rabbit intercaval region, including the SA node: insights from recording multiple ion currents in each cell," *American Journal of Physiology-Heart and Circulatory Physiology*, vol. 314, pp. H403–H414, 2018. doi:10.1152/ajpheart.00253.2016

[30] S. R. Kharche, E. Vigmond, I. R. Efimov, and H. Dobrzynski, "Computational assessment of the functional role of sinoatrial node exit pathways in the human heart," *PLOS ONE*, vol. 12, p. e0183727, 2017. doi:10.1371/journal.pone.0183727

[31] A. A. Karpaev, R. A. Syunyaev, and R. R. Aliev, "Effects of fibroblast-myocyte coupling on the sinoatrial node activity: A computational study," *International Journal for Numerical Methods in Biomedical Engineering*, vol. 34, p. e2966, 2018. doi:10.1002/cnm.2966

[32] R. E. Klabunde, *Cardiovascular physiology concepts*, third edition ed. Philadelphia Baltimore New York London: Wolters Kluwer, 2022.

[33] J. Behar, A. Ganesan, J. Zhang, and Y. Yaniv, "The Autonomic Nervous System Regulates the Heart Rate through cAMP-PKA Dependent and Independent Coupled-Clock Pacemaker Cell Mechanisms," *Frontiers in Physiology*, vol. 7, 2016, publisher: Frontiers Media SA. doi:10.3389/fphys.2016.00419

[34] F. A. Garza and S. W. Leslie, "Anatomy, Abdomen and Pelvis: Kidneys," in *statpearls*. Treasure Island (FL): StatPearls Publishing, 2025. http://www.ncbi.nlm.nih.gov/books/NBK482385/

[35] P. A. Gallardo and C. P. Vio, *Renal Physiology and Hydrosaline Metabolism*. Cham: Springer International Publishing, 2022. doi:10.1007/978-3-031-10256-1

[36] S. D. Serai and K. Darge, Eds., *Advanced Clinical MRI of the Kidney: Methods and Protocols*. Cham: Springer International Publishing, 2023. doi:10.1007/978-3-031-40169-5

[37] A. L. Ammirati, "Chronic Kidney Disease," *Revista da Associação Médica Brasileira*, vol. 66, pp. s03–s09, 2020. doi:10.1590/1806-9282.66.s1.3

[38] National Collaborating Centre for Infectious Diseases. (2015) Understanding summary measures used to estimate the burden of disease: All about halys, dalys and qalys. National Collaborating Centre for Infectious Diseases. Online document explaining summary measures of disease burden such as HALYs, DALYs, and QALYs. https://nccid.ca/publications/understanding-summary-measures-used-to-estimate-the-burden-of-disease/

[39] G. Phadke and R. Khanna, "Renal replacement therapies," *Missouri Medicine*, vol. 108, pp. 45–49, 2011.

[40] S. Severi, M. Fantini, L. A. Charawi, and D. DiFrancesco, "An updated computational model of rabbit sinoatrial action potential to investigate the mechanisms of heart rate modulation," *The Journal of Physiology*, vol. 590, pp. 4483–4499, 2012, publisher: Wiley. doi:10.1113/jphysiol.2012.229435

[41] K. H. Jæger and A. Tveito, "The simplified Kirchhoff network model (SKNM): a cell-based reaction–diffusion model of excitable tissue," *Scientific Reports*, vol. 13, p. 16434, 2023. doi:10.1038/s41598-023-43444-9

[42] A. L. Hodgkin and A. F. Huxley, "A quantitative description of membrane current and its application to conduction and excitation in nerve," *The Journal of Physiology*, vol. 117, pp. 500–544, 1952. doi:10.1113/jphysiol.1952.sp004764

[43] Y. Rudy, "9.14 From Genes and Molecules to Organs and Organisms: Heart," in *comprehensive biophysics*. Elsevier, 2012, pp. 268–327. doi:10.1016/B978-0-12-374920-8.00924-3

[44] D. Noble, “From the Hodgkin–Huxley axon to the virtual heart,” *The Journal of Physiology*, vol. 580, pp. 15–22, 2007. doi:10.1113/jphysiol.2006.119370

[45] K. H. Jæger, J. D. Trotter, X. Cai, H. Arevalo, and A. Tveito, “Evaluating computational efforts and physiological resolution of mathematical models of cardiac tissue,” *Scientific Reports*, vol. 14, p. 16954, 2024. doi:10.1038/s41598-024-67431-w

[46] A. Tveito, K.-A. Mardal, and M. E. Rognes, Eds., *Modeling Excitable Tissue: The EMI Framework*, Simula SpringerBriefs on Computing, vol. 7. Cham: Springer International Publishing, 2021. doi:10.1007/978-3-030-61157-6

[47] K. H. Jæger and A. Tveito, “Efficient, cell-based simulations of cardiac electrophysiology; The Kirchhoff Network Model (KNM),” *npj Systems Biology and Applications*, vol. 9, p. 25, 2023. doi:10.1038/s41540-023-00288-3

[48] F. B. Sachse, *Computational cardiology: modeling of anatomy, electrophysiology, and mechanics*, Lecture Notes in Computer Science, no. 2966. Berlin, Heidelberg, [Germany]: Springer, 2004.

[49] G. Plank, A. Loewe, A. Neic, et al., “The openCARP simulation environment for cardiac electrophysiology,” *Computer Methods and Programs in Biomedicine*, vol. 208, p. 106223, 2021. doi:10.1016/j.cmpb.2021.106223

[50] R. R. Aliev and A. V. Panfilov, “A simple two-variable model of cardiac excitation,” *Chaos, Solitons & Fractals*, vol. 7, pp. 293–301, 1996. doi:10.1016/0960-0779(95)00089-5

[51] B. A. J. Lawson, C. C. Drovandi, N. Cusimano, P. Burrage, B. Rodriguez, and K. Burrage, “Unlocking data sets by calibrating populations of models to data density: A study in atrial electrophysiology,” *Science Advances*, vol. 4, p. e1701676, 2018. doi:10.1126/sciadv.1701676

[52] V. A. Maltsev, J. W. Kyle, S. Mishra, and A. Undrovinas, “Molecular identity of the late sodium current in adult dog cardiomyocytes identified by Na_v 1.5 antisense inhibition,” *American Journal of Physiology-Heart and Circulatory Physiology*, vol. 295, pp. H667–H676, 2008. doi:10.1152/ajpheart.00111.2008

[53] R. Morgan, M. A. Colman, H. Chubb, G. Seemann, and O. V. Aslanidi, “Slow Conduction in the Border Zones of Patchy Fibrosis Stabilizes the Drivers for Atrial Fibrillation: Insights from Multi-Scale Human Atrial Modeling,” *Frontiers in Physiology*, vol. 7, 2016. doi:10.3389/fphys.2016.00474

[54] P. Boyle. (2026) Cellular dynamics heterogeneity (opencarp example). https://opencarp.org/documentation/examples/02_ep_tissue/05c_cellular_dynamics_heterogeneity. openCARP community. Example documentation for openCARP demonstrating heterogeneous cell-scale dynamics in tissue simulations.

[55] A. Fabbri, M. Fantini, R. Wilders, and S. Severi, “Computational analysis of the human sinus node action potential: model development and effects of mutations,” 2017.

[56] A. Loewe, Y. Lutz, N. Nagy, et al., “Inter-Species Differences in the Response of Sinus Node Cellular Pacemaking to Changes of Extracellular Calcium.”

[57] T. M. Vinogradova, K. Y. Bogdanov, and E. G. Lakatta, “-Adrenergic Stimulation Modulates Ryanodine Receptor Ca^{2+} Release During Diastolic Depolarization to Accelerate Pacemaker Activity in Rabbit Sinoatrial Nodal Cells,” *Circulation Research*, vol. 90, pp. 73–79, 2002. doi:10.1161/hh0102.102271

[58] A. Bucchi, M. Baruscotti, R. B. Robinson, and D. DiFrancesco, “Modulation of rate by autonomic agonists in SAN cells involves changes in diastolic depolarization and the pacemaker current,” *Journal of Molecular and Cellular Cardiology*, vol. 43, pp. 39–48, 2007. doi:10.1016/j.yjmcc.2007.04.017

[59] P. Camelliti, C. R. Green, I. LeGrice, and P. Kohl, "Fibroblast Network in Rabbit Sinoatrial Node: Structural and Functional Identification of Homogeneous and Heterogeneous Cell Coupling," *Circulation Research*, vol. 94, pp. 828–835, 2004. doi:10.1161/01.RES.0000122382.19400.14